

***In Situ*, Through-Thickness Potential Distribution Measurements in  
Electrochemical Energy Conversion and Storage Devices**

Submitted in partial fulfillment of the requirements for

the degree of

Doctor of Philosophy

in

Mechanical Engineering

Katherine C. Tully

B.S., Mechanical Engineering, Carnegie Mellon University  
M.S., Mechanical Engineering, Carnegie Mellon University

Carnegie Mellon University  
Pittsburgh, PA

April 26<sup>th</sup>, 2013

UMI Number: 3573493

All rights reserved

INFORMATION TO ALL USERS

The quality of this reproduction is dependent upon the quality of the copy submitted.

In the unlikely event that the author did not send a complete manuscript and there are missing pages, these will be noted. Also, if material had to be removed, a note will indicate the deletion.



UMI 3573493

Published by ProQuest LLC 2013. Copyright in the Dissertation held by the Author.

Microform Edition © ProQuest LLC.

All rights reserved. This work is protected against unauthorized copying under Title 17, United States Code.



ProQuest LLC  
789 East Eisenhower Parkway  
P.O. Box 1346  
Ann Arbor, MI 48106-1346

© Copyright by Katherine Cane Tully 2013  
All Rights Reserved

# CARNEGIE MELLON UNIVERSITY

CARNEGIE INSTITUTE OF TECHNOLOGY

## THESIS

SUBMITTED IN PARTIAL FULFILLMENT OF THE REQUIREMENTS

FOR THE DEGREE OF Doctor of Philosophy


TITLE *In Situ, Through-Thickness Potential Distribution Measurements in*  
*Electrochemical Energy Conversion and Storage Devices*

PRESENTED BY Katherine Cane Tully

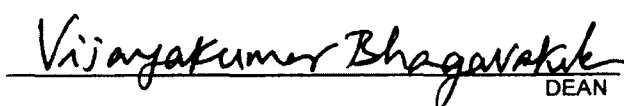
ACCEPTED BY THE DEPARTMENT OF  
Mechanical Engineering

  
\_\_\_\_\_  
ADVISOR, MAJOR PROFESSOR

5/17/2013  
\_\_\_\_\_  
DATE

  
\_\_\_\_\_  
DEPARTMENT HEAD

5/21/13  
\_\_\_\_\_  
DATE

APPROVED BY THE COLLEGE COUNCIL  
  
\_\_\_\_\_  
DEAN

May 22, 2013  
\_\_\_\_\_  
DATE

# Abstract

Fuel cells, batteries and capacitors are becoming increasingly important in modern technology as we begin to move away from fossil fuels in an effort to decrease pollution and our reliance on non-renewable energy sources. However, there are still many technical barriers that must be overcome before these technologies become economically and commercially viable. One important hurdle to overcome is poor transport through the thickness of porous electrodes. This leads to under utilization of the electrode materials making the electrodes costly and hindering efforts to reach performance goals. Unfortunately, studying through-plane transport in these electrodes under standard operating conditions is challenging as the electrodes are difficult to access and the electrode structure must not be compromised.

We have developed an electrode scaffold (ES) device for making *in situ*, through-thickness distribution measurements in porous electrodes. The device allows for sensing layers to contact the perimeter of a 1-D column of working electrode at known, discrete points through the electrode thickness without interrupting the electrode structure or otherwise interfering with standard operation. The sensing layers are made accessible to a data acquisition board that is used to measure and record potential measurements from each layer. To the best of our knowledge, these measurements are the first distribution measurements gathered from fuel cell and capacitor electrodes that have been obtained *in situ* under standard operating conditions without altering the electrode's structure.

Variations of the ES have been implemented on the porous electrodes of polymer electrolyte membrane (PEM) fuel cells and electrochemical double layer (EDL) capacitors to investigate the distributions that evolve during standard operation. Additionally, we have developed a mathematical technique that allows us to further characterize the electrode by finding local current and charging current distributions from the potential distribution data using finite difference methods. The results show that the distributions through the electrode are often non-uniform, likely due to poor through-plane transport, which leads to under utilized areas of the electrode and therefore, cost inefficiencies. The ES was able to detect anomalies such as a higher than expected ionic conductivity, stray currents and under performing electrode geometries. These measurements allow us to gain a more thorough understanding of the processes taking place in the electrodes during operation and provide us with information that we believe will help to improve electrode performance in the future.

# Acknowledgments

I would like to thank my advisor for giving me the opportunity to work with him and guiding me through the Ph. D. process. I learned an incredible amount from him in my time in the TPES lab and truly admire his extensive knowledge and his dedication to his work. I have grown immeasurably as a writer and researcher under his guidance.

I want to thank all of the TPES lab members for making our lab an enjoyable and interesting place to work. It has been great getting to know all of you and work closely with some of you. I especially want to thank Billy Epting and Iryna Zenyuk for their support and camaraderie, and for working through everything from problem sets to presentations with me along the way. I am very grateful to have had such fun, intelligent and helpful labmates that I could rely on and learn from. I also want to thank all of my Wellesley and CMU friends as well as my PSL teammates for adding balance to my life and keeping things fun, interesting and active.

I would like to thank all of the mechanical engineering machine shop staff as well as the mechanical engineering staff and faculty. I appreciate the work they put into helping us keep our labs properly functioning, creating the tools we need for our research, organizing events and courses, and providing a bit of a distraction now and then so we don't forget to have fun with our work.

I would like to acknowledge the additional members of my dissertation committee, Professor Jay Whitacre, Professor Yoed Rabin and Professor Jeremy Michalek. I appreciate their thoughtful comments and insights that improved and shaped my research.

I gratefully acknowledge funding for this research from both the Pennsylvania Infrastructure Technology Alliance (PITA) and the Dowd Fellowship. The funding from these grants had an enormous effect on the amount and quality of the work I was able to accomplish during my time at Carnegie Mellon.

Finally, I want to say a huge thank you to my family for all of their love and support and for helping me to be where I am today. To my parents, Walter Hess and Janice Cane, thank you for the drive and determination you've instilled in me and for always supporting and believing in me. To my wonderful husband, Stephen Tully, thank you for your patient and loving support through this often stressful and overwhelming process. I couldn't have done it without you.



# Table of Contents

<b>Abstract .....</b>	<b>iv</b>
<b>Acknowledgments .....</b>	<b>vi</b>
<b>List of Tables .....</b>	<b>xi</b>
<b>List of Figures .....</b>	<b>xii</b>
<b>1. Introduction .....</b>	<b>1</b>
1.1 Motivation .....	1
1.2 Polymer Electrolyte Membrane Fuel Cells .....	3
1.2.1 Standard Operation .....	4
1.2.2 Common PEM Fuel Cell Performance Characterization Methods .....	7
1.3 Hybrid Batteries and EDL Capacitors .....	14
1.3.1 Standard Operation .....	14
1.3.2 Common Performance Characterization Methods .....	17
1.4 Related Work .....	23
1.5 Method .....	27
1.6 Scope of Thesis .....	31
<b>2. The MES as Applied to PEM Fuel Cell Electrodes .....</b>	<b>32</b>
2.1 Experimental Setup .....	33
2.1.1 MES Build .....	33
2.1.2 Catalyst Ink Preparation .....	36
2.1.3 MES Hardware .....	36
2.1.4 Preparation of 1 cm <sup>2</sup> MEA .....	38
2.1.5 Equipment and Testing Procedures .....	38
2.2 MES Baseline Testing .....	40
2.2.1 Reliability Testing .....	40
2.2.2 Assessment of Effects of MES Assembly on Performance .....	44
2.3 MES Results .....	48
2.3.1 Transient Changes in Potential Distribution .....	48
2.3.2 Polarization Curve Analysis .....	52
2.4 Summary .....	57
<b>3. A Mathematical Method for Determining Local Current, Charging Current and Charge Stored from Potential Distributions .....</b>	<b>59</b>
3.1 Finite Difference Methods Derivations .....	60
3.2 Charge Storage .....	66
3.3 Error Calculations .....	67
3.3.1 Error Propagation Equations as Applied to ES Data .....	67
3.3.2 Error Analysis of Analytical Equation .....	70
3.4 Error Sensitivity Analysis .....	73
3.5 Optimal Spacing Analysis .....	79

3.6 Summary.....	86
<b>4. An ES for Gathering Electric Potential Distributions Across a Symmetric EDL Capacitor Electrode.....</b>	<b>87</b>
4.1 Experimental Setup .....	88
4.1.1 Electric ES Build and Cell Assembly.....	89
4.1.2 Equipment and Testing Procedures .....	91
4.2 Preliminary Testing Results.....	92
4.2.1 Conductivity Measurements.....	93
4.2.2 Conventional Cell-Terminal Characterization .....	95
4.3 Electric ES Results .....	99
4.3.1 Potentiostatic Charging .....	99
4.3.2 Galvanostatic Discharging.....	108
4.4 Summary.....	114
<b>5. An ES for Gathering Ionic Potential Distributions Across a Symmetric EDL Capacitor Electrode.....</b>	<b>117</b>
5.1 Experimental Setup .....	118
5.1.1 Ionic ES Build and Cell Assembly.....	118
5.1.2 Equipment and Testing Procedures .....	121
5.2 Preliminary Results .....	122
5.3 Ionic ES Results .....	125
5.3.1 Galvanostatic Charging .....	125
5.3.2 Effects of Charging Parameters on Charge Storage Distribution.....	135
5.3.3 Effectiveness Factor .....	138
5.4 Summary.....	141
<b>6. Conclusions, Contributions and Recommendations for Future Work.....</b>	<b>143</b>
6.1 Conclusions and Contributions.....	143
6.1.1 MES Applied to the Cathode Catalyst Layer of a PEM Fuel Cell .....	144
6.1.2 Mathematical Methods Used to Assess Electric and Ionic Potential Distribution Methods in Aqueous Sodium EDL Capacitors .....	145
6.1.3 ES Used to Make Electrical Potential Distribution Measurements in an Aqueous Sodium EDL Capacitor .....	146
6.1.4 ES Used to Make Ionic Potential Distribution Measurements in an Aqueous Sodium EDL Capacitor .....	148
6.2 Recommendations for Future Work .....	149
6.2.1 MES Applied to PEM Fuel Cells .....	149
6.2.2 Electric ES Applied to EDL Capacitors .....	151
6.2.3 Ionic ES Applied to EDL Capacitors. ....	151
<b>A. Nafion Supported EDL Capacitor Electrodes .....</b>	<b>153</b>
<b>B. Macro-structuring EDL Capacitor Electrodes for Improved Through-Plane Transport.....</b>	<b>158</b>

**C. In Situ, Through-Thickness Distribution Measurements of Oxygen Partial Pressure in a PEM Fuel Cell.....166**

**References .....172**

# List of Tables

Table 2.1 Fitting parameters for potential distribution under dry conditions shown in Figure 6c, including the measured Ohmic overpotential, $\eta_{ohm}$ .....	55
Table A.1 The results of CV scans conducted at multiple different scan rates on electrodes with varying amounts of Nafion in the electrode material.....	156
Table B.1 Results from CV and EIS run on cells using electrodes with 89 wt % activated carbon, 10 wt % FEP and 1 wt % Triton X. A single 500 $\mu\text{m}$ diameter hole was drilled halfway through the thickness of both electrodes in these tests.....	163
Table B.2 Results from CV and EIS run on cells using electrodes with 89 wt % activated carbon, 10 wt % FEP and 1 wt % Triton X. These standard electrodes did not have holes drilled into them.....	164

# List of Figures

- Figure 1.1 Schematic of a PEM fuel cell using hydrogen and air to produce electricity with water and heat as byproducts.....4
- Figure 1.2 Schematic of a PEM fuel cell cathode. Protons from the anode cross the PEM and electrons travel through an external load. They react with oxygen at Pt catalyst particles, producing water according to the ORR. The oxygen is delivered from the gas channels through an adjacent porous carbon GDL.....5
- Figure 1.3 A typical polarization curve for a PEM fuel cell operating under standard conditions. The dashed curves show loss of voltage associated with the overpotentials. The activation polarization losses, ohmic losses and concentration polarization losses affect the shape of the polarization curve most notably in the accompanying regions. .8
- Figure 1.4 CV performed on a 1 cm<sup>2</sup> MEA. The cell and gas humidifiers were all held at 30 °C and a voltage sweep was conducted from 0 to 0.8 V at a rate of 40 mV/s..... 11
- Figure 1.5 Schematic of an aqueous sodium hybrid battery. The positive electrode is a sodium intercalation material similar to the positive electrode of a Li-ion battery. The negative electrode is made from an EDL capacitance material, such as activated carbon, typically found in EDL capacitors..... 15
- Figure 1.6 Cross-section of a symmetric EDL capacitor during charging. When a voltage is applied to the cell, electrons leave the carbon in the positive electrode and travel into the negative electrode carbon creating a positive surface charge and a negative surface charge, respectively. The electrolyte then breaks down with the sodium and sulfate ions being respectively drawn towards the negative and positive electrodes. It is believed that charging begins in the region next to separator and moves outwards towards the current collectors..... 17
- Figure 1.7 A typical CV curve for an EDL capacitor. This is the result of a CV conducted on an EDL capacitor with ultra-thick electrodes. The voltage was swept between -0.9 and 0.9 V at a scan rate of 0.1 mV/s. .... 19
- Figure 1.8 A typical EIS plot for an EDL capacitor. This data was obtained using a 10 mV perturbation over a frequency range of 1 MHz to 30 μHz. .... 21
- Figure 1.9 Example of a charge cycle for an EDL capacitor. This cell was charged at a constant current of 76 A/m<sup>2</sup> from 0 to 0.7 V..... 23
- Figure 1.10 Example of an analytical solution to the current conservation equation for a porous electrode. It can be seen that a potential distribution develops through the thickness of the electrode during operation..... 29

- Figure 1.11 A schematic of the proposed device, which will allow for distribution measurements to be collected in porous electrodes..... 31
- Figure 2.1 Electron micrographs of MES substrates. a. SEM image of a laser-cut hole in the MES, b. SEM image showing alternating Nafion (light) and Kapton (dark) layers inside of the hole, and c. TEM image of alternating Nafion and Kapton layers showing approximately uniform 1  $\mu\text{m}$  thick sensing layers..... 34
- Figure 2.2 Schematic of the membrane electrode assembly for a PEM fuel cell with the MES being implemented. .... 35
- Figure 2.3 A schematic of the MES hardware (left) for use with the MES to make ionic potential measurements through the thickness of a PEM fuel cell cathode. Close ups of the cathode and anode plates (right), as well as a fully constructed MES (top). ..... 37
- Figure 2.4 A schematic showing a comparison between the MES used for baseline testing (left) and the MES used for potential distribution data gathering (right). It can be seen that the MES on the left has all tabs protruding from a single sensing layer, while the MES on the right has each tab protruding from a different sensing layer. Note that the thickness in these schematics is exaggerated for clarity..... 41
- Figure 2.5 RE variability during a potentiostatic polarization curve with fuel cell voltages ranging between 0.8 and 0.2 V. The bars represent the mean potential standard deviation of the four REs for five realizations. The error bars are the standard deviation of the standard deviations. Deviations on the order of  $\sim 5$  mV or less ensure adequate resolution for gathering through-plane data. .... 43
- Figure 2.6 Comparison between the electrochemical characteristics of an MES and a 1  $\text{cm}^2$  MEA. The solid lines in the main plot are the polarization data collected at 57/57/35  $^\circ\text{C}$  (anode dew point/cell/cathode dew point); dashed lines show the IR-free curves. The inset shows cyclic voltammograms measured for the MES and the 1  $\text{cm}^2$  MEA with the vertical axis being the area-specific current density..... 45
- Figure 2.7 Effects of flooding and drying on the potential distribution through the electrode. a. Voltage and temperature time-series as the cathode dew point changed from 50 to 35  $^\circ\text{C}$  during a galvanostatic hold at 520  $\text{mA}/\text{cm}^2$ . b. Electrolyte potential distributions for both flooded (57/57/50  $^\circ\text{C}$ ) and dry (57/57/35  $^\circ\text{C}$ ) times indicated by the dashed lines in part a. Potential data for each case was averaged over 60 s. Error bars are a root mean square combination of the HRE standard deviation at OCV (2 mV) and the temporal variations of each HRE over the time-averaging period..... 49

Figure 2.8 Polarization curves and electrolyte potential distributions through the thickness of the electrode as measured by the MES. a, Polarization and IR-free curves for both flooded (57/57/50°C) and dry (57/57/35°C) conditions. b, Electrolyte potential distributions through the thickness of the MES in flooded conditions during potentiostatic holds; starting with OCV (squares) then 0.7 V to 0.2 V (circles). The solid lines are linear fits at each fuel cell potential. c, Electrolyte potential distributions through the thickness of the MES in dry conditions during potentiostatic holds; starting with OCV (squares) then 0.7 V to 0.2 V (circles). Solid lines show the analytical solution for a uniform reaction rate at each fuel cell potential. .... 53

Figure 3.1 Positions at which conductivity,  $\sigma$ , and potential,  $\phi$ , measurements were taken. .... 62

Figure 3.2 Error sensitivity plots for local current (top row) and charging current (bottom) at about 4 minutes of charging. In both cases the sensitivity is plotted for forward and backward difference cases as well as a representative central difference case. Red dots and percentage values denote the errors that are used in our final analysis. Sensitivity towards  $E_x$  is not shown as there is no noticeable effect within reasonable error bounds..... 76

Figure 3.3 Error sensitivity plots for local current (top row) and charging current (bottom) at about 15 minutes of charging. In both cases the sensitivity is plotted for forward and backward difference cases as well as a representative central difference case. Red dots and percentage values denote the errors that are used in our final analysis. Sensitivity towards  $E_x$  is not shown as there is no noticeable effect within reasonable error bounds..... 77

Figure 3.4 Total error associated with calculating the local current shown as a percentage of the total current used to charge the cell and as a function of the number of sensing layers used. .... 85

Figure 3.5 Total error associated with calculating the charging current shown as a percentage of the total volumetric charging current used to charge the cell and as a function of the number of sensing layers used. .... 85

Figure 4.1 a. Schematic of the ES cross-section showing the alternating sensing and insulating layers on the negative electrode. b. A photo of an assembled ES. .... 91

Figure 4.2 Conductivity through the thickness of the negative electrode using both pre-assembled and assembled configurations of the ES. .... 94

Figure 4.3 CV conducted at 40 A/m<sup>2</sup> (0.1 mV/s) from 0 V to 0.9 V, yielding a capacitance of 17.3 F/g. The inset shows data for a constant current discharge held at 22.5 A/m<sup>2</sup> for four hours that gives a comparable capacitance result of 38 F/g when taking the slower discharge rate into consideration. .... 96

Figure 4.4 CV comparison between the ES (solid red line) and an all acrylic capacitor with the same dimensions (dashed black line). Similar shapes and areas dictate that the ES does not affect the performance of the electrode. .... 97

Figure 4.5 Constant voltage charging at 0.9 V. a. Voltage-time series showing raw potential data from the ES. The top right inset is the corresponding current-time series. The bottom left inset shows the placement of each sensing layer on the ES structure. b. Voltage versus the current collector as a function of the distance away from the separator at eight logarithmically distributed times. The dashed lines are fits to the analytical solution for uniform charging and conductivity. Deviations between the solid experimental data lines and the dashed analytical solution lines indicate non-uniform charging. Symbols denote times plotted:  $\diamond$  - 63 s,  $\triangle$  - 100 s,  $\square$  - 159 s,  $\circ$  - 251 s,  $\times$  - 398 s,  $\nabla$  - 631 s,  $\star$  - 1000 s,  $+$  - 1585 s. .... 101

Figure 4.6 Constant voltage charging at 0.9 V. a. Local current plotted as a function of distance through the electrode. Lower currents near the separator suggest charge storage taking place here. b. Volumetric charging current through the thickness of the electrode. Charging current is high where local current was low. Inset shows the position of the charging current peak through the electrode over time. c. Charge stored through the electrode over time. In all plots:  $\diamond$  - 63 s,  $\triangle$  - 100 s,  $\square$  - 159 s,  $\circ$  - 251 s,  $\times$  - 398 s,  $\nabla$  - 631 s,  $\star$  - 1000 s,  $+$  - 1585 s. .... 106

Figure 4.7 Constant current discharging at  $225 \text{ A/m}^2$ . a. Voltage versus the current collector as a function of the distance away from the separator and plotted over time. Deviations of the solid experimental data lines from the dashed uniform charging analytical solution lines suggest non-uniform charging in the electrode. b. Local current plotted as a function of distance through the electrode. Higher currents near the separator suggest most discharging taking place here. c. Volumetric discharging current through the thickness of the electrode. Discharging current is high where local current was low. In all plots:  $\triangle$  - 25 s,  $\circ$  - 35 s,  $\diamond$  - 50 s,  $\square$  - 71 s,  $\nabla$  - 100 s,  $\times$  - 141 s,  $\bullet$  - 200 s,  $\triangleleft$  - 282 s,  $+$  - 398 s,  $\triangleright$  - 537 s. .... 110

Figure 4.8 Spatio-temporal plot of the volumetric discharging current. Each color represents the amount of discharging current at a given tab and amount of time through the experiment. The majority of the discharging occurs in the half of the electrode closest to the separator. .... 112

Figure 4.9 Distribution of voltage (a.) and local current (b.) during a constant  $169 \text{ A/m}^2$  discharge of the cell. .... 113

Figure 4.10 Distribution of voltage (a.) and local current (b.) during a constant  $112 \text{ A/m}^2$  discharge of the cell. .... 114



Figure 5.1 a. Schematic of the ionic ES cross-section showing alternating sensing and insulating layers on the negative electrode. An example of an electrolyte filled well and a RE is also shown. b. Photo of the fully assembled ionic ES including Hg/Hg<sub>2</sub>SO<sub>4</sub> reference electrodes (top left). Close up top views of the ionic ES (bottom left) and the top compression plate (right) are also included. .... 120

Figure 5.2 a. CV cycled at 0.1 mV/s from -0.9 V to 0.9 V. Integration of the curve leads to a calculated capacitance of 31 F/g. b. EIS conducted from 1 MHz to 30  $\mu$ Hz with a 10 mV perturbation. The calculated capacitance matches well with the CV data at 33 F/g and the effective conductivity is estimated to be about 1.4 S/m. .... 123

Figure 5.3 a. Distributions of ionic potential (vs. the negative current collector) at 10 logarithmically distributed times during constant current charging at 76 A/m<sup>2</sup>. The dashed lines are fits to the analytical solution for uniform charging and conductivity. Deviations between the experimental and analytical lines indicate non-uniform charging. The negative electrode inset depicts the orientation of the electrode and location of the sensing layers. Symbols denote the times plotted:  $\circ$  - 25 s,  $\nabla$  - 50 s,  $\square$  - 100 s,  $\triangle$  - 159 s,  $\times$  - 251 s,  $\triangleleft$  - 398 s,  $\bullet$  - 631 s,  $\triangleright$  - 1000 s,  $+$  - 1585 s,  $\diamond$  - 2512 s. b. Raw data of the voltage-time series of the cell during charging. .... 127

Figure 5.4 Constant current charging at 76 A/m<sup>2</sup>. a. Local current plotted as a function of the distance away from the separator at 10 logarithmically distributed times. Higher ionic current near the separator initially, indicates charging in this area of the electrode only at these short times. b. The absolute value of the volumetric charging current through the thickness of the electrode is plotted here. Again it is seen that most of the charging current is localized near the separator at short times. At longer times, the charging current begins to level out, suggesting uniform charging at these times. Inset shows volumetric charging current vs. distance away from the separator vs. time. c. Amount of charge stored through the thickness of the electrode. Inset shows charge stored vs. distance away from the separator vs. time. In all plots:  $\circ$  - 25 s,  $\nabla$  - 50 s,  $\square$  - 100 s,  $\triangle$  - 159 s,  $\times$  - 251 s,  $\triangleleft$  - 398 s,  $\bullet$  - 631 s,  $\triangleright$  - 1000 s,  $+$  - 1585 s,  $\diamond$  - 2512 s. .... 133

Figure 5.5 Charge distributions for three current densities (absolute values plotted). a. Distributions at a total cell charge for 50 mC. b. Distributions at a total cell charge of 100 mC. c. Distributions at a total cell charge of 150 mC. Larger current densities result in the most non-uniform distributions. All distributions are more uniform at higher amounts of cell charge. Note that the full length of the error bars is not shown, but they are all symmetric. In all cases:  $\nabla$  - 38 A/m<sup>2</sup> (C/2),  $\diamond$  - 50 A/m<sup>2</sup> (2C/3),  $\square$  - 76 A/m<sup>2</sup> (1C). .... 137

Figure 5.6 Effectiveness factor,  $\beta$ , as a function of current density at three levels of charge stored. .... 140

Figure A.1 Titration curve showing the pH of the Nafion solution as sodium hydroxide is added to the solution. The x-axis is the ratio of moles of sodium added to the moles of hydrogen that started in the solution. .... 154

Figure A.2 Typical CV curves for a Nafion electrode. In this case a 5 wt % Nafion electrode was used. The scan rates used were 0.1 mV/s (blue), 0.2 mV/s (black), 0.5 mV/s (red), 1 mV/s (green) and 2 mV/s (purple).....155

Figure B.1 Macro-structuring an electrode by adding through-thickness holes. The left side shows a schematic of a side view of an electrode with holes drilled into it and the relevant length scales that influence charging. It is assumed that the ion transport through the electrolyte filled hole is sufficiently fast such that the charging depth would be a uniform distance into the electrode from every surface. An image of an electrode with a 500  $\mu\text{m}$  hole is shown on the right. The hole remained visibly unchanged after testing.....160

Figure B.2 The active volume ratio between an electrode with a 500  $\mu\text{m}$  hole and a similar electrode with no hole is plotted. The depth of the hole and the depth of charging were varied parametrically to assess the effects on the active volume ratio.....161

Figure C.1 Schematic of a platinum MES used for sensing oxygen partial pressure in the cathode catalyst layer of a PEM fuel cell.....167

Figure C.2 Time series of UME current for the UME located 7.5  $\mu\text{m}$  from the membrane. The cell was held at 0.175 V, in the limiting current regime, as the oxygen concentration in the inlet air (listed on figure as a fraction of  $c_{O_2}$  in air) was varied every 60 s. The inset shows the reverse scan from CV conducted on the UME located 42.3  $\mu\text{m}$  from the membrane (scan rate 5 mV/s). A transport-limited region can be seen around 0.2 V.....169

Figure C.3 Dimensionless oxygen concentration values are plotted versus distance through the electrode. Measurements were made at each UME one at a time while the cell was operating at 450 mA/cm<sup>2</sup> and 50% RH. A schematic of the fuel cell cathode is shown below the x-axis, corresponding to the direction in which the measurements were made. The error bars represent one standard deviation. The dashed line is the analytical solution to the mass conservation equation derived from Fick's law.....171

# Chapter 1

## Introduction

### 1.1 Motivation

The United States makes up less than 5% of the world's population, but it consumes 23% of the world's petroleum, while producing only 9% [1, 2]. This high consumption of petroleum is costly and takes a toll on the U.S. economy, national security and environment. It has been estimated that the U.S. spends between \$15-47 billion in a year (2004) in military expenditures to protect its foreign reserves [3]. Additionally, the consumption of petroleum leads to the production of greenhouse gases, such as carbon dioxide, which are largely responsible for global warming. Concentrations of carbon dioxide in the atmosphere are higher today than any time in the last 650,000 years. Continuing to release greenhouse gases into the atmosphere at the current rate, thereby increasing the effects of global warming, could lead to dangerous environmental situations such as increased heat waves, droughts and rising sea levels [4].

One possibility for combating climate change is to develop a “green” energy infrastructure using electrochemical energy conversion and storage devices. A “green” energy grid consisting of windmills and solar panels, for example, may pose difficulties due to the intermittent power sources. However, when production rates are high the excess energy could be temporarily stored as chemical energy to be used when these intermittent power sources cannot meet demand. When the energy is needed, an electrochemical energy conversion or storage device, such as a fuel cell, capacitor or battery, would convert the chemical energy into electrical energy. On the grid, this energy could be used for a task such as load leveling or incorporating off-grid renewables as discussed. Off the grid these devices have many applications as well, such as powering anything from cell phones to back up generators. Additionally, fuel cells, capacitors and batteries are being studied as replacements for combustion engines in vehicles as they have much higher efficiencies and produce zero tailpipe emissions. Unfortunately, these devices are still limited as they are often costly and have relatively short lifetimes [5-8].

The high cost of these devices is often due to under utilization of the electrode materials, which arises due to poor through-plane transport of the reactants. For example, a significant number of platinum (Pt) particles in polymer electrolyte membrane (PEM) fuel cell catalyst layers are unreachable to hydrogen, oxygen or electrons, which leads to these reaction sites being inactive. If through-plane transport for these reactants could be improved, the Pt particle utilization would increase. This would lead to lower required loadings of the costly Pt particles to attain the same

performance, thereby decreasing the cost of the fuel cell. However, there are still many unknowns regarding through-plane transport making it difficult to determine which methods will lead to the largest performance improvements. This work discusses a novel method for making through-thickness potential measurements to study transport in porous electrode materials and assess possibilities for improving their performance.

## **1.2 Polymer Electrolyte Membrane Fuel Cells**

Polymer electrolyte membrane (PEM) fuel cells are a particular type of fuel cell that convert hydrogen and oxygen into water, heat and electricity. They are particularly advantageous for transportation applications since they operate at relatively low temperatures and only require one reactant to be carried on board since oxygen can be obtained from the air. However, PEM fuel cells still face many cost and performance limitations due to poor through-plane transport, especially in the cathode catalyst layer. This section will discuss how PEM fuel cells operate and a number of common characterization techniques used to assess their performance.

## 1.2.1 Standard Operation

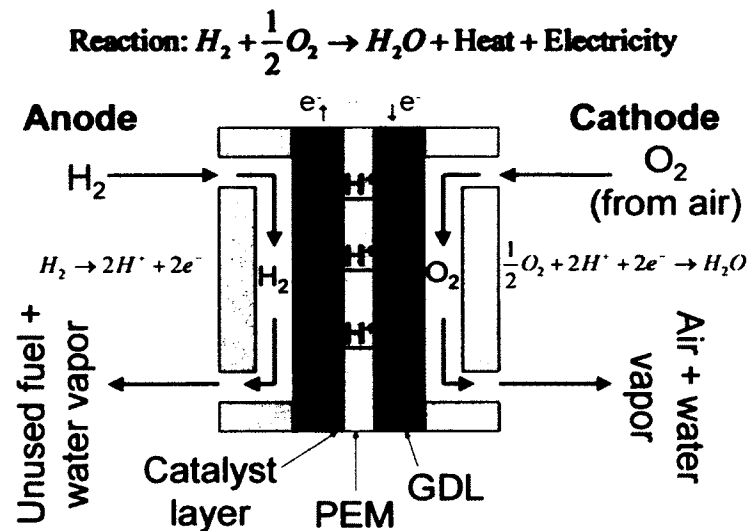


Figure 1.1 Schematic of a PEM fuel cell using hydrogen and air to produce electricity with water and heat as byproducts.

PEM fuel cells take in hydrogen at the anode and oxygen at the cathode, combining them to produce electricity, with water and heat as byproducts. Figure 1.1 shows how hydrogen gas fed to the anode, diffuses through a gas diffusion layer (GDL) to the electrode (often referred to as the catalyst layer) where the oxidation reaction splits it into hydrogen ions and electrons. The electrons, which cannot penetrate the PEM, flow out of the cell through an external circuit, thereby generating electric current. Hydrogen ions pass through the membrane where they react with oxygen and electrons at the cathode catalyst layer to produce water. Although the anode reaction is rapid, the overall reaction rate of the cell is severely restricted by the sluggish oxygen reduction reaction (ORR) kinetics.

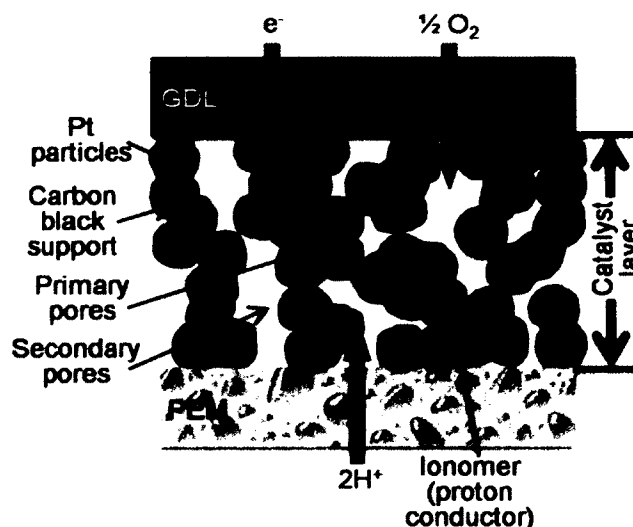


Figure 1.2 Schematic of a PEM fuel cell cathode. Protons from the anode cross the PEM and electrons travel through an external load. They react with oxygen at Pt catalyst particles, producing water according to the ORR. The oxygen is delivered from the gas channels through an adjacent porous carbon GDL.

Figure 1.2 illustrates the cathode catalyst layer where the sluggish ORR occurs. This figure depicts the primary aggregates of carbon supported Pt catalyst particles bound by a Nafion ionomer film that make up the porous agglomerate structure [9-11]. Between the agglomerates are larger secondary pores and within the agglomerates are smaller primary pores. Protons travel through the ionomer while electrons travel through the carbon black and Pt particles. Oxygen enters from the GDL and travels across the electrode through the secondary pores. It then locally dissolves into, and diffuses through, the Nafion film to meet the protons and electrons at a triple-phase boundary point on a Pt particle surface [12]. The ORR kinetics are sluggish due to the need for hydrogen ions, oxygen and electrons to meet at these triple-phase boundary points in order for a reaction to occur [12]. Because each of the reactants travels

through a different type of transport media it is difficult to balance the quantities of ionomer, carbon particles and void space that are required to reach performance goals. In general, if ionomer is added to a fixed volume of catalyst layer, the transport of hydrogen is improved; however, there is less void space, which hinders the transport of oxygen. In this case, the fuel cell would be prone to becoming oxygen transport limited, which would result in most of the reactions occurring near the GDL where the oxygen is most abundant. Similarly, if ionomer were removed from a fixed volume of catalyst layer, this would create more void space, improving the transport of oxygen. However, the catalyst layer would likely become proton transport limited and, consequently, most of the reactions would occur near the membrane. In both of these cases, many Pt catalyst sites would be inaccessible to the reactants and would therefore remain unused.

Despite the catalyst layers being thin ( $< 50 \mu\text{m}$ ), large variations in oxygen concentration, electrolyte potential, and reaction rates can develop across the thickness due to the transport limitations previously discussed. Transport resistances arise from the intrinsic resistance of the electrode materials, as well as from the fractional volume and tortuous pathways of the transport media [10]. In addition, the Nafion's protonic resistance is highly sensitive to hydration and increases sharply under drier conditions. These resistances again lead to regions near the GDL and the PEM becoming proton and oxygen limited prone, respectively. Further characterization of PEM fuel cell electrodes is required to better understand and lessen the effects of through-thickness



distributions so that the Pt catalyst particles can be used more effectively and costs can be cut.

## **1.2.2 Common PEM Fuel Cell Performance Characterization Methods**

There are a number of methods by which researchers assess the performance of a fuel cell. Some of the most common experimental techniques include polarization curves, cyclic voltammetry and electrochemical impedance spectroscopy. Additionally, many researchers employ models to predict how fuel cells will perform under various operating conditions. There are still many cell parameters that these techniques cannot provide, however, they do offer much insight into the workings of the cell none-the-less and are often used as baseline tests before conducting new experimental techniques. This section will give an overview of two of these commonly used techniques, polarization curve analysis and cyclic voltammetry, that were used to do fuel cell baseline tests. Other common testing techniques such as electrochemical impedance spectroscopy (EIS) and current interrupt, will not be discussed as they were not employed to analyze the fuel cells in this work, but information on these techniques can be found in many other sources including references [13-19].

### **1.2.2.1 Polarization Curves**

Polarization curves are one of the most common techniques used to characterize the performance of a fuel cell. These tests relate the current to the voltage and provide

insight into the three main types of losses occurring in the cell; activation polarization losses, Ohmic losses and concentration polarization losses. Polarization curves are obtained by running the cell through a series of galvanostatic (constant current) or potentiostatic (constant voltage) holds and measuring the subsequent voltage or current, respectively. The shape of the resulting polarization curve shows how much of an impact overpotential losses have on the performance of the fuel cell.

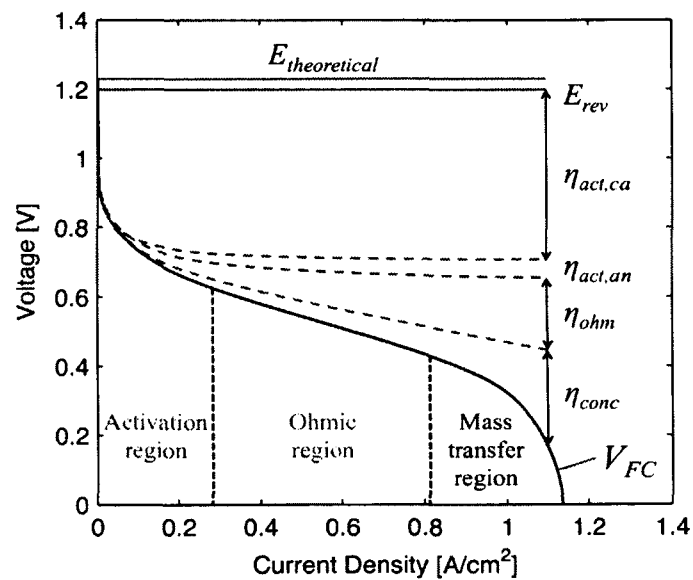


Figure 1.3 A typical polarization curve for a PEM fuel cell operating under standard conditions. The dashed curves show loss of voltage associated with the overpotentials. The activation polarization losses, ohmic losses and concentration polarization losses affect the shape of the polarization curve most notably in the accompanying regions.

Figure 1.3 shows a typical polarization curve and denotes important aspects that are considered when analyzing the cell performance. First, as with many chemical reactions, there is a theoretical maximum potential that can be reached based on the Gibbs free energy of the components involved in the reaction, in this case hydrogen

and oxygen. This potential,  $E_{theoretical}$ , is calculated to be 1.23 V for a hydrogen/oxygen fuel cell. We would expect to find that this theoretical voltage would be nearly equal to the open circuit voltage (OCV) of the cell since the OCV is measured when the cell is being supplied with reactant gases, but the electrical connection is open so there would be no losses associated with current through the cell. However, the OCV is often under 1 V due to irreversibilities in the cell. One reason for the irreversibilities may be from side reactions such as platinum oxidation or the formation of hydrogen peroxide occurring in the cell. The reversible potential of the cell can be measured at OCV and typically decreases over time as the catalyst layers degrade with use. Once a load is applied to the cell, we see a steep drop-off in voltage over a very slight increase in current. This initial voltage loss is due to activation overpotentials, which are related to the amount of energy required to begin the chemical reaction. While there are activation overpotentials associated with both the anode and the cathode, the hydrogen oxidation reaction at the anode occurs much more readily than the ORR at the cathode. This results in the cathode activation overpotentials being responsible for the majority of losses in this section of the polarization curve. As the current is increased or the voltage is decreased, the cell performance begins to decline due to Ohmic losses that arise from contact resistances between cell components, ion transport resistances through the membrane and ionic phase of the catalyst, and electron transport resistances through the current collector, external wires and electric phase of the catalyst. Finally, we will eventually begin to see losses due to concentration overpotentials. These losses are related to mass transport resistances that develop during cell operation often due to either an increase of water in the cathode,

which fills the void space and hinders oxygen transport, or dry out of the Nafion ionomer, which reduces that conductivity of the Nafion and impedes the transport of hydrogen ions.

It is important to note that the regions denoted in Figure 1.3 for each loss mechanism are merely guidelines. The losses often overlap with one another making it difficult to diagnose the specific cause of the performance losses from just the polarization data. Additionally, there are other sources of losses, such as hydrogen cross-over, which were not discussed that can be difficult to detect from the polarization curve data. Polarization curves are one useful, well-accepted and simple method for observing the overall performance of a particular fuel cell, but other methods are needed to expand upon the data and obtain a more in depth characterization of the cell.

#### 1.2.2.2 Cyclic Voltammetry

Cyclic voltammetry (CV) is another common characterization technique for PEM fuel cells. CV scans can provide information about the electrochemically active surface area (ECSA) of the catalyst layer, detect the presence of certain species and easily identify hydrogen cross-over. For PEM fuel cells, CV scans are generally conducted with fully humidified  $H_2$  gas flowing through the anode and a fully humidified inert gas such as nitrogen flowing through the cathode. It is important to completely purge the cathode with the  $N_2$  gas so there is no oxygen left to react with the hydrogen. A potentiostat is used to conduct galvanostatic or potentiostatic sweeps while voltage or current data is measured. The cell temperature, scan rates and gas flow rates used can

vary and must be chosen carefully as they influence the results [20-22]. The CVs in this work were conducted at a cell temperature of 30 °C using fully humidified gases flowing at 0.1 slpm on the anode side and 0.2 slpm on the cathode side. Potentiostatic sweeps were conducted between 0 and 0.8 V at a rate of 40 mV/s. A typical CV run under these conditions is shown in Figure 1.4.

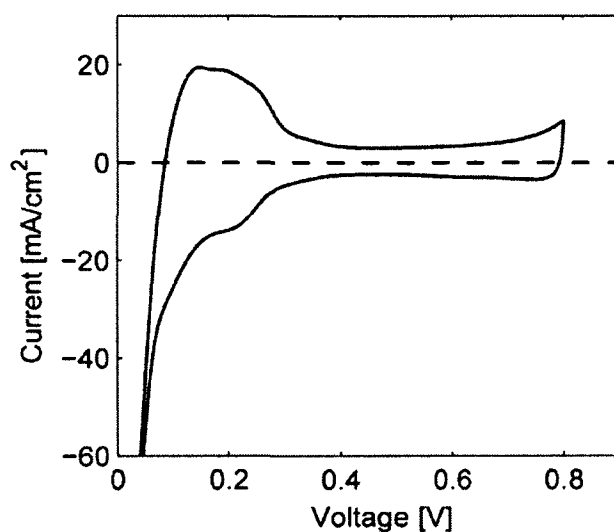


Figure 1.4 CV performed on a 1 cm<sup>2</sup> MEA. The cell and gas humidifiers were all held at 30 °C and a voltage sweep was conducted from 0 to 0.8 V at a rate of 40 mV/s.

There are a number of events that occur during the CV cycle. First, during the forward sweep (0 to 0.8 V, top line) there is an initial spike in the current, which denotes desorption/oxidation of hydrogen from the platinum catalyst. The current then flattens, representing the current due to charging the capacitive double layers (DL). Finally, there is a small spike around 0.8 V, which may be indicative of the start of platinum oxidation. On the reverse sweep (0.8 to 0 V, bottom line), any platinum that may have

been oxidized is reduced, the DL is discharged and hydrogen is adsorbed/reduced onto the platinum surface again. The two regions of highest interest for this plot are the hydrogen adsorption region, between about 0.42 and 0.06 V during the reverse sweep, and the DL region that begins after about 0.42 V. Consider the DL charging region first. The double layer current is easily determined from the plot as half of the absolute difference between the currents measured during the forward and backward sweeps in this flat region of the curve. If there is no hydrogen crossover in the cell, this region of the curve will be perfectly centered around 0 mA/cm<sup>2</sup>. However, if there is hydrogen crossover, a hydrogen evolution reaction will occur, producing current and offsetting the DL currents. The current associated with this reaction can be determined by finding the offset of the center of the DL currents from the zero current line as the DL currents will always be symmetrical about the crossover current. In Figure 1.4 the DL currents seem to be well centered around the zero current line, indicating little to no hydrogen crossover.

Next, the data from the hydrogen adsorption region of the curve along with equation [1.1] can be used to determine the ECSA of the catalyst. The platinum loading,  $L$  [g Pt/cm<sup>2</sup>], is a known experimental value based on the composition of the catalyst layer and  $\Gamma$  is a constant equal to 210  $\mu\text{C}/\text{cm}^2_{\text{Pt}}$ , that represents the charge required to adsorb a monolayer of protons on the platinum surface. It is assumed that once a monolayer of protons forms on the platinum surface there is no more room for activity. Therefore, the only unknown is the amount of charge transferred,  $q$ , which can be determined from the CV data. The amount of charge transferred is determined

by doing a time integration of the current during the reverse sweep in the region in which hydrogen is being reduced. The integration region is determined by extending a horizontal line from the reverse sweep DL current all the way to the y-axis. The integration is then performed to determine the area that falls between this line and the reverse sweep curve and the result is the charge transferred in Amp-seconds, or Coulombs. It is important to note that this integration purposefully excludes the DL current as this is an underlying current that is always present, but does not provide information on the amount of charge transferred. Finally, the charge transferred must be normalized by the area of the membrane electrode assembly (MEA) and can then be used to calculate the ECSA.

$$ECSA [cm^2 Pt/g Pt] = \frac{q}{\Gamma L} \quad [1.1]$$

The value of the ECSA is an indication of the fuel cell's performance. In general, a higher ECSA means that more of the platinum is accessible and active, which in turn means that the performance of the fuel cell will likely be higher. It can also be an indication of catalyst degradation over time if subsequent CVs run on the same cell have decreasing ECSA values. Furthermore, if there are any unexpected peaks in the CV this may suggest that unwanted species are present in the catalyst. The CV results can be used with the polarization curve results to start building a more complete picture of the reactions taking place within the fuel cell.

## 1.3 Hybrid Batteries and EDL Capacitors

The aqueous sodium hybrid battery is an interesting new technology that is being studied with a focus on improving the volume and quality of grid scale energy storage. This technology is particularly attractive because it uses only environmentally friendly, benign materials and combines high power from a battery electrode with large storage from a capacitor electrode. Unfortunately, the performance and commercial viability of this battery suffer due to poor through plane transport, which is most severe in the negative electric double layer (EDL) capacitance electrode. This section will provide an overview of standard hybrid battery operation and common characterization techniques used to assess performance.

### 1.3.1 Standard Operation

Hybrid batteries are referred to as such because they combine an intercalation electrode, typically used in batteries, with an electric double layer (EDL) capacitance electrode, typically found in capacitors. Aqueous sodium hybrid batteries in particular, feature a Na-ion based positive intercalation electrode and use an aqueous sodium electrolyte. One example, which is shown in Figure 1.5, is the aqueous sodium hybrid battery that was developed by Whiteacre et al. [23] It uses  $\text{Na}_4\text{Mn}_9\text{O}_{18}$  for the intercalation positive electrode and activated carbon for the negative electrode in combination with  $\text{Na}_2\text{SO}_4$  as the aqueous sodium electrolyte. In the positive electrode during charging, ions diffuse through the  $\text{Na}_4\text{Mn}_9\text{O}_{18}$  and incorporate themselves into the crystal structure of the material via the intercalation sites. In the negative



electrode, Na-ions diffuse through the electrolyte-filled pores in the activated carbon and store charge by electrostatically adsorbing at the negatively charged carbon surface. There are, unfortunately, many losses associated with transport through the negative electrode and it is here that improvements must be made.

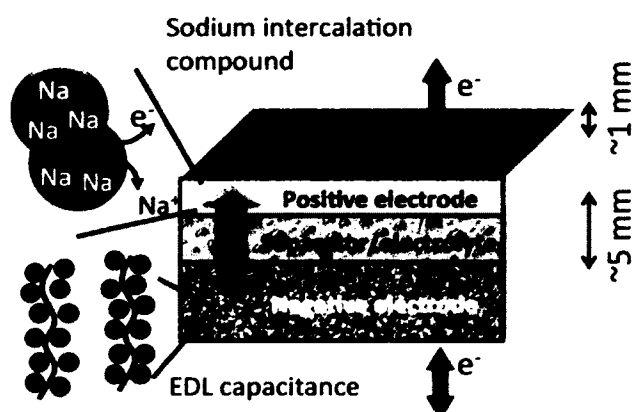


Figure 1.5 Schematic of an aqueous sodium hybrid battery. The positive electrode is a sodium intercalation material similar to the positive electrode of a Li-ion battery. The negative electrode is made from an EDL capacitance material, such as activated carbon, typically found in EDL capacitors.

The losses in the negative electrode are due to the finite mobilities of the ions, and thicker electrodes are associated with higher losses. This issue is particularly unfortunate because the negative electrode has a lower volumetric energy density than the positive electrode and must therefore be made thicker in order to properly balance the accessible charge-storage capacities between the two electrodes [24]. Furthermore, one cost cutting technique that would improve the commercial viability of hybrid batteries is to increase the thickness of both electrodes so that more charge can be stored with less geometric area thereby decreasing the amount and cost of non-

functional materials needed for the cell (i.e. separator, current collector, packaging, etc.) [6, 7, 24, 25]. For this reason, the following research will focus on the negative electrode|electrolyte system for this hybrid battery where the most improvements must be made. In order to simplify testing procedures and implementation, the cell will be operated as a symmetric EDL capacitor.

Figure 1.6 shows a cross-section schematic of the symmetric EDL capacitor used in this study during charging. Charging occurs when a positive voltage is applied to the cell's positive electrode and electrons begin to travel away from the positive electrode towards the negative electrode. A positive surface charge forms in the positive electrode, while a negative surface charge forms in the negative electrode. These surface charges then begin to attract sulfate and sodium ions from the electrolyte, respectively. It is believed that the charging begins quickly with ions filling unoccupied sites in the material near the separator. However, the charging likely slows over time as the ions must travel further through the electrode to find unoccupied charge sites, leading to difficulties in fully utilizing the electrode. Further characterization of the EDL capacitor electrode must be conducted to study and improve transport rates, and thereby the performance, of thick electrodes. This will lead to lower costs of non-functional materials, making the EDL capacitor electrodes more economically viable in grid-scale energy storage technology.

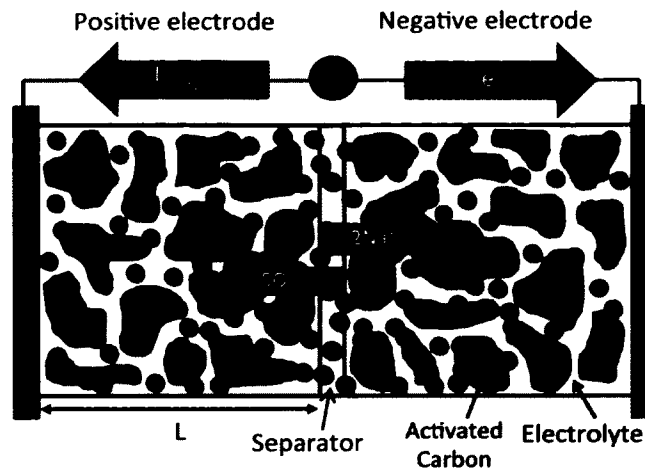


Figure 1.6 Cross-section of a symmetric EDL capacitor during charging. When a voltage is applied to the cell, electrons leave the carbon in the positive electrode and travel into the negative electrode carbon creating a positive surface charge and a negative surface charge, respectively. The electrolyte then breaks down with the sodium and sulfate ions being respectively drawn towards the negative and positive electrodes. It is believed that charging begins in the region next to separator and moves outwards towards the current collectors.

### 1.3.2 Common Performance Characterization Methods

There are many techniques commonly applied to assess the performance of batteries and capacitors. Many of these techniques, such as CV, EIS and modeling are similar to those used to evaluate fuel cell performance, but others, such as charge/discharge cycling, are different. As with fuel cells, these techniques provide many interesting insights, but only convey part of the picture. Again, they are often used as baseline tests when new techniques are being employed. This section will provide an overview of three different techniques, CV, EIS and charge/discharge cycling that were implemented as baselines tests.

### 1.3.2.1 Cyclic Voltammetry

CV, which was discussed with regards to characterizing fuel cells in section 1.2.2.2, is also a common technique for characterizing capacitors. Just as with fuel cells, a potentiostat is used to conduct potentiostatic sweeps and the resulting capacitor current is measured. The data gathered from the CV can be used to determine the capacitance of the EDL capacitor. When applying this method to capacitors, we do not have reactant gases to be concerned with and only need to carefully consider the scan rate as this can significantly change the shape of the curve and will therefore affect our capacitance calculations [26, 27]. A very slow scan rate was required to obtain a reasonable estimate of the capacitance of the ultra-thick electrodes used in this work. Figure 1.7 shows the result of a CV conducted at a scan rate of 0.1 mV/s and swept between -0.9 to 0.9 V. The CV curve shown in this figure is rectangular in shaping indicating it is exhibiting nearly ideal capacitor behavior. An ideal capacitor would charge and discharge the EDLs instantaneously, the EDL current would remain constant throughout the potential sweep and it would be perfectly centered about the x-axis. Deviations from the ideal are indicative of losses or unwanted reactions occurring in the cell. For example, the slight off-vertical slope of the curve during the initial charging is denotes some amount of ion transport resistance hindering the cell's ability to quickly charge the EDLs completely. Another example would be if the curve were not centered around the x-axis it would indicate the presence of a side reaction occurring within the cell during charging and discharging, although that is not seen in this figure.

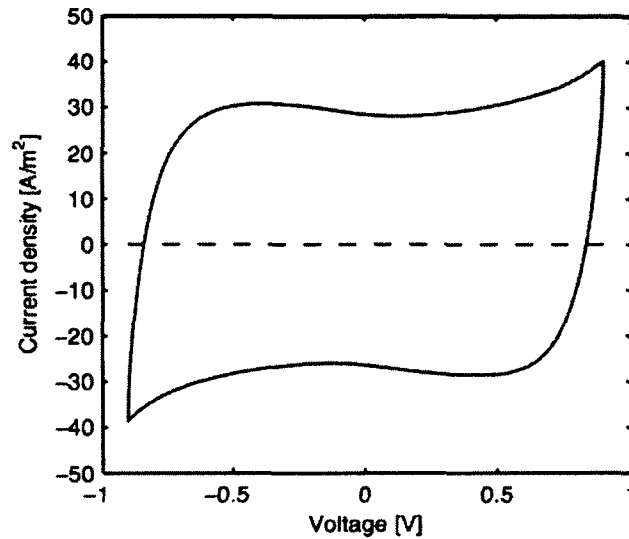


Figure 1.7 A typical CV curve for an EDL capacitor. This is the result of a CV conducted on an EDL capacitor with ultra-thick electrodes. The voltage was swept between -0.9 and 0.9 V at a scan rate of 0.1 mV/s.

The capacitance of the EDL capacitor can be determined from the CV data. Equation [1.2] shows us that the capacitance,  $C$ , is related to the current,  $I$ , divided by the scan rate,  $dV/dt$ . To evaluate this equation we use an average current, which is obtained by integrating the area under the forward sweep curve and subtracting the integrated area under the backward sweep curve then dividing by the entire range over which the voltage was swept. Using that average current in conjunction with the known scan rate at which the CV was conducted, the cell's capacitance is easily calculated.

$$C = \frac{I}{(dV/dt)} \quad [1.2]$$

### 1.3.2.2 Electrochemical Impedance Spectroscopy

Electrochemical impedance spectroscopy (EIS) can be used to estimate porous electrode characteristics such as resistance and capacitance. EIS studies are conducted by applying a small voltage perturbation to the cell and measuring the impedance response. The voltage perturbations are generally on the order of 5-10 mV and are applied over a range of frequencies. For the thick electrodes discussed in this work, we covered a large range of frequencies from 1 MHz to 30  $\mu$ Hz using a 10 mV perturbation. A typical result from running EIS on an EDL capacitor using these parameters is shown in Figure 1.8. There are two distinct regions to this curve, the initial bounded Warburg-like response ( $45^\circ$  slope) of the electrode at high frequencies, which corresponds to the migration of ions through the electrode, and the subsequent vertical region seen at low frequencies, which is representative of the total capacitance of the electrode.

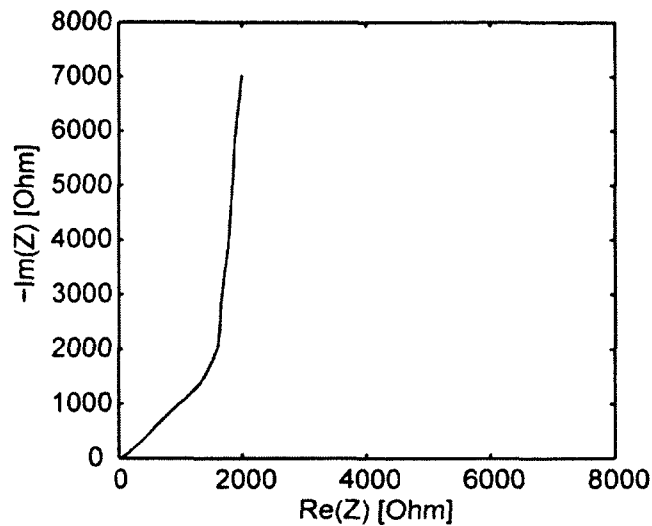


Figure 1.8 A typical EIS plot for an EDL capacitor. This data was obtained using a 10 mV perturbation over a frequency range of 1 MHz to 30  $\mu$ Hz.

In order to extract meaningful data from this curve, the data must be fit to an equivalent circuit. The accuracy of the estimated values for resistance and conductivity, etc. will be based on how well the equivalent circuit matches the system. For example, there is no obvious source of inductance in the electrode or a clear inductance loop seen in Figure 1.8 therefore, adding an inductance term to the equivalent circuit would result in a poor fit. We considered our sources of resistance as well as the transport of ions through the electrodes and determined that the equivalent circuit,  $R1+M1$ , best suited this type of electrode. The  $R1$  term refers to the Ohmic resistance in the cell, while the  $M1$  term relates to the electrolyte resistance and a time constant for the electrode. This equivalent circuit can be inputted to the Bio-Logic Z Fit software and estimates for the Ohmic resistance, the electrolyte resistance and the time constant of the capacitor will be returned. The electrolyte resistance can be used, along with known cell parameters, to estimate the electrolyte conductivity

according to the equation:  $\sigma = L/AR_{e'lyte}$ . The time constant and the electrolyte resistance can then be used to estimate the capacitance using the relationship:  $C = \tau/R_{e'lyte}$ . This capacitance value can be compared to that determined from the CV to check for agreement and to build confidence in the goodness of the fit.

### 1.3.2.3 Charge/Discharge Cycling

EDL capacitors can also be characterized by analyzing their charge/discharge cycles. During a charge/discharge cycle, the capacitor is generally held at a constant current or a constant voltage until a predetermined stopping point is reached. This stopping point could be a certain voltage or current reached, a state of charge reached or a specified quantity of time for example. An example of a typical charge cycle is shown in Figure 1.9. In this case, the capacitor began in a completely discharged state and was charged at a constant current of  $76 \text{ A/m}^2$  until it reached  $0.7 \text{ V}$ . This can be used as yet another method to calculate the capacitance of the cell through the use of equation [1.3]. In this equation,  $Q$  is the charge storage capacity,  $I$  is the current used to charge the cell,  $dV$  is the total potential change over the entire cycle,  $C$  is again the capacitance of the cell and  $dV/dt$  is the change in voltage over time, which is determined from the slope of the linear section of the curve. As with the CV tests, the rate at which the capacitor is charged or discharged will affect the capacitance calculated from this method [26, 28]. In addition to providing information about the capacitance, the steep slope seen at early times in this plot also shows how the capacitor's performance is altered due to internal resistances [29]. The



charge/discharge cycles give an overview of the capacitor's performance and provide additional evidence that can be used in conjunction with the methods previously discussed to characterize the cell.

$$Q = \int_{t_1}^{t_2} \frac{I}{\left(\frac{dV}{dt}\right)} dV, \text{ where } C = Q/dV \quad [1.3]$$

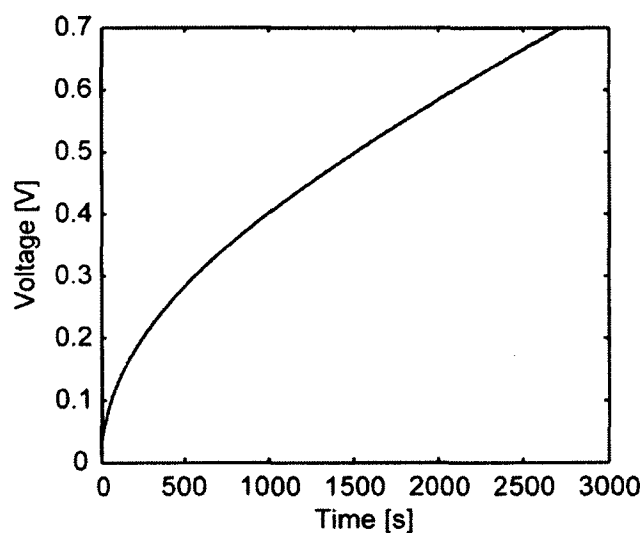


Figure 1.9 Example of a charge cycle for an EDL capacitor. This cell was charged at a constant current of  $76 \text{ A/m}^2$  from 0 to 0.7 V.

## 1.4 Related Work

There are many important applications for fuel cells, capacitors and batteries. Implementing these devices in our electronics, vehicles and as stationary storage would have major positive impacts on the economic and environmental well being of

the United States and the rest of the world. However, the relatively high costs and low performance of these technologies currently prohibit them from widespread use and commercialization. Research being conducted on porous electrodes continues to improve performance and lower costs, but DOE goals have not yet been reached for these technologies.

Common experimental methods, such as the ones discussed in the previous sections, are useful for globally characterizing porous electrodes, but the information they provide does not readily translate into methods for improving the electrode performance. Many experimental and modeling studies have specifically focused on ways to improve materials, relative composition, and the morphology of fuel cell, capacitor, and battery electrodes in order to combat the myriad of transport resistances that cause limited performance in these porous electrodes [11, 23, 25, 30-36]. Unfortunately, many of these existing electrochemical diagnostic methods again face a significant limitation in that they only interface with the electrodes as either surfaces or bulk volumes and often provide data based solely on cell terminal measurements. Furthermore, many of these techniques are conducted under non-standard operating conditions or are performed *ex situ*, such as in a rotating disk electrode (RDE) setup. In the last decade, however, a few techniques for gathering *in situ* measurements in PEM fuel cells and batteries have been developed.

Multiple *in situ* studies have been conducted on PEM fuel cell MEAs. Büchi et al. [37], pressed gold wires between Nafion membranes to measure the through-plane

resistance distributions during operation and found higher resistances on the anode side of the membrane than the cathode side. Another group, Takaichi et al. [38], used Pt wire probes placed within the membrane to measure the oxygen partial pressure distribution. Finally, Piela et al. [39] studied several reference electrode (RE) placements to determine the optimal technique for separating the anode and cathode potentials in an MEA. While these studies provide vital information about the operations of working fuel cells, the methods that were developed for these experiments are not transferrable to studying distributions in the cathode catalyst layer of a PEM fuel cell. The probes discussed are generally as thick or thicker than the catalyst layer itself, which would result in a major disturbance on the macroscopically one-dimensional transport as well as make it impossible to have multiple probes in the thickness direction for gathering distribution data.

Other studies have been conducted on porous electrodes in Li-ion batteries to measure distributions and to gather a more comprehensive understanding of electrode charging and discharging cycles. Liu et al. [40] used synchrotron X-ray microdiffraction to obtain state-of-charge profiles, both in-plane and through-plane, in Li-ion battery electrodes. However, they had to “freeze” the charge distribution and conduct X-ray microdiffraction post-mortem, preventing transient measurements during discharging and charging. Additionally, this method required a large number of repeated, complex experiments. Harris et al. [41] used the color changing properties of graphite to visualize the insertion of lithium into the electrode as it charged. While this method enables transient visualizations, it is only semi-quantitative and is restricted to the Li-

ion|graphite electrode system. Ng et al. [42] developed a quantitative, multiple working electrode (MWE) method for measuring charging distributions. The MWEs, which each had their own mesh current collector and were electrically isolated from one another by using additional separators, were stacked on top of each other and used to obtain current density measurements at three points through the thickness of a Li-ion negative electrode. While Ng. et al. were the first to gather these types of distributions through a battery electrode, the separators and current collectors intrude significantly upon the normal electrode structure, and make it unrepresentative of those used in a typical Li-ion battery. In addition, the macroscale current collectors and separators limit the resolution of this approach and exclude this method from being applied to study PEM fuel cell electrodes. A recent study by Siegel et al. [43] used neutron imaging to look at the change in Li concentrations through a Lithium Iron Phosphate battery electrode during charging and discharging. They were able to visualize the changes in Li concentration, but there were a number of sources of uncertainty in their measurements, such as possible improper alignment and surface roughness. Additionally, the radiography imaging requires trade-offs between measurement accuracy and temporal resolution.

Despite these advances in experimental techniques, there are still, to the best of our knowledge, no *in situ* studies conducted on uninterrupted PEM fuel cell catalyst layers or EDL capacitor electrodes under standard operating conditions. Additionally, the *in situ* experiments conducted on Li-ion battery electrodes could be simpler, less costly and more general such that the techniques could be applied to multiple types of porous

electrodes. It is important to make *in situ*, through-plane measurements that provide local information for parameters such as potential, current and conductivity to ensure models have the most accurate data and to aid in determining how and why the performance of a cell is affected by a change in materials or structure. *In situ* measurements will allow for a more in depth understanding of the transport and reactions occurring in the electrode and will provide additional guidance for the development of new electrode materials and structures. To alleviate some of the issues found in current measurement techniques, we have developed a novel *in situ* measurement device that has allowed us to make some of the first *in situ*, through-plane measurements on representative porous electrodes during standard operation.

## 1.5 Method

Fuel cells and ultra-thick capacitors suffer from high transport losses through their electrodes during operation, which hinders the commercial viability and widespread adoption of these technologies. These issues could likely be resolved with improved electrode materials and architectures [44], however, there is a lack of experimental data gathered from within functioning electrodes due to the difficulty of accessing the electrode in a non-invasive manner during operation. Without this type of data it is difficult to determine which materials and architectures will result in the largest performance improvements.

Many current theories about how electrodes function during operation are derived from analytical solutions and conjecture. For example, we believe there is a potential distribution that develops in electrodes during operation. In fuel cells this is due to hydrogen ions being consumed in a through the thickness of the cathode catalyst layer as the ORR takes place. In a capacitor it arises as ions adsorb or desorb from surface charge sites as the cell is charged or discharged. To get an idea of what these distributions might look like, we apply current conservation through the use of equation [1.4]. In this equation,  $\sigma_{eff}$  is the effective conductivity of the electrode,  $\phi$  is the local potential,  $x$  is the distance through the electrode and  $j$  is the volumetric current. We can calculate an analytical solution to this equation, but we must make a few simplifying assumptions to do so. First we must assume that the reaction rate is uniform through the electrode such that  $j$  can be modeled as  $j = i/L$  where  $i$  is the area-specific current density and  $L$  is the length of the electrode. Additionally, we must assume that the conductivity is constant through the electrode. If we then apply appropriate boundary conditions for a given electrode we can eventually plot a curve such as the one seen in Figure 1.10. While our assumptions of uniform reaction rate and conductivity are unlikely to hold true in all scenarios, it is likely that we will see some distribution of potential through the electrode as shown in the figure.

$$\frac{\partial}{\partial x} \left( \sigma_{eff} \frac{\partial \phi}{\partial x} \right) = j \quad [1.4]$$

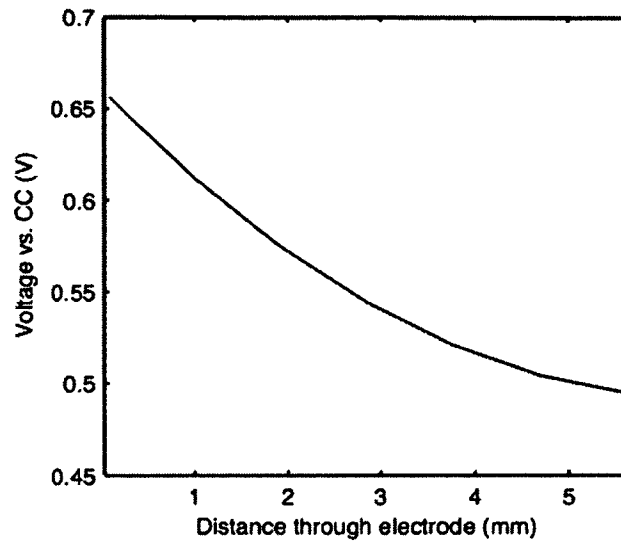


Figure 1.10 Example of an analytical solution to the current conservation equation for a porous electrode. It can be seen that a potential distribution develops through the thickness of the electrode during operation.

The shape of the distribution curve can provide valuable information that can lead to developing improved porous electrodes. For example, if a distribution curve could be obtained through the use of an *in situ* measurement device, it may be discovered that there is a steep initial drop in the potential followed by a flat section in the curve. This would indicate that only a small region of the electrode is being used and that much of the electrode material may be going to waste. Using this information we may find that we can remove a section of the electrode without decreasing performance and will therefore be able to cut costs. Or we may find that we need to improve conductivity in certain regions of the electrode to boost transportation in these areas and improve overall performance.

To address the need for experimental data gathered from within functioning electrodes, we have developed a device that allows for unobtrusive, *in situ*, through-thickness distribution measurements to be made within a fuel cell, capacitor or battery electrode during normal operation. A schematic of the device, which is referred to as an electric scaffold (ES), can be seen in Figure 1.11. The ES consists of alternating sensing and insulating layers that are stacked around a quasi 1-D column of electrode material. Each sensing layer contacts the electrode at a known, discrete distance through the electrode's thickness and is accessible to a data collection device. The insulating layers prevent crossover between the sensing layers and the 1-D column of working electrode ensures that the majority of transport is perpendicular to our sensing layers allowing us to easily measure the full potential drop through the electrode's thickness. This basic structure remains the same throughout, but the size and shape of the device are adjusted to accommodate the system being studied. Additionally, the insulating and sensing layer materials are altered to allow for different types of distribution measurements, such as electric potential or ionic potential. This method could also be used for species sensing within the electrode, however that is beyond the scope of this work. This rest of this dissertation will focus on using a microstructured version of this device (an MES) to study a PEM fuel cell electrode, as well as using both electric and ionic versions of the ES in symmetric EDL capacitor electrodes with applications for aqueous sodium hybrid batteries.



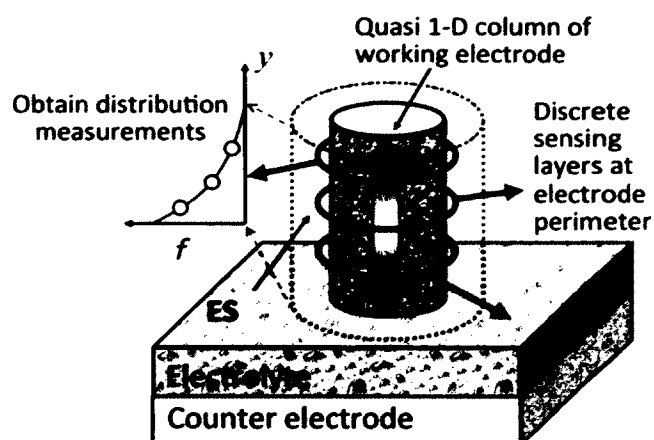


Figure 1.11 A schematic of the proposed device, which will allow for distribution measurements to be collected in porous electrodes.

## 1.6 Scope of Thesis

This dissertation discusses the use of a novel diagnostic tool for making *in situ*, through-thickness distribution measurements in porous electrodes used for PEM fuel cells, capacitors and batteries and considers methods for improving performance. The dissertation is divided into 5 additional chapters. Chapter 2 focuses on the application of an MES used to measure ionic potential in a PEM fuel cell cathode. Chapter 3 discusses a finite difference method developed to analyze the data gathered in chapters 4 and 5. In these chapters, an ES has been used to gather electric or ionic potential distribution measurements and the mathematical methods developed in chapter 3 have been applied to determine current, charging current and charge storage distributions from this data. Finally, chapter 6 reviews the conclusion and contributions of the completed research and makes recommendations for future work.

## **Chapter 2**

# **The MES as Applied to PEM Fuel Cell Electrodes**

Sluggish oxygen reduction reaction (ORR) kinetics lead to significant losses in the cathode catalyst layer of polymer electrolyte membrane (PEM) fuel cells. Despite the fact that these catalyst layers are typically on the order of about 10  $\mu\text{m}$  thick, substantial potential distributions can develop during operation. Understanding how and why these distributions occur can lead to a more thorough understanding of the reactions that take place in the catalyst layer, which will aid in developing improved catalyst layers in the future. To this end, we have developed a microstructured electrode scaffold (MES) to study the ionic potential distributions that develop within the cathode catalyst layer of a PEM fuel cell during standard operation. The design of the MES, and the results and analysis of the data gathered using it are discussed in detail in this chapter.

## 2.1 Experimental Setup

The MES consists of alternating sensing and insulating layers surrounding a 1-D column of working electrode material; the cathode catalyst layer in this case. A number of build iterations were experimented with before determining the best configuration for the MES. Insulating materials, thickness of sensing layers, and the number and diameter of the 1-D columns of catalyst layer were all varied during this initial iteration period. The final insulating material was chosen because of its relative ease to work with, thinness and low cost. Sensing layer thickness was determined by choosing the thinnest layer achievable that did not hinder the conductivity through the layer from the column of catalyst material to the measurement point. Finally, a single hole with a 170  $\mu\text{m}$  diameter was chosen for its simplicity and to ensure 1-D transport through the catalyst layer while maintaining negligible edge effects. Details of the MES build, catalyst ink preparation, MES hardware design and the equipment used for testing are discussed in the following sections.

### 2.1.1 MES Build

The MES was fabricated by spin coating a  $\sim 1$   $\mu\text{m}$  thick layer of Nafion from a 15 wt % Nafion solution (Ion Power, New Castle, DE) onto a 7.5  $\mu\text{m}$  thick sheet of Kapton (American Durafilm, Holliston, MA). Once dry, a laser engraver (Pinnacle, V-series) cut the bilayers to the desired shape: a square with a protruding tab on one edge. They were then stacked such that none of the protruding tabs overlapped, and a square of uncoated Kapton was placed on top, insulating the exposed Nafion layer.

The resulting 50  $\mu\text{m}$  thick stack was hot pressed at 2.8 MPa and 125  $^{\circ}\text{C}$  for 4 min. A 170  $\mu\text{m}$  diameter hole was then laser micromilled (New Wave, Fremont, CA) into the center of the stack. This diameter was chosen because it is small enough that transport through the electrode can still be considered nearly one-dimensional, but large enough to neglect edge effects and to easily permit hand painting of the catalyst ink. A scanning electron microscope (SEM) image of an MES with a 200  $\mu\text{m}$  diameter hole is shown in Figure 2.1a with a close up of the laser cut layers shown in Figure 2.1b. Additionally, Figure 2.1c shows a transmission electron microscope (TEM) image of an ultramicrotome slice of the MES substrate cross-section with nearly uniform, • 1  $\mu\text{m}$  thick Nafion sensing layers.

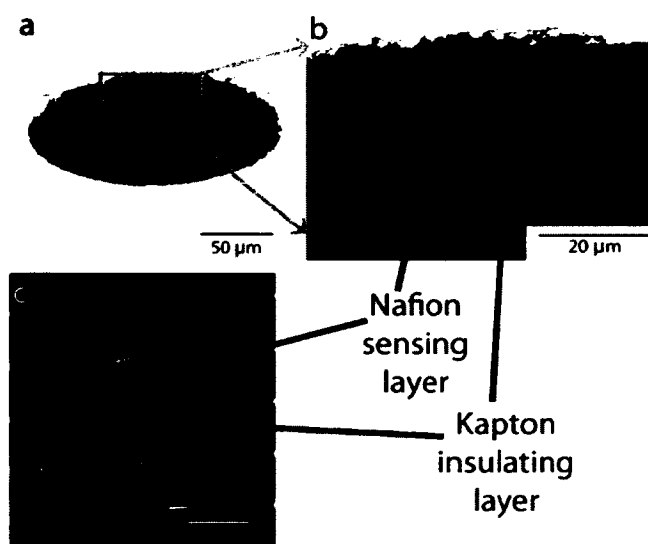


Figure 2.1 Electron micrographs of MES substrates. a. SEM image of a laser-cut hole in the MES, b. SEM image showing alternating Nafion (light) and Kapton (dark) layers inside of the hole, and c. TEM image of alternating Nafion and Kapton layers showing approximately uniform 1  $\mu\text{m}$  thick sensing layers.

To assemble the MES, a Nafion 115 membrane (Ion Power) and then a 0.4 cm<sup>2</sup> commercial gas diffusion electrode (GDE) (Electrochem EC-20-10-7 Electrode, Woburn, MA) impregnated with Nafion solution were adhered to the bottom of the MES stack by hot pressing at 125 °C for 4 min at 0.71 MPa and 70 kPa, respectively. Once the assembly was bonded, the catalyst ink was painted into the hole in the MES with the aid of a stereoscopic microscope and then dried at room temperature. The painting process was repeated until the hole was filled to the height of the MES. A schematic of the MES setup at this point in the process is shown in Figure 2.2 along with a wiring diagram. A 0.4 cm<sup>2</sup> conventional GDL (SGL-24BC, Ion Power) was then hot pressed to the top of the MES. Finally, during assembly a hydrogen reference electrode (HRE), made from the same GDE material as the anode, is placed on each protruding sensing layer.

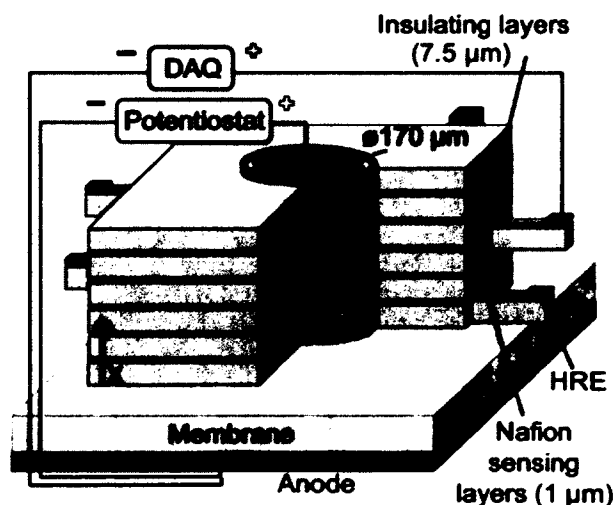


Figure 2.2 Schematic of the membrane electrode assembly for a PEM fuel cell with the MES being implemented.

### **2.1.2 Catalyst Ink Preparation**

Preparation of the catalyst ink was based on techniques used by Wilson and Gottesfeld [33]. A catalyst ink suspension was made by combining Pt/C catalyst (20% Pt/C on Vulcan XC-72R, HiSPEC 3000, Alfa Aesar, Ward Hill, MA), 5 wt % Nafion solution (DE-521, Ion Power), and a small amount of deionized water for a final Nafion loading of 33 wt %. The deionized water was added to the catalyst first and the Nafion was chilled before use to prevent possible catalyst burning. Glycerol was omitted in this procedure as it would have made the ink too thick to paint into the MES hole. Additionally, it would have made it very difficult to fully dry the ink due to the small surface area exposed to air once the ink is painted into the hole. The catalyst ink suspension was placed in an ultrasonication bath for 5 min and then mixed overnight on a magnetic stirrer to ensure uniform dispersion of the Nafion.

### **2.1.3 MES Hardware**

Specialized fuel cell hardware, shown in Figure 2.3b, was designed and fabricated specifically for conducting MES diagnostic experiments. The hardware resembles that for a traditional PEM fuel cell with serpentine channels milled into graphite plates for the anode and cathode flow fields. However, the cathode plate is embedded in an acrylic chassis, which additionally houses up to eight electrically isolated HRE flow fields for separately delivering air to the cathode and hydrogen to the HREs. Each HRE is sealed with an O-ring to prevent gas leakage. Thus, the only gas transport

pathway is through the long, thin Nafion sensing layers, which present a much higher transport resistance than the normal hydrogen and oxygen crossover through the membrane. Two tubulations (Scanivalve, Liberty Lake, WA) protrude from the back of each flow field to provide gas delivery. Rubber tubing connects the anode to each of the HREs so that hydrogen gas flows into the anode, then to each HRE in sequence. To prevent condensation of the humidified hydrogen gas as it passed in and out of the heated cell hardware, the entire setup was placed inside of an environmental chamber heated to the same temperature as the hydrogen gas. Finally, the cell's current and potential, and the HRE potentials are measured from a third tubulation that is attached to each flow field with conductive silver epoxy (EPO-TEK, Billerica, MA).

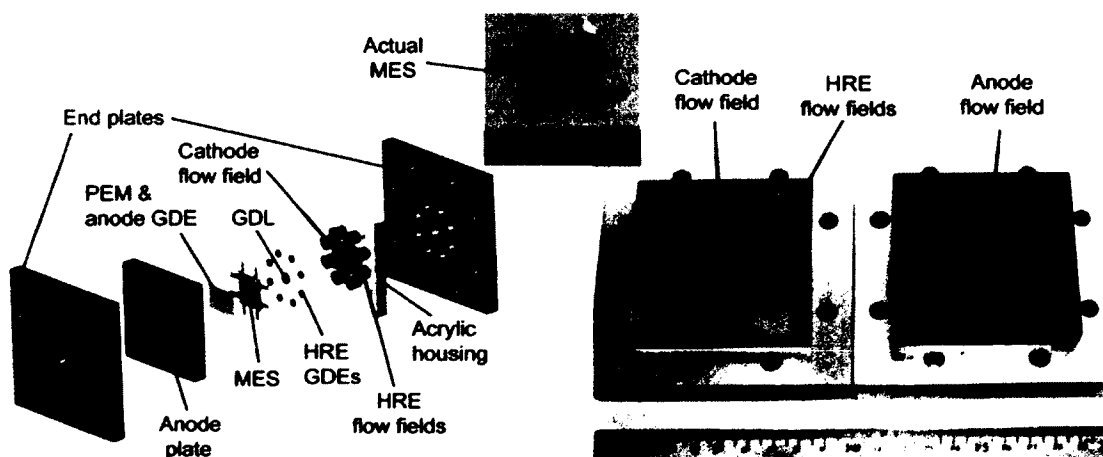


Figure 2.3 A schematic of the MES hardware (left) for use with the MES to make ionic potential measurements through the thickness of a PEM fuel cell cathode. Close ups of the cathode and anode plates (right), as well as a fully constructed MES (top).

### **2.1.4 Preparation of 1 cm<sup>2</sup> MEA**

A conventional 1 cm<sup>2</sup> membrane electrode assembly (MEA) was prepared for verifying that the MES cathode was representative of a normal electrode. The 1 cm<sup>2</sup> MEA was prepared from the same batch of catalyst ink and used the same Nafion impregnated GDE and the same GDL as the MES to eliminate variability between materials. The ink was hand painted onto a Nafion 115 membrane with a target loading of 0.7 mgPt/cm<sup>2</sup>, which was chosen to roughly match the 50 μm thickness of the MES cathode. A comparison of the performance of a 1 cm<sup>2</sup> MEA with the performance of an MES is discussed in the results section and verifies that the MES does not significantly interfere with the standard operation of the fuel cell.

### **2.1.5 Equipment and Testing Procedures**

A fuel cell test stand (850e, Scribner and Associates, Southern Pines, NC) was used to control the fuel cell temperature, and supply air to the cathode and H<sub>2</sub> to the anode with the desired dew point temperatures and flow rates. Air and H<sub>2</sub> flow rates of 0.2 and 0.3 slpm, respectively, were used and resulted in very high stoichiometric ratios given the small area of the MES cathode. The same constant flow rates were used for the 1 cm<sup>2</sup> MEA resulting in stoichiometric ratios of 12 and 29, at a current density of 1 A/cm<sup>2</sup>, for the air and H<sub>2</sub>, respectively. During ionic potential measurements, the HREs were held under the same temperature and humidity conditions as the anode at all times. A potentiostat (VSP, Biologic, Knoxville, TN) contacting the anode and cathode terminals controlled the fuel cell voltage, measured the current, and performed



electrochemical impedance spectroscopy (EIS). A data acquisition board (DAQ) (National Instruments, Austin, TX) simultaneously collected potential data versus the cathode from the HREs and the anode. All experiments used a Faraday cage (Technical Manufacturing Corporation, Peabody, MA) and shielded cables to minimize noise.

$N_2/H_2$  cyclic voltammetry (CV) measurements were performed with fully humidified gases at a cell temperature of 30 °C with a scan rate of 40 mV/s between potentials of 0 and 0.8 V. Electrochemically active surface area measurements were based on the CV's current-voltage curve area for hydrogen desorption, correcting for the electric double layer charging current. For potentiostatic polarization curves, potentials greater than 0.8 V were held for 60 s, while lower potentials were held for 10 min. The data presented are time-averages of the current and MES potential data for the last 30 and 90 s of the voltage holds for potentials  $>0.8$  V and  $\leq 0.8$  V, respectively. At the end of each potential hold, EIS was performed over a frequency range of 0.1 Hz to 300 kHz to obtain the high frequency resistances and generate IR-free polarization curves. Throughout the experiment, fully humidified hydrogen gas was delivered to HREs being held at the fuel cell temperature. Before performing experiments, we assured the continuity of the Nafion films by measuring the current when 0.5 V was applied between any two of the HREs. All HREs used here provided a current of 1  $\mu$ A or greater, with an average value of 5.2  $\mu$ A and a standard deviation of 1.7  $\mu$ A, which indicated that the sensing layers were in good contact with the electrode's Nafion phase.

## **2.2 MES Baseline Testing**

Before attempting to obtain distribution data using the MES, a few tests were conducted to assess the reliability of the RE readings as well as evaluate the effects of the MES structure on the performance of the fuel cell. The reliability testing was conducted using an alternative MES build, while the assessment of possible performance alterations due to the MES was carried out by comparing the performance of an MES cell with a cell using a standard MEA setup. The results find that the variations in the HREs used for making potential distribution measurements are insignificant considering the total potential drop across the catalyst layer and that the MES performs reasonably well compared to a standard PEM fuel cell.

### **2.2.1 Reliability Testing**

A series of tests run on the alternative MES structure provided confirmation that the MES was acting as expected and quantified the variability in the HREs. The alternative MES structure was built using the same technique discussed in the experimental section, however, in this case all five tabs protrude from the center sensing layer. Figure 2.3 shows a schematic of the MES used for reliability testing on the left and a schematic of the MES used for potential distribution data gathering on the right, for comparison. Using the alternative MES configuration each HRE is in contact with the same sensing layer and therefore the same slice of catalyst material. Consequently, if the MES is working properly, i.e. there is adequate conduction through the sensing layer and 1-D transport in the catalyst layer, then every HRE

should read the same potential value at any given time. Additionally, the potential value measured should be slightly higher than the fuel cell potential since the potential drop between the cathode and the middle sensing layer will be smaller than the potential drop between the cathode and the anode. This is due to the fact that reactions will continue to take place between the center sensing layer and the GDL meaning that more current is consumed and the potential drops as was discussed in the theory section of the introduction.

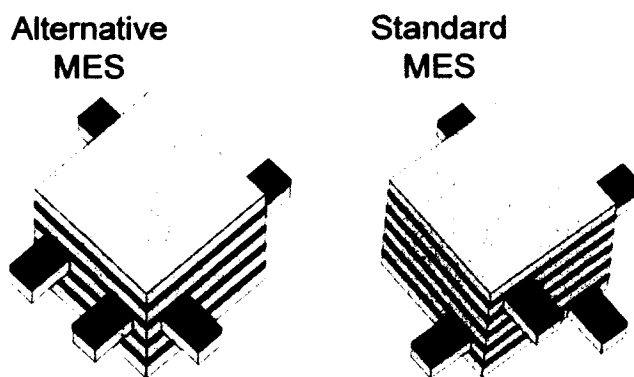


Figure 2.4 A schematic showing a comparison between the MES used for baseline testing (left) and the MES used for potential distribution data gathering (right). It can be seen that the MES on the left has all tabs protruding from a single sensing layer, while the MES on the right has each tab protruding from a different sensing layer. Note that the thickness in these schematics is exaggerated for clarity.

The alternative MES was first evaluated by using a hydrogen pumping test to assess the conduction between the HREs through the relevant Nafion sensing layer because adequate conductivity is necessary to obtain ionic potential measurements. The hydrogen pumping test was done by first purging the cathode compartment with inert

nitrogen in place of air, then applying a voltage between two HREs to induce a hydrogen oxidation reaction at the HRE used as the anode and a hydrogen evolution reaction at the HRE used as the cathode. The current between the HREs could then be measured and used to determine if there was sufficient conduction. Current of approximately  $1 \mu\text{A}$  or greater with an applied potential of  $0.5 \text{ V}$  indicated adequate conduction. In this case, four of the five HREs presented adequate conduction. The fifth HRE presented significantly lower conduction and was removed from the final analysis. We believe this outlier was due to damage of the exposed sensing layer tab that connects to the HRE during assembly.

We then assessed the variability of the HREs by conducting a series of five potentiostatic fuel cell polarization tests while measuring the potentials at the four HREs that had sufficient conduction. During this test, the HREs should provide equal potential readings at each fuel cell voltage, but will undoubtedly have small differences due to slight variations in the conductivity through the sensing layer, the behavior of the catalyst layer, etc. By analyzing the differences in these measurements, we will be able to obtain data that can be used for error analysis for future experiments. Additionally, it is important to prove that these variations are sufficiently small to show that the HREs are all accurate relative to each other, as this will build confidence for future distribution measurements. Figure 2.5 presents the results of our analysis of the HRE variability. The bar height in this figure represents the mean of the standard deviation of the potentials recorded at all four HREs during the five polarization curve experiments where each bar represents a specific voltage of the

polarization curve. The mean potential standard deviation was found by calculating the standard deviation between the four HREs at a given voltage for each realization individually then taking the average of the standard deviations over the five realizations. The error bars in Figure 2.5 are the standard deviation of the HRE potential standard deviations measured in each realization and indicate the variability between each realization. It can be seen from this figure that the variation between the HREs is generally less than 5 mV, which is significantly smaller than the expected potential drop through catalyst layers, 50 – 100 mV [45] at high currents, and should provide adequate potential resolution.

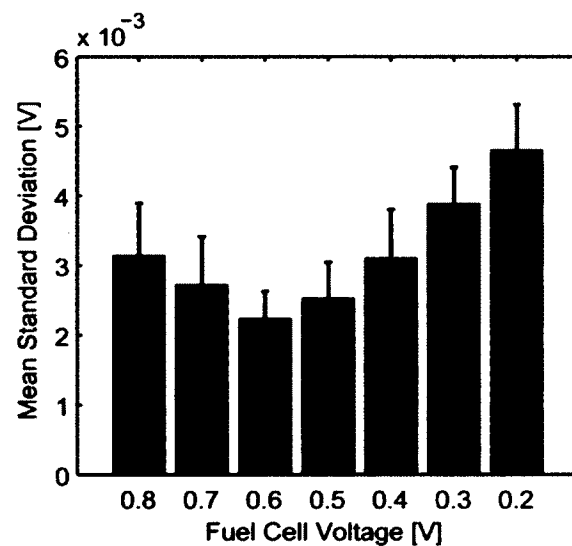


Figure 2.5 RE variability during a potentiostatic polarization curve with fuel cell voltages ranging between 0.8 and 0.2 V. The bars represent the mean potential standard deviation of the four REs for five realizations. The error bars are the standard deviation of the standard deviations. Deviations on the order of ~5 mV or less ensure adequate resolution for gathering through-plane data.

The results of the reliability tests showed that the REs generally varied by less than 5 mV, which is significantly smaller than the expected 50-100 mV drop through the electrode and should not, therefore, greatly affect our results.

## **2.2.2 Assessment of Effects of MES Assembly on Performance**

This section presents a comparison of the MES assembly with a more traditional PEM fuel cell assembly, a 1 cm<sup>2</sup> MEA, to verify that the cathode in the MES adequately replicates the characteristics of that in a conventional fuel cell. This assessment is important for demonstrating that the results measured by the MES are indicative of standard fuel cells during operation and are not specific to the MES arrangement. SEM images, electrochemical surface area (ECSA), CV scans and polarization curves were all conducted, analyzed and compared to assess any effects of the MES.

As discussed in the experimental section, the 1 cm<sup>2</sup> MEA was constructed using the same catalyst ink, GDL and GDE as the MES, and was painted such that the final thickness of the cathode catalyst layer would roughly match the thickness of the MES cathode catalyst layer. This was done to provide the closest comparison possible between the two assemblies. However, a post-mortem SEM image of the 1 cm<sup>2</sup> MEA showed that the cathode catalyst layer thickness was closer to 40 μm rather than the 50 μm of the MES. This reduced thickness was also evidenced by a reduced area in the hydrogen desorption portion of the 1 cm<sup>2</sup> MEA's CV plot (Figure 2.6 inset). Since this area is proportional to the ECSA, this also indicates a lower Pt loading in the

1 cm<sup>2</sup> MEA than in the MES. The mass specific ECSA values calculated from the MES and 1 cm<sup>2</sup> MEA CV curves in the inset of Figure 2.6 compare reasonably well when accounting for the ink composition, material densities, thicknesses, and an estimated porosity of 50%. We obtain ECSA values of 56 m<sup>2</sup><sub>Pt</sub>/g<sub>Pt</sub> for the MES cathode and 45 m<sup>2</sup><sub>Pt</sub>/g<sub>Pt</sub> for the 1 cm<sup>2</sup> MEA cathode. It is important to note that these values are within the expected range for this catalyst [46], as this provides something more than visual evidence suggesting that the MES hole was successfully filled with catalyst ink.

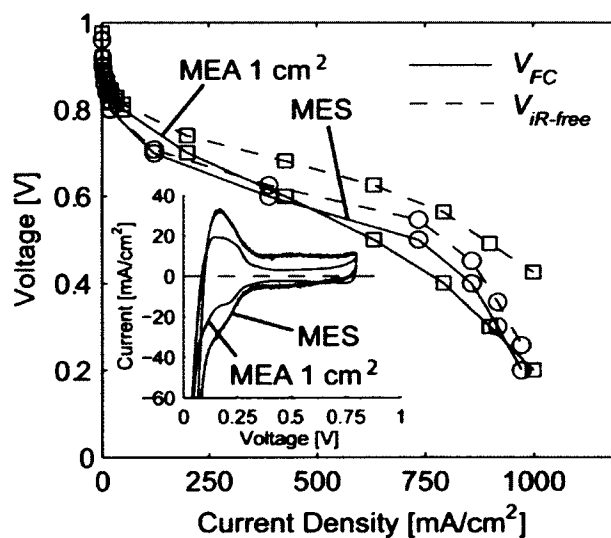


Figure 2.6 Comparison between the electrochemical characteristics of an MES and a 1 cm<sup>2</sup> MEA. The solid lines in the main plot are the polarization data collected at 57/57/35 °C (anode dew point/cell/cathode dew point); dashed lines show the IR-free curves. The inset shows cyclic voltammograms measured for the MES and the 1 cm<sup>2</sup> MEA with the vertical axis being the area-specific current density.

A closer look at the Figure 2.6 inset shows that the CVs have different profiles. It has been found that these differences often arise from high N<sub>2</sub> gas flow rates and the resulting increased removal of evolved hydrogen from the working electrode [20, 47]. This effect is consistent with extremely high N<sub>2</sub> flow rates used during the CV (0.2 slpm) relative to the very small size of the MES cathode. Additionally, roughly 7 times greater hydrogen crossover current density is observed in the MES cathode's CV compared to the 1 cm<sup>2</sup> MEA. This is identified by the positive shift of the EDL charging current as well as a lower OCV of 0.96 V for the MES compared to 0.98 V for the 1 cm<sup>2</sup> MEA. It is presumed that this is due to the large ratio of the anode to cathode area in the MES. This area asymmetry manifests itself as increased effective transport area through the membrane that reduces the resistances for water, hydrogen diffusion and proton conduction.

Figure 2.6 presents potentiostatic polarization curves for both the MES and the 1 cm<sup>2</sup> MEA at 57/57/35 °C (anode dew point/cell/cathode dew point). These curves show reasonable agreement over the entire voltage range, but have some notable differences. There is an apparent lack of activity in the MES at potentials around 0.8 V. In addition, there was a noticeable transient decrease in current with the MES during the first extended potential hold at 0.8 V, consistent with changes in the Pt oxide coverage conditions [48]. These differences at high potentials could be due to higher rates of hydrogen crossover or anode to cathode water diffusion. It is also possible that the isolated, microscale MES cathode exhibits oxide coverage effects more clearly than full-scale cathodes.



A comparison of the IR-free polarization curves shows that the Ohmic resistances are 4 times higher for the 1 cm<sup>2</sup> MEA than the MES, probably because of the MES electrode asymmetry. Examining the IR-free curves further, it can be seen that the MES and 1 cm<sup>2</sup> MEA have very similar IR-free potentials at roughly 750 mA/cm<sup>2</sup> and both begin to exhibit increasing mass transport limitations at currents above this value. The higher IR-free potential of the 1 cm<sup>2</sup> MEA at higher currents is most likely because of reduced flooding in the slightly thinner cathode. Indeed, the MES exhibited more severe flooding than the 1 cm<sup>2</sup> MEA when the air dew point was increased.

The preceding analysis comparing the MES to the 1 cm<sup>2</sup> MEA, leads to the conclusion that MES diagnostics fall in between the techniques of rotating disk electrode (RDE) and single cell MEA diagnostics. The MES allows for analysis of transport in an electrode under representative operating conditions, unlike RDE. However, because of the reduced membrane transport resistances arising from electrode area asymmetry, exact MEA conditions cannot be identically recreated. A possible way to minimize this discrepancy when applying MES diagnostics in the future is to match membrane transport resistances by using thicker membranes during MES diagnostics than those anticipated for use in the final PEM fuel cell.

## 2.3 MES Results

### 2.3.1 Transient Changes in Potential Distribution

Results from an experiment during which the fuel cell was held at a current of  $520 \text{ mA/cm}^2$  and temperature of  $57 \text{ }^\circ\text{C}$ , while the air dew point was changed from  $50$  to  $35 \text{ }^\circ\text{C}$  can be seen in Figure 2.7. During this experiment, the MES measured the electrolyte potential distribution across the cathode's thickness. Figure 2.7a presents the air dew point and fuel cell voltage time-series over roughly a 1 h portion of the experiment. At early times, the fuel cell exhibited a low, decreasing voltage due to electrode flooding. As the air's dew point cooled to  $35 \text{ }^\circ\text{C}$ , we observed a corresponding increase in voltage, indicating the evaporation of accumulated liquid water. After the dew point reached  $35 \text{ }^\circ\text{C}$ , we observed a small initial decrease in fuel cell voltage consistent with the initial drying of Nafion and increasing Ohmic losses.

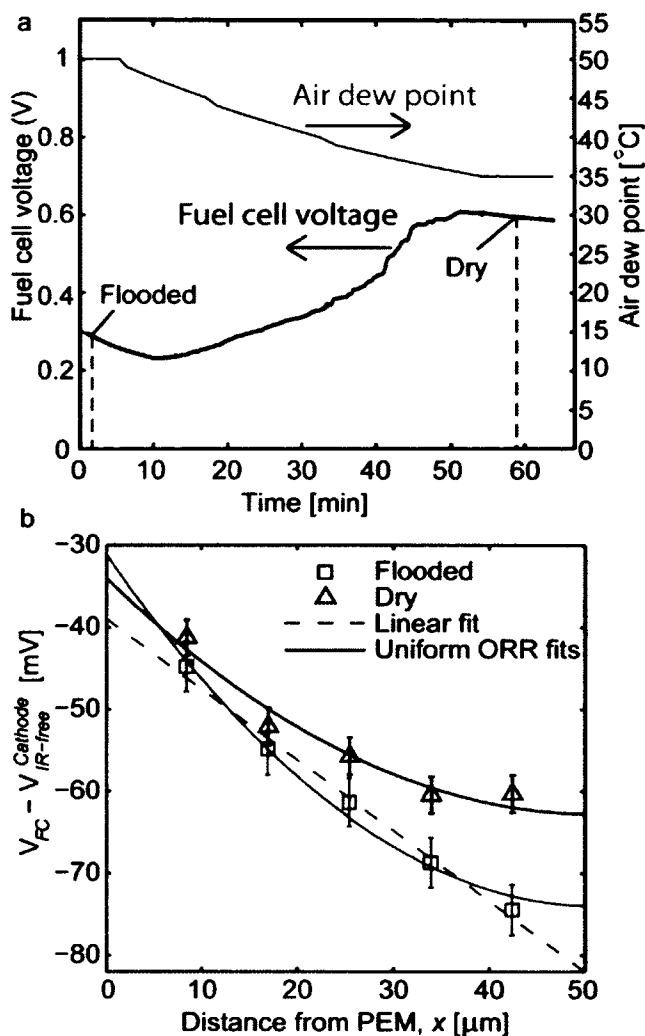


Figure 2.7 Effects of flooding and drying on the potential distribution through the electrode. a. Voltage and temperature time-series as the cathode dew point changed from 50 to 35 °C during a galvanostatic hold at 520 mA/cm<sup>2</sup>. b. Electrolyte potential distributions for both flooded (57/57/50 °C) and dry (57/57/35 °C) times indicated by the dashed lines in part a. Potential data for each case was averaged over 60 s. Error bars are a root mean square combination of the HRE standard deviation at OCV (2 mV) and the temporal variations of each HRE over the time-averaging period.

Figure 2.7b plots the through-plane electrolyte potential distributions across the cathode at the times indicated in Figure 2.7a. The points plotted were determined by

time-averaging data over 60 s periods. The error bars are the root mean square combination of the standard deviation of the HREs at OCV and the temporal variations of each HRE during the averaging period. This led to error bars in the range of 2–4 mV. First, it is observed in both cases that the potential gradient for the first two points and their extrapolated intercepts with the y-axis are nearly identical. Given the constant current density, this indicates negligible change in the proton conductivity in the membrane and in the portion of the electrode near the PEM. This is expected since the dry condition data was gathered at the beginning of the transient drying process so the cell was likely still well hydrated near the PEM. The key difference between the two profiles is the significant flattening of the dry profile near the GDL, whereas the flooded profile is roughly linear throughout as illustrated by the  $R^2$  value of 0.99 for the linear fit shown. Figure 2.7b also includes fits to the two profiles for a uniform, one-dimensional ORR distribution with a volumetric ORR rate of  $104 \text{ A/cm}^3$  consistent with the  $520 \text{ mA/cm}^2$  current density. These fits were calculated from the conservation of current equation that was previously discussed and presented in equation [1.4]. We applied a fixed potential boundary condition,  $\phi|_{x=0} = \phi_o$ , at the membrane interface and a zero current boundary condition,  $\partial\phi/\partial x|_{x=L} = 0$ , at the GDL to determine the analytical solution for a PEM fuel cell electrode. The final solution is shown in equation [2.1], where  $\phi_o$  is the potential at the interface of the electrode with the PEM. The linear profile of the flooded case indicates that the ORR is concentrated near the GDL interface due to mass transport limitations within the electrode. In other words, since the potential gradient is uniform up to the last measurement point, the current is also uniform. This means the proton current is primarily being consumed

between the last sensing layer and the GDL. In contrast, the notable flattening of the dry distribution near the GDL suggests that the electrode is relatively more proton transport limited due to Ohmic losses and the reaction has shifted toward the PEM interface.

$$\phi = \frac{i}{\sigma_{eff}} \left( \frac{x^2}{2L} - x \right) + \phi_o \quad [2.1]$$

The MES data also provides a method for estimating the electrode's ionic conductivity, which is based on using local values rather than global values like most existing electrode characterization methods use. This estimation can be made using Ohm's law in the form shown in equation [2.2] where  $V$  is determined using the potential drop between the first two data points in Figure 2.7b,  $\sim 10$  mV,  $i$  is the known current density at which the fuel cell is being held,  $520$  mA/cm<sup>2</sup>, and  $L$  is the known distance between the two sensing layers at which the potentials are being measured,  $8.5$   $\mu$ m. These calculations lead to an effective conductivity of  $4.5$  S/m, which is significantly higher than the expected value of less than  $1$  S/m and suggests that there may be an unknown reaction process or an unexpected material property shift under certain conditions that the MES is detecting. This is an interesting finding that would likely go unnoticed when using most existing electrode characterization techniques. Possible explanations for this result will be discussed in further detail in the next section.

$$\sigma_{eff} = \frac{iL}{V} \quad [2.2]$$

### 2.3.2 Polarization Curve Analysis

Polarization curve experiments were performed to elucidate the effects of fuel cell potential and current density on the electrolyte potential distributions under high and low humidity conditions. The potentiostatic polarization curves were measured from OCV to 0.2 V at a cell temperature of 57 °C with fully humidified hydrogen. The air dew point temperatures for the high and low humidity conditions were 50 and 35 °C, respectively. The corresponding polarization curves in Figure 2.8a show greater mass transport losses and lower limiting current densities in the high humidity condition due to liquid water flooding. However, the Ohmic losses did not seem to vary significantly between the two cases because the fully humidified hydrogen and small MES area act to maintain membrane hydration in both cases.

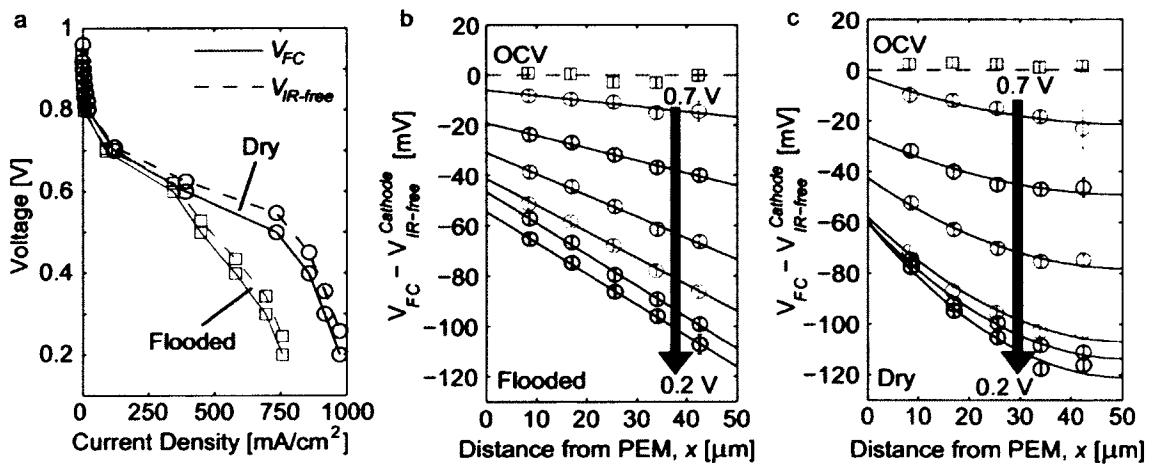


Figure 2.8 Polarization curves and electrolyte potential distributions through the thickness of the electrode as measured by the MES. a, Polarization and IR-free curves for both flooded (57/57/50°C) and dry (57/57/35°C) conditions. b, Electrolyte potential distributions through the thickness of the MES in flooded conditions during potentiostatic holds; starting with OCV (squares) then 0.7 V to 0.2 V (circles). The solid lines are linear fits at each fuel cell potential. c, Electrolyte potential distributions through the thickness of the MES in dry conditions during potentiostatic holds; starting with OCV (squares) then 0.7 V to 0.2 V (circles). Solid lines show the analytical solution for a uniform reaction rate at each fuel cell potential.

Figure 2.8b,c shows how the electrolyte potential distributions change through the thickness of the electrode under two different humidity conditions and for fuel cell potentials ranging from 0.7 to 0.2 V in 0.1 V increments. This is novel data that has not been seen before the development of the MES. In Figure 2.8b, we have plotted linear fits to the high humidity condition as this has proven to be the better fit for a flooded electrode. The linear trend at the highest potentials for the flooded conditions suggests that the cell is mass transport limited even at low currents. This is another somewhat unexpected finding that likely would have gone unnoticed in traditional characterization experiments. Flooding at low currents is possibly due to the high anode humidity and the MES electrode asymmetry that increases the relative water diffusion rates from anode to cathode. Our analysis shows that as the current increases, the linear fit improves from an  $R^2$  value of 0.898 to 0.999. This is expected: more water is produced at higher currents, impeding oxygen transport and driving the reaction toward the GDL even further.

The dry case, shown in Figure 2.8c, appears to match the analytical solution for uniform ORR well at most currents. This implies that even at high currents, the cell does not become as severely mass transport limited. In fact, the flattening out of the two data points farthest from the membrane indicates that the cell is somewhat proton transport limited and that more of the reaction is occurring closer to the PEM. However, at the highest currents it is apparent that the profile becomes more linear toward the PEM side, which is consistent with the fuel cell being in the mass transport limited portion of the polarization curve.

We now analyze the fits to the distributions to extract information regarding the effective ionic conductivity and the through-plane uniformity of the ORR. Table 2.1 lists the fit values for  $\phi_o$  and  $\sigma_{eff}$ , along with the Ohmic potential drop,  $\eta_{ohm}$ , measured by EIS for the dry condition data in Figure 2.8c. The values for the 0.7 V hold are not shown because of the large, unsystematic variability associated with the point nearest the GDL that was likely due to a water droplet entering the HRE during the time-averaging. We note that there is generally less than a 10% difference between the  $\phi_o$  and  $\eta_{ohm}$  values, indicating that the value of the high frequency resistance is primarily due to the PEM's resistance. This good agreement for the PEM's potential drop, and the high  $R^2$  values suggest that the fits to the data are both reasonably precise and accurate. We conclude that the conductivity values calculated from the fits and listed in Table 2.1 are representative estimations, typically ranging between 4.0 and 4.5 S/m.



Table 2.1 Fitting parameters for potential distribution under dry conditions shown in Figure 6c, including the measured Ohmic overpotential,  $\eta_{ohm}$ .

$V_{FC}$ [V]	$\eta_{ohm}$ [mV]	$\phi_o$ [mV]	$\sigma$ [S/m]	$R^2$	% Err $ \eta_{ohm} + \phi_o  / \eta_{ohm}$
0.6	25.1	-26.4	4.40	0.923	5.18
0.5	46.2	-42.4	5.44	0.974	8.23
0.4	51.1	-57.9	4.45	0.980	13.3
0.3	56.3	-59.9	4.34	0.987	6.39
0.2	57.9	-60.0	4.05	0.979	3.63

The conductivity values from the fits as well as those estimated from the initial slopes in Figure 2.7b, agree well with the recent measurements taken by Liu et al. [49] for the same ionomer/carbon (Vulcan XC-72R) weight ratio of 0.6 and oversaturated gases. Using EIS analysis on an  $N_2/H_2$  cell, they found the resistivity to be  $\sim 25 \Omega \text{ cm}$  in their work, which translates to  $\sim 4 \text{ S/m}$ . Although our measurements of  $\sim 4.5 \text{ S/m}$  ( $\sim 22 \Omega \text{ cm}$ ) agree well with Liu et al.'s results, we find that these conductivities are higher than our anticipated value of less than  $1 \text{ S/m}$ . We estimated this value using the bulk conductivity of Nafion equilibrated with liquid water at  $330 \text{ K}$  ( $13 \text{ S/m}$ ) [50], a realistic tortuosity of roughly 3, and an expected Nafion volume fraction of 0.2, where the Nafion volume fraction is estimated based on the Nafion loading, density of Nafion, and the electrode thickness [49]. These high conductivities led Liu et al. to estimate nonphysical tortuosity factor values as low as 0.5 when considering their estimates of Nafion volume fraction and their measured values for the conductivity of

cast Nafion films. Because tortuosity values below unity are not physical, this suggests an unknown mechanism causing abnormally high conductivity in the electrode.

We suggest three possible causes for the high conductivity given *ex situ* studies have shown that thin Nafion films exhibit lower conductivity than bulk [51]. (1) Water generation within the agglomerates results in non-equilibrium water content levels (above an  $\text{H}_2\text{O}/\text{SO}_3^-$  ratio of 22 for liquid water equilibrated Nafion [50]) due to water desorption resistances and increases the conductivity within the electrode. (2) Water films surrounding the Nafion provide proton transport bridges that reduce tortuosity and increase local mobility. Because of the porosity and pore morphology of Nafion, protons have roughly 5 times higher mobility in water [50, 52]. (3) Surface conduction mechanisms and acidic groups on the carbon catalyst support may increase the electrode's conductivity. Additional research is required to elucidate the proton conduction mechanisms in PEM fuel cell electrodes and determine the cause of such high conductivity values. The MES is one of the few methods that has been able to locally measure ionic conductivity to find this unexpected result and is the only method for making *in situ*, through-thickness potential distribution methods in the cathode catalyst layer of a PEM fuel cell. We hope the findings obtained with the MES will promote further research into distributions through the catalyst layer and will continue to aid researchers to fully characterize the reactions taking place in PEM fuel cells during operation.

## 2.4 Summary

In this chapter we studied the electrolyte potential distributions that arise through the thickness of the cathode catalyst layer of a PEM fuel cell under normal operating conditions. These measurements were made possible through the development of the MES, which used Nafion sensing layers positioned at known distances through the thickness of the electrode to make ionic potential measurements during standard fuel cell operation. We found that the potential distribution data could provide us with insight into whether the cell was dry or flooded and additionally allowed us to determine the effective ionic conductivity through the cathode catalyst layer. The conductivity measurement was particularly interesting because it was multiple times higher than expected based on the catalyst layer geometry. This suggests the presence of some unknown mechanism creating higher than expected ionic conductivity through the catalyst layer. Although we have many speculations about what this mechanism might be, more work needs to be done to know for sure.

While the MES provided us with some interesting, previously unattainable data, we suggest a number of improvements to increase the reliability and repeatability of the MES data. First and foremost, the MES hardware must be improved. The first iteration of hardware achieved its goals, allowing us to flow hydrogen over the HREs and obtain a measurement from each sensing layer. However, the setup was cumbersome and unheated gas lines lead to instabilities in the cell due to the formation of water droplets. The use of an environmental chamber dramatically improved this issue, but it complicated the setup and still did not provide the level of control desired for testing.

In the future, redesigning the hardware such that all of the gasses traveled inside the insulated and heated hardware would alleviate the droplet issues and allow for more precise control over the relative humidity of the gas flowing over each HRE. Additionally, creating easier access to the HRE measurement points through the use of a printed circuit board, for example, would make the hardware more durable and easier to use. These changes are currently being implemented by another Ph. D. student in our lab.

Another change would be to make the MES thinner so that it's closer to the thickness of state-of-the-art catalyst layers or to make the insulating layers thinner so the measurement resolution could be increased. Thinner insulating layers are too difficult to work with using our current fabrication techniques however. Furthermore, a thinner MES would require a smaller diameter hole to ensure that there was still 1-D transport through the catalyst layer. Again, our current fabrication techniques would not allow us to properly make or fill such a small hole, but we believe there are ways to overcome both of these issues. Regardless of these improvements, the MES has proven to be a useful diagnostic tool that has the potential to be extremely helpful to researchers developing new catalyst layers for improved performance of PEM fuel cells.

## **Chapter 3**

# **A Mathematical Method for Determining Local Current, Charging Current and Charge Stored from Potential Distributions**

This chapter will discuss the mathematical methods we have developed for analyzing the electric and ionic potential distributions obtained using an ES to study an EDL capacitor. Results and analysis of the electric and ionic ES data will be discussed in the following two chapters, but first we will introduce the theory behind the analysis. There are some important differences in the data these two devices were able to collect, which affected how the data was analyzed, but the methods used were very similar and will therefore be discussed in tandem as much as possible.

### 3.1 Finite Difference Methods Derivations

Much like the MES discussed in the previous chapter, both the electric and ionic ES make potential measurements at discrete, known locations through the thickness of an electrode, in this case the negative electrode, during standard cell operation. Using this data along with Ohm's Law, we were additionally able to extract local current and local charging current distributions.

Ohm's Law is traditionally written as,  $V = IR$ , where  $V$  is the voltage,  $I$  is the current and  $R$  is the resistance. We can rewrite this equation by noting that voltage is define as the difference in electrical potential between two points,  $V = \phi_1 - \phi_2 = \Delta\phi$ . Additionally, we know that resistance is related to conductivity as shown in equation [3.1].

$$R = \frac{L}{A\sigma} \quad [3.1]$$

Where  $L$  is the length over which the resistance is being measured, in this case the distance between sensing layers,  $\Delta x$ ,  $A$  is the surface area of the electrode and  $\sigma$  is the conductivity between the two sensing layers. We can now rewrite Ohm's Law as:

$$\frac{I}{A} = i = \sigma \frac{\Delta\phi}{\Delta x} \quad [3.2]$$

where  $i$  is the area-specific current density. The final differential form of this equation is:

$$i = -\sigma \frac{d\phi}{dx} \quad [3.3]$$

Equation [3.3] includes a negative sign because current is flowing in the positive  $x$  direction, while  $d\phi/dx$  is negative in this direction since current is being consumed. This equation shows us that we can calculate the current as long as we know the relevant conductivity and the slope of the current, both of which can be obtained using data from the ES. We can obtain  $d\phi/dx$  from the sensing layer data since we know the potential at and the distance between each sensing layer. With the ionic ES we were only able to obtain an effective conductivity from EIS studies, however, with the electrical ES we were able to use the ES to measure local conductivity values. By applying finite difference methods to our discretized potential and conductivity data, we can calculate the local current with reasonable accuracy. Additionally, once we have obtained local current values, we can again use finite differencing to determine the local charging current since the charging current,  $i_c$ , is equal to the first derivative of the current with respect to  $x$ .

Before we consider the finite difference equations used to solve for  $i$ , it is important to note that the electric ES not only allowed us to gather electric potential measurements during operation, but also made it possible for us to make resistance measurements

between the sensing layers prior to operation. Using these resistance measurements and the known geometry of the electrode, we were able to calculate the conductivity through the electrode. However, because the resistance measurements were made between two sensing layers, the resulting conductivity values calculated are an average conductivity of the slice of the electrode between the sensing layers and should therefore be taken to represent the conductivity at the center of that slice. This means that the resistance and conductivity measurements were made at different locations in the electrode, which slightly complicates the finite difference equations. Figure 3.1 shows a schematic of the staggered grid arrangement for the finite differencing for 7 sensing layers and 6 conductivity measurements.

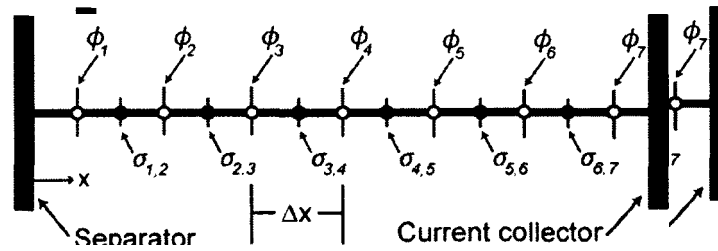


Figure 3.1 Positions at which conductivity,  $\sigma$ , and potential,  $\phi$ , measurements were taken.

Let us now consider the derivative term in equation [3.3]. In order to have a second order accurate solution, we apply a standard three point forward and backward difference at the end points and a central difference on the interior points as seen below.

$$i_{m,fd} = -\sigma_m \left[ -3\phi_m + 4\phi_{m+1} - \phi_{m+2} \right] / 2\Delta x \quad [3.4]$$



$$i_{m_{bkwd}} = -\sigma_m [\phi_{m-2} - 4\phi_{m-1} + 3\phi_m] / 2\Delta x \quad [3.5]$$

$$i_m = -\sigma_m (\phi_{m+1} - \phi_{m-1}) / 2\Delta x \quad [3.6]$$

Equations [3.4]-[3.6] are second order accurate if the conductivity values are constant or known at the position of the sensing layers. Since we were only able to obtain a bulk conductivity value for the ionic ES data, these equations can be used to calculate the current for that case. For the electric ES, we were able to measure local conductivity, however, because these measurements were made between sensing layers we must apply finite difference methods again in order to obtain conductivity values at the sensing layers. To find the forward and backward finite difference equations for conductivity we started by using the Taylor Series expansion on two adjacent points. For the forward difference we see:

$$\begin{aligned} \sigma_{m,m+1} &= \sigma_m + \sigma'_m \left( \frac{\Delta x}{2} \right) + \frac{\sigma''_m \left( \frac{\Delta x}{2} \right)^2}{2!} + \dots \\ \sigma_{m+1,m+2} &= \sigma_m + \sigma'_m \left( \frac{3\Delta x}{2} \right) + \frac{\sigma''_m \left( \frac{3\Delta x}{2} \right)^2}{2!} + \dots \end{aligned} \quad [3.7]$$

We can combine these two equations to eliminate the first derivative by multiplying the first equation by 3 and then subtracting the second equation from the first. We are left with the second order equation shown below, which estimates the conductivity at a

sensing layer based on the conductivity measurements made at  $+\Delta x/2$  and  $+3\Delta x/2$  away from that sensing layer.

$$3\sigma_{m,m+1} - \sigma_{m+1,m+2} = (3\sigma_m - \sigma_m) + \left[ 3\sigma'_m \left( \frac{\Delta x}{2} \right) - \sigma'_m \left( \frac{3\Delta x}{2} \right) \right] + O(\Delta x^2) \quad [3.8]$$

$$\sigma_m = \frac{(3\sigma_{m,m+1} - \sigma_{m+1,m+2})}{2} + O(\Delta x^2) \quad [3.9]$$

The backward difference is derived in a similar way with the final form shown in Eq. [3.10].

$$\sigma_m = \frac{(3\sigma_{m-1,m} - \sigma_{m-2,m-1})}{2} + O(\Delta x^2) \quad [3.10]$$

By combining equations [3.9] and [3.10] with [3.4] and [3.5] respectively, we obtain the final form of the current equations.

$$i_{m\_fwd} = \frac{-(3\sigma_{m,m+1} - \sigma_{m+1,m+2})}{2} [-3\phi_m + 4\phi_{m+1} - \phi_{m+2}] / 2\Delta x + O(\Delta x^2) \quad [3.11]$$

$$i_{m\_bkwd} = \frac{-(3\sigma_{m-1,m} - \sigma_{m-2,m-1})}{2} [\phi_{m-2} - 4\phi_{m-1} + 3\phi_m] / 2\Delta x + O(\Delta x^2) \quad [3.12]$$

Finally, we use a modified central difference formula for the interior points in order to take into account the changing conductivities. Here we can break down the central

difference formula seen in equation [3.6] into a forward and backward difference. This allows us to include the conductivity values from both sections of the electrode and we obtain the final central difference equation for calculating current:

$$i_m = -\left[\sigma_{m,m+1}(\phi_{m+1} - \phi_m) + \sigma_{m-1,m}(\phi_m - \phi_{m-1})\right]/2\Delta x + O(\Delta x^2) \quad [3.13]$$

Equations [3.11]-[3.13] can then be used to find the current distribution through the electrode. Furthermore, the values obtained from this calculation can be used in the second derivative calculation for determining the volumetric charging current distribution. An extensive derivation of the finite difference equations for finding the volumetric current density is not included as they are found from standard finite difference equations. However, the forward, backward and central difference equations are shown in equations [3.14]-[3.16] to facilitate discussion of the error calculations in the next section:

$$i_{c,m_{fwd}} = \frac{d}{dx} \left( -\sigma \frac{d\phi}{dx} \right) \Big|_{m_{fwd}} = \frac{di}{dx} \Big|_{m_{fwd}} = (-3i_m + 4i_{m+1} - i_{m+2}) / 2\Delta x + O(\Delta x^2) \quad [3.14]$$

$$i_{c,m_{bkwd}} = \frac{d}{dx} \left( -\sigma \frac{d\phi}{dx} \right) \Big|_{m_{bkwd}} = \frac{di}{dx} \Big|_{m_{bkwd}} = (i_{m-2} - 4i_{m-1} + 3i_m) / 2\Delta x + O(\Delta x^2) \quad [3.15]$$

$$i_{c,m} = \frac{d}{dx} \left( -\sigma \frac{d\phi}{dx} \right) \Big|_m = \frac{di}{dx} \Big|_m = (i_{m+1} - i_{m-1}) / 2\Delta x + O(\Delta x^2) \quad [3.16]$$

## 3.2 Charge Storage

Both the electric and ionic ES provide us with enough information to additionally determine the volumetric charge storage distribution through the electrode at any given point during the charging/discharging cycle. The amount of charge stored in the electrode is directly related to the amount of current applied over a stretch of time. Therefore, if we time-integrate the local charging current at each sensing layer, which was determined using equations [3.14]-[3.16], we will find the total charge stored in each slice of the electrode at a given point in the charging cycle. Likewise, if we are discharging the cell, we will be able to determine how much charge has been discharged from each section of the electrode at a given time during the discharge cycle. The time-integral for finding the charge storage,  $Q$ , is shown in equation [3.17].

$$Q[C/cm^3] = \int_{t_1}^{t_2} i_c dt \quad [3.17]$$

This method appears to give us reasonable results, which are shown in the following two chapters, however the error can become a problem and sometimes prohibits us from looking as far into the charging/discharging cycle as we would like to. This is because the error associated with the charge storage,  $E_Q$ , must also be determined through time-integration as seen below. It is likely that this method of calculating error is resulting in rather conservative error bars and that the data may be better than the error suggests. This would especially be true if there were a systematic offset in the measurements as this would affect the absolute value of the sensing layer

measurements, but not the differential between them, which is ultimately what our results are based on. Our interpretation of the charge storage distribution data and the associated error are discussed more thoroughly in the following chapters.

$$E_Q = \int_{t_1}^{t_2} E_{i_c} dt \quad [3.18]$$

### 3.3 Error Calculations

#### 3.3.1 Error Propagation Equations as Applied to ES Data

We applied error propagation theory to assess the error in our results based on errors in our measurements and the finite difference equations used to determine local current and charging current. Note that truncation error from applying finite difference methods was assumed to be small compared to the measurement error. The generalized forms of the error equations are shown in equations [3.19] and [3.20] for the current and volumetric charging current respectively.

$$E_i = \sqrt{\left(E_\sigma \frac{di}{d\sigma}\right)^2 + \left(E_\phi \frac{di}{d\phi}\right)^2 + \left(E_{\Delta x} \frac{di}{d\Delta x}\right)^2} \quad [3.19]$$

$$E_{i_c} = \sqrt{\left(E_{\Delta x} \frac{di_c}{d\Delta x}\right)^2 + \left(E_i \frac{di_c}{di}\right)^2} \quad [3.20]$$

Each derivative in equations [3.19] and [3.20] must then be determined from the previously defined current and volumetric charging current equations. For example, to find the error associated with the forward difference current calculation we must consider equation [3.11] and find the following derivatives:

$$\frac{di}{d\sigma_{m,m+1}} = \frac{-3}{2} \frac{[-3\phi_m + 4\phi_{m+1} - \phi_{m+2}]}{(2\Delta x)}, \quad \frac{di}{d\sigma_{m+1,m+2}} = \frac{1}{2} \frac{[-3\phi_m + 4\phi_{m+1} - \phi_{m+2}]}{(2\Delta x)}$$

$$\frac{di}{d\phi_m} = \frac{-(3\sigma_{m,m+1} - \sigma_{m+1,m+2})}{2} \left[ \frac{-3}{2\Delta x} \right], \quad \frac{di}{d\phi_{m+1}} = \frac{-(3\sigma_{m,m+1} - \sigma_{m+1,m+2})}{2} \left[ \frac{2}{\Delta x} \right] \quad [3.21]$$

$$\frac{di}{d\phi_{m+2}} = \frac{-(3\sigma_{m,m+1} - \sigma_{m+1,m+2})}{2} \left[ \frac{-1}{2\Delta x} \right]$$

$$\frac{di}{d\Delta x} = \frac{(3\sigma_{m,m+1} - \sigma_{m+1,m+2})}{2} \left[ -3\phi_m + 4\phi_{m+1} - \phi_{m+2} \right] / (2\Delta x)^2$$

The derivatives shown in [3.21] can then be inserted into [3.19] and the final form becomes,

$$E_{i_{m,fd}} = \sqrt{\left[ E_{\sigma_{m,m+1}} \frac{-3/2(-3\phi_m + 4\phi_{m+1} - \phi_{m+2})}{2\Delta x} \right]^2 + \left[ E_{\sigma_{m+1,m+2}} \frac{1/2(-3\phi_m + 4\phi_{m+1} - \phi_{m+2})}{2\Delta x} \right]^2 + \left[ E_{\phi_m} \frac{3/2(3\sigma_{m,m+1} - \sigma_{m+1,m+2})}{2\Delta x} \right]^2 + \left[ E_{\phi_{m+1}} \frac{-1/2(3\sigma_{m,m+1} - \sigma_{m+1,m+2})}{2\Delta x} \right]^2 + \left[ E_{\phi_{m+2}} \frac{1/2(3\sigma_{m,m+1} - \sigma_{m+1,m+2})}{2\Delta x} \right]^2 + \left[ E_{\Delta x} \frac{(3\sigma_{m,m+1} - \sigma_{m+1,m+2})(-3\phi_m + 4\phi_{m+1} - \phi_{m+2})}{2 \cdot 2\Delta x^2} \right]^2} \quad [3.22]$$

This process is repeated again for the backward and central difference current calculations to obtain,

$$E_{i_{m,bwd}} = \sqrt{\left[ E_{\sigma_{m-1,m}} \frac{-3/2(\phi_{m-2} - 4\phi_{m-1} + 3\phi_m)}{2\Delta x} \right]^2 + \left[ E_{\sigma_{m-2,m-1}} \frac{1/2(\phi_{m-2} - 4\phi_{m-1} + 3\phi_m)}{2\Delta x} \right]^2 + \left[ E_{\phi_m} \frac{-3/2(3\sigma_{m-1,m} - \sigma_{m-2,m-1})}{2\Delta x} \right]^2 + \left[ E_{\phi_{m-1}} \frac{(3\sigma_{m-1,m} - \sigma_{m-2,m-1})}{\Delta x} \right]^2 + \left[ E_{\phi_{m-2}} \frac{-1/2(3\sigma_{m-1,m} - \sigma_{m-2,m-1})}{2\Delta x} \right]^2 + \left[ E_{\Delta x} \frac{(3\sigma_{m-1,m} - \sigma_{m-2,m-1})(\phi_{m-2} - 4\phi_{m-1} + 3\phi_m)}{2 \cdot 2\Delta x^2} \right]^2} \quad [3.23]$$

$$E_{i_m} = \sqrt{\left[ E_{\sigma_{m,m+1}} \frac{(-\phi_{m+1} + \phi_m)}{2\Delta x} \right]^2 + \left[ E_{\sigma_{m-1,m}} \frac{(\phi_m - \phi_{m-1})}{2\Delta x} \right]^2 + \left[ E_{\phi_{m+1}} \frac{(-\sigma_{m,m+1})}{2\Delta x} \right]^2 + \left[ E_{\phi_m} \frac{(\sigma_{m,m+1} + \sigma_{m-1,m})}{2\Delta x} \right]^2 + \left[ E_{\phi_{m-1}} \frac{(-\sigma_{m-1,m})}{2\Delta x} \right]^2 + \left[ E_{\Delta x} \frac{\sigma_{m,m+1}(\phi_{m+1} - \phi_m) - \sigma_{m-1,m}(\phi_m - \phi_{m-1})}{2\Delta x^2} \right]^2} \quad [3.24]$$

A similar process is conducted to find the error for the volumetric charging current equations. Here we have assumed that equations [3.22]-[3.24] have already been solved for, as the solution for  $E_i$  is needed to compute  $E_{i_c}$ . The final form of the equations for calculating the error on the forward, backward and central difference volumetric charging current equations are shown below.

$$E_{i_{c,m} \text{ fwd}} = \sqrt{\left[ E_{i_m} \left( \frac{-3}{2\Delta x} \right) \right]^2 + \left[ E_{i_{m+1}} \left( \frac{2}{\Delta x} \right) \right]^2 + \left[ E_{i_{m+2}} \left( \frac{-1}{2\Delta x} \right) \right]^2 + \left[ E_{\Delta x} \frac{(3i_m - 4i_{m+1} + i_{m+2})}{2\Delta x^2} \right]^2} \quad [3.25]$$

$$E_{i_{c,m} \text{ bkwd}} = \sqrt{\left[ E_{i_m} \left( \frac{3}{2\Delta x} \right) \right]^2 + \left[ E_{i_{m-1}} \left( \frac{-2}{\Delta x} \right) \right]^2 + \left[ E_{i_{m-2}} \left( \frac{1}{2\Delta x} \right) \right]^2 + \left[ E_{\Delta x} \frac{(-i_{m-2} + 4i_{m-1} - 3i_m)}{2\Delta x^2} \right]^2} \quad [3.26]$$

$$E_{i_{c,m}} = \sqrt{\left[ E_{i_{m+1}} \left( \frac{1}{2\Delta x} \right) \right]^2 + \left[ E_{i_{m-1}} \left( \frac{-1}{2\Delta x} \right) \right]^2 + \left[ E_{\Delta x} \frac{(i_{m-1} - i_{m+1})}{2\Delta x^2} \right]^2} \quad [3.27]$$

The results of equations [3.22]-[3.27] are used to plot error bars for the current density and volumetric charging current distribution plots that will be shown in the following two chapters.

### 3.3.2 Error Analysis of Analytical Equation

It is also of interest to consider error propagation applied to the analytical solution for the conservation of current equation as the result provides a simple expression that clearly illustrates how each term affects the uncertainty error. We will start with the analytical equation for the ionic potential, which was presented in equation [2.1] and is rewritten here for simplicity:



$$\phi = \frac{i}{\sigma_{eff}} \left( \frac{x^2}{2L} - x \right) + \phi_o \quad [3.28]$$

We then use this equation to determine the partial derivatives from the error propagation equation found in [3.19] and subsequently substitute them into this equation.

$$E_i = \sqrt{\left[ E_\sigma \frac{-i_{cell} \left( \frac{x_{m+1}^2 - x_{m-1}^2}{2L} + x_{m-1} - x_{m+1} \right)}{2\Delta x} \right]^2 + \left[ E_{\phi_{m+1}} \frac{-\sigma_{eff}}{2\Delta x} \right]^2 + \left[ E_{\phi_{m-1}} \frac{\sigma_{eff}}{2\Delta x} \right]^2} + \left[ E_{\Delta x} \frac{i_{cell} \left( \frac{x_{m+1}^2 - x_{m-1}^2}{2L} + x_{m-1} - x_{m+1} \right)}{2\Delta x^2} \right]^2 \quad [3.29]$$

This equation can be simplified by recognizing that  $x_{m-1} - x_{m+1} = -2\Delta x$  and  $x_{m+1}^2 - x_{m-1}^2 = (x_{m+1} - x_{m-1})(x_{m+1} + x_{m-1}) = 2\Delta x(2x_m)$ . The result of this simplification is shown below.

$$E_i = \sqrt{\left[ E_\sigma \frac{-i_{cell} \left( \frac{x_m}{L} - 1 \right)}{\sigma_{eff}} \right]^2 + 2 \left[ E_\phi \frac{\sigma_{eff}}{2\Delta x} \right]^2 + \left[ E_{\Delta x} \frac{i_{cell} \left( \frac{x_m}{L} - 1 \right)}{2\Delta x} \right]^2} \quad [3.30]$$

To better understand the effects of each error term at a given point, we normalize equation [3.30] by the current at point  $m$ . The current at a point  $m$  is defined by Ohm's law as shown in equation [3.3] where the first derivative of the potential can be exactly calculated from the uniform analytical solution for potential given in equation [3.28]. The current we are normalizing by is therefore given by the equation below.

$$i_{x_m} = -\sigma_{eff} \left( \frac{i_{cell}}{\sigma_{eff}} \left[ \frac{x_m}{L} - 1 \right] \right) = i_{cell} \left[ 1 - \frac{x_m}{L} \right] \quad [3.31]$$

Equation [3.32] shows the result of normalizing the error by this current.

$$\varepsilon_{x_m} = \frac{E_{i_{x_m}}}{i_{x_m}} \sqrt{\left[ \frac{E_\sigma}{\sigma_{eff}} \right]^2 + 2 \left[ E_\phi \frac{\sigma_{eff}}{2\Delta x i_{cell}} \left[ 1 - \frac{x}{L} \right] \right]^2 + \left[ E_{\Delta x} \frac{-1}{2\Delta x} \right]^2} \quad [3.32]$$

This is an interesting and surprisingly simple result. We notice that the first and third terms on the right side of the equation are just the relative errors of the conductivity and spacing, respectively. Changing one of these errors would have a proportional effect on the current error that is independent of the location within the electrode. In other words, if the error at each sensing layer were plotted versus the distance away from the separator and one of these two errors was changed, the shape of the curve would remain the same, but it would shift up or down depending on which way the error changed. However, the middle term, which is the percent error in the current

calculation due to the error in the potential measurements, is location dependent. Close to the separator, the term  $[1 - x/L]$  goes to one and the error term reaches a fixed maximum. However, as  $x$  goes to  $L$  near the current collector, the  $[1 - x/L]$  term goes to zero and the error term therefore goes to infinity. This makes sense because the potential drops become small close to the current collector so even minimal amounts of error are large compared to the magnitude of the current at these points. If this error were found to be larger or smaller, it would affect the overall shape of the error curve.

### 3.4 Error Sensitivity Analysis

In order to calculate the error associated with our current and charging current calculations, we had to estimate the amount of error in our measurements. These estimations were based on equipment sensitivities when possible and what we considered to be reasonable bounds in other cases. In this section, we consider how sensitive our results are to these error estimates. We considered three main sources of error; 1.) error from the potential measurements,  $E_\phi$ , 2.) error in our conductivity estimation,  $E_\sigma$ , and 3.) error in the measured spacing of the sensing layers,  $E_x$ . For the electrical sensing ES we determined  $E_\phi$  to be on the same order of magnitude as the sensitivity of our DAQ board,  $10 \mu\text{V}$ , and we calculated  $E_x$  to be  $20 \mu\text{m}$  based on the accuracy of our micrometer and the tolerances of the materials we used. Finally, we determined  $E_\sigma$  to be  $10 \text{ S/m}$  based on the accuracy of the sourcemeter used to make resistance measurements and the calipers used to make length measurements. While

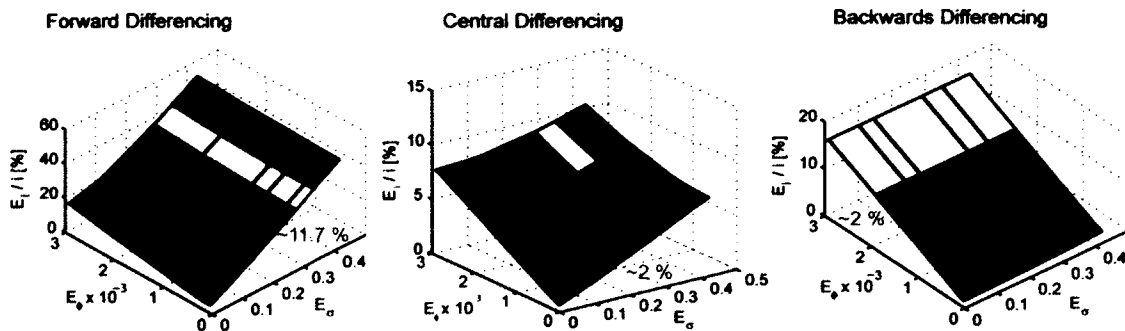
these errors were fairly small, the results discussed in chapter 4 will show that they are still significant in relation to the voltage readings obtained from this device. Therefore, the error sensitivity for the electrical ES is not shown as we believe the ionic ES will play a more important role in our future work.

For the ionic ES, we again used a value of 20  $\mu\text{m}$  for  $E_x$  since the same measurement devices were used to determine the sensing layer locations. We used our best judgment to make estimations for  $E_\phi$  and  $E_\sigma$  as there were no direct calculations for these. To estimate  $E_\phi$ , we had to consider the sensitivity of our DAQ board as well as the fact that we are now measuring our potential through the use of REs. Taking these points into account, we chose to estimate  $E_\phi$  as 0.5 mV. Finally, we estimated  $E_\sigma$  to be 0.1 S/m, which is about 7% of the conductivity value used. We believe this is reasonable based on the variations we saw in the estimations of the conductivity from fitting the data in MATLAB.

To more fully understand the strengths and limitations of our results we looked at the sensitivity of our data to the three main sources of error. We did this by varying the amount of potential, conductivity and thickness error over at least an order of magnitude and determining the resulting error in our current calculations for all the combinations of error values. The results can be seen in Figure 3.2 and Figure 3.3. In both figures, a range of potential and conductivity errors have been plotted versus the resulting percentage error for the local current (top row) or charging current (bottom row). The variance related to changing the thickness error is not shown as it was found

to be negligible over a reasonable range of values. For each of the current calculations, we plotted the sensitivity related to the forward, backward and central difference calculations as these are found using different equations. We chose to use a representative central difference point to plot rather than show all points as the trends in these plots will be similar. Finally, we looked at an early point in the charging cycle (Figure 3.2) and a later point in the charging cycle (Figure 3.3) to see if the trends change over time.

Error Sensitivity for Local Current Calculation:



Error Sensitivity for Volumetric Charging Current Calculation:

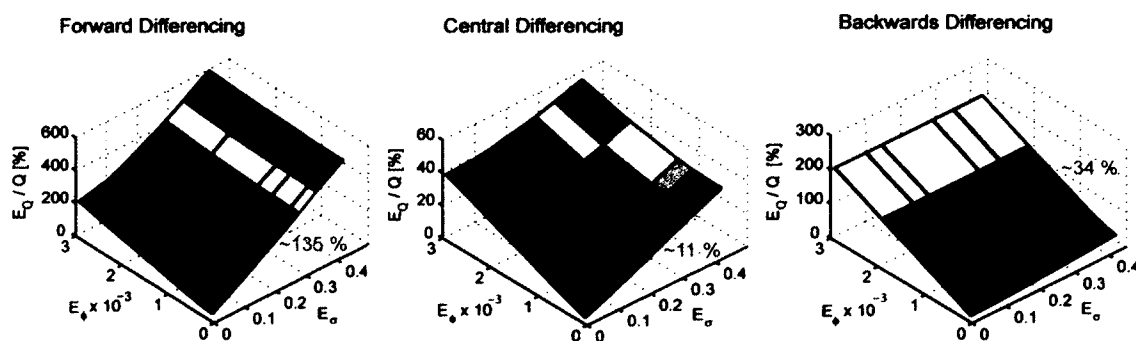
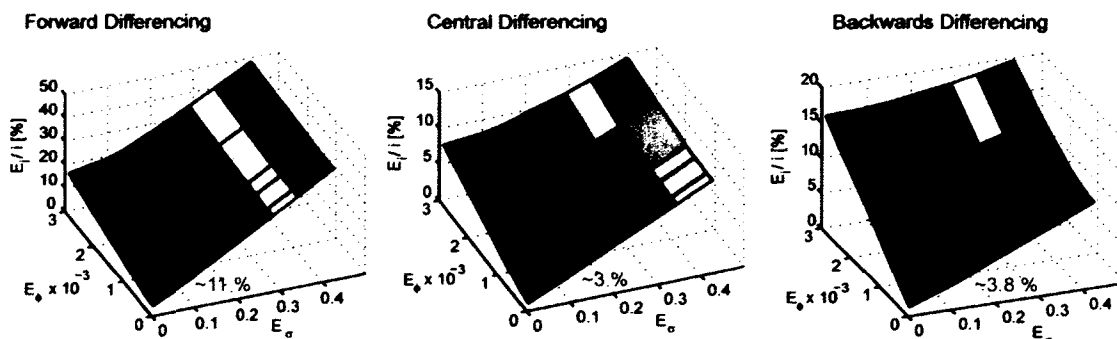


Figure 3.2 Error sensitivity plots for local current (top row) and charging current (bottom) at about 4 minutes of charging. In both cases the sensitivity is plotted for forward and backward difference cases as well as a representative central difference case. Red dots and percentage values denote the errors that are used in our final analysis. Sensitivity towards  $E_x$  is not shown as there is no noticeable effect within reasonable error bounds.

Error Sensitivity for Local Current Calculation:



Error Sensitivity for Volumetric Charging Current Calculation:

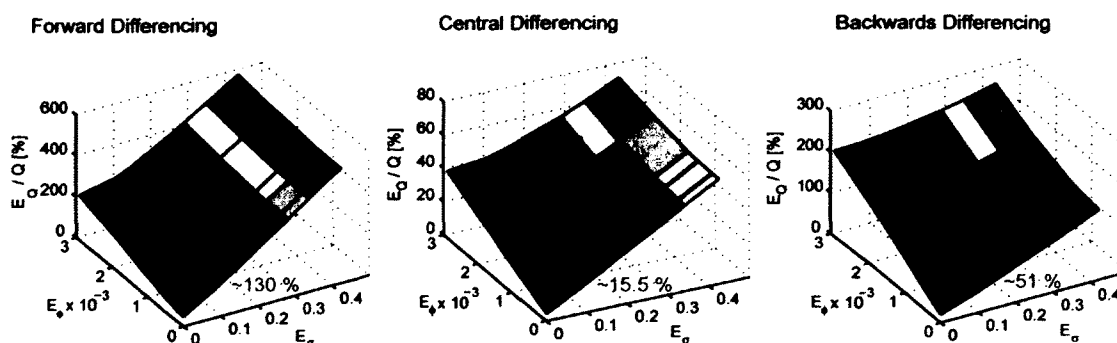


Figure 3.3 Error sensitivity plots for local current (top row) and charging current (bottom) at about 15 minutes of charging. In both cases the sensitivity is plotted for forward and backward difference cases as well as a representative central difference case. Red dots and percentage values denote the errors that are used in our final analysis. Sensitivity towards  $E_x$  is not shown as there is no noticeable effect within reasonable error bounds.

The plots of the error sensitivity show some notable trends. First, we find that the total error in the central difference calculations remains reasonable for a wide range of potential and conductivity values. This is especially true for the local current calculations, but holds true to a lesser extent for the charging current calculations as well. However, these plots show that we must be careful with our end points, especially the point closest to the separator, as these can be quite sensitive to error.

Looking more closely at the sensitivity plots for the forward and backward differences, we see that trends for the potential error are very consistent, however the forward difference is much more sensitive to the error in the conductivity than the backwards difference. This is due to the relatively large potential drop between the sensing layers closest to the separator. A small change in the conductivity leads to a large change in the slope at these points, but near the current collector, where the potential drops are smaller, the slope will not change as drastically with a change in the conductivity. In agreement with this, it can be seen that the backwards difference becomes more sensitive to the conductivity error further into the charging cycle where more charging is occurring near the current collector and the potential difference between sensing layers on this end of the electrode begins to increase. It is important to note, however, that the total error corresponding to the potential and conductivity error values that we are using in our analysis remains relatively constant over time.

Analysis of the error sensitivity of our system has revealed that our central difference calculations are quite robust, but our end point calculations are not quite as reliable as we would like them to be. The total error for the central difference is reasonable at the potential and conductivity error values that we have chosen, both for the local current and charging current calculations and this value does not change significantly throughout the charging cycle. Additionally, the total error remains reasonable for the points closely neighboring our chosen potential and conductivity error values. However, it would be beneficial to find a way to decrease the error associated with the forward and backward differences. There are a number of methods by which the error



at the end points may be decreased. Determining a way to obtain more accurate conductivity measurements could significantly decrease the error of the forward difference and, in some cases, the backward difference. Furthermore, the accuracy of the REs could be more thoroughly investigated to potentially decrease the error estimate, more sensitive equipment could be used to make the potential measurements and additional sensing layers could be added near the end points to increase the spatial resolution. Finally, the setup could be tested to determine if there is a systematic offset in the measurements. This type of error would affect the absolute values of the measured points, but would not affect the shape of the curves or the conclusions drawn from the data as these are dependent only on the differential between the measured points. If there is a systematic offset then our error bars may be significantly smaller than we have estimated here.

### **3.5 Optimal Spacing Analysis**

The distribution data gathered with the ionic ES (presented and discussed in Chapter 5) was used to analyze the spacing between sensing layers to determine if the error could be reduced through decreasing or increasing the distance between the sensing layers. To properly analyze the layer spacing, we had to consider two competing types of error, uncertainty error and truncation error. The uncertainty error, which has already been discussed in detail in previous sections, is independent of the layer spacing. Therefore, this error would become a larger percentage of the potential measurements if the sensing layers were moved closer together thereby decreasing the

potential drop between sensing layers. However, the truncation error tends towards zero as the number of sensing layers approaches infinity. We must balance these two types of errors in order to determine the optimal layer spacing for the ES.

We considered an early time during the charging cycle as this is when the potential drops between layers are the smallest and the calculations will be most affected by the addition or subtraction of data. The problem was constrained by fixing the electrode length and the placement of the first and last sensing layers. This ensured that the calculations always drew from data within the measured distribution. A polynomial was fit to the measured potential distribution data using MATLAB to obtain a continuous function with which to do the optimization calculations. We assumed that the conductivity and the sensing layer spacing were uniform through the electrode's thickness. The sensing layer positions were used in conjunction with the polynomial fit from MATLAB to determine the potential at each sensing layer. The local current, charging current and the associated uncertainty errors were calculated as discussed in sections 3.1 and 3.3 based on the new spacing/potential points. The truncation error (TE) was also calculated and added to the uncertainty error to determine the total error for each case.

The TE was calculated using third, fourth and fifth order terms from the central difference equation. Finding the TE for the local current was straightforward as we were able to calculate the derivatives from the polynomial fit to the potential distribution data. The derivatives were used in conjunction with equation [3.33] to

determine the TE associated with calculating the local current at each sensing layer. It is important to note that we are assuming a constant conductivity through the electrode for the ionic ES data, which means that the standard central difference equation can be used rather than the one developed previous and shown in equation [3.13].

$$i_m = \sigma \frac{\partial \phi}{\partial x} \Big|_{x_m} = \sigma \left[ \frac{\phi_{m+1} - \phi_{m-1}}{2\Delta x} + \frac{\Delta x^2}{3!} \frac{\partial^3 \phi}{\partial x^3} \Big|_{x_m} + \frac{\Delta x^3}{4!} \frac{\partial^4 \phi}{\partial x^4} \Big|_{x_m} + \frac{\Delta x^4}{5!} \frac{\partial^5 \phi}{\partial x^5} \Big|_{x_m} + \dots \right] \quad [3.33]$$

$$\text{So, } TE = \left[ \frac{\Delta x^2}{3!} \frac{\partial^3 \phi}{\partial x^3} \Big|_{x_m} + \frac{\Delta x^3}{4!} \frac{\partial^4 \phi}{\partial x^4} \Big|_{x_m} + \frac{\Delta x^4}{5!} \frac{\partial^5 \phi}{\partial x^5} \Big|_{x_m} + \dots \right]$$

To find the TE for the charging current points, we had to consider the TE associated with calculating the charging current, and additionally incorporate the error associated with calculating the local current since the local current values are used when calculating the charging current. The central difference equation used to find a given charging current point is shown in [3.34].

$$i_c = \frac{\partial i}{\partial x} = \sigma \frac{\partial^2 \phi}{\partial x^2} \text{ so,} \quad [3.34]$$

$$i_{c,m} = \frac{\partial i}{\partial x} \Big|_{x_m} = \frac{i_{m+1} - i_{m-1}}{2\Delta x} + \frac{\Delta x^2}{3!} \frac{\partial^3 \phi}{\partial x^3} \Big|_{x_m} + \frac{\Delta x^3}{4!} \frac{\partial^4 \phi}{\partial x^4} \Big|_{x_m} + \frac{\Delta x^4}{5!} \frac{\partial^5 \phi}{\partial x^5} \Big|_{x_m} + \dots$$

Equation [3.33] is then used to find  $i_{m+1}$  and  $i_{m-1}$ :

$$\begin{aligned}
i_{m+1} &= \sigma \left. \frac{\partial \phi}{\partial x} \right|_{x_{m+1}} = \sigma \left[ \frac{\phi_{m+2} - \phi_m}{2\Delta x} + \frac{\Delta x^2}{3!} \left. \frac{\partial^3 \phi}{\partial x^3} \right|_{x_{m+1}} + \frac{\Delta x^3}{4!} \left. \frac{\partial^4 \phi}{\partial x^4} \right|_{x_{m+1}} + \frac{\Delta x^4}{5!} \left. \frac{\partial^5 \phi}{\partial x^5} \right|_{x_{m+1}} + \dots \right] \\
i_{m-1} &= \sigma \left. \frac{\partial \phi}{\partial x} \right|_{x_{m-1}} = \sigma \left[ \frac{\phi_m - \phi_{m-2}}{2\Delta x} + \frac{\Delta x^2}{3!} \left. \frac{\partial^3 \phi}{\partial x^3} \right|_{x_{m-1}} + \frac{\Delta x^3}{4!} \left. \frac{\partial^4 \phi}{\partial x^4} \right|_{x_{m-1}} + \frac{\Delta x^4}{5!} \left. \frac{\partial^5 \phi}{\partial x^5} \right|_{x_{m-1}} + \dots \right]
\end{aligned} \quad [3.35]$$

These equations can be directly substituted into [3.34] to find:

$$\begin{aligned}
i_{c,m} &= \frac{\sigma \left[ \frac{\phi_{m+2} - \phi_m}{2\Delta x} + \frac{\Delta x^2}{3!} \left. \frac{\partial^3 \phi}{\partial x^3} \right|_{x_{m+1}} + \frac{\Delta x^3}{4!} \left. \frac{\partial^4 \phi}{\partial x^4} \right|_{x_{m+1}} + \frac{\Delta x^4}{5!} \left. \frac{\partial^5 \phi}{\partial x^5} \right|_{x_{m+1}} + \dots \right]}{2\Delta x} \\
&\quad - \frac{\sigma \left[ \frac{\phi_m - \phi_{m-2}}{2\Delta x} + \frac{\Delta x^2}{3!} \left. \frac{\partial^3 \phi}{\partial x^3} \right|_{x_{m-1}} + \frac{\Delta x^3}{4!} \left. \frac{\partial^4 \phi}{\partial x^4} \right|_{x_{m-1}} + \frac{\Delta x^4}{5!} \left. \frac{\partial^5 \phi}{\partial x^5} \right|_{x_{m-1}} + \dots \right]}{2\Delta x} \\
&\quad + \frac{\Delta x^2}{3!} \left. \frac{\partial^3 \phi}{\partial x^3} \right|_{x_m} + \frac{\Delta x^3}{4!} \left. \frac{\partial^4 \phi}{\partial x^4} \right|_{x_m} + \frac{\Delta x^4}{5!} \left. \frac{\partial^5 \phi}{\partial x^5} \right|_{x_m} + \dots
\end{aligned} \quad [3.36]$$

$$\begin{aligned}
\text{so, } TE &= \frac{\sigma \left[ \frac{\Delta x^2}{3!} \left. \frac{\partial^3 \phi}{\partial x^3} \right|_{x_{m+1}} + \frac{\Delta x^3}{4!} \left. \frac{\partial^4 \phi}{\partial x^4} \right|_{x_{m+1}} + \frac{\Delta x^4}{5!} \left. \frac{\partial^5 \phi}{\partial x^5} \right|_{x_{m+1}} + \dots \right]}{2\Delta x} \\
&\quad - \frac{\sigma \left[ \frac{\Delta x^2}{3!} \left. \frac{\partial^3 \phi}{\partial x^3} \right|_{x_{m-1}} + \frac{\Delta x^3}{4!} \left. \frac{\partial^4 \phi}{\partial x^4} \right|_{x_{m-1}} + \frac{\Delta x^4}{5!} \left. \frac{\partial^5 \phi}{\partial x^5} \right|_{x_{m-1}} + \dots \right]}{2\Delta x} \\
&\quad + \frac{\Delta x^2}{3!} \left. \frac{\partial^3 \phi}{\partial x^3} \right|_{x_m} + \frac{\Delta x^3}{4!} \left. \frac{\partial^4 \phi}{\partial x^4} \right|_{x_m} + \frac{\Delta x^4}{5!} \left. \frac{\partial^5 \phi}{\partial x^5} \right|_{x_m} + \dots
\end{aligned}$$

The first two terms of the TE from [3.36] have already been calculated from finding the TE for the local current calculations and can easily be plugged in here. To find the

third term, we again use MATLAB to find a polynomial fit, this time to the local current curve, and use that to directly calculate the derivatives.

Both the uncertainty error and truncation error are calculated at each sensing layer for every variation of total number of sensing layers considered. In order to easily compare the error for various numbers of layers, an average error value is calculated. Only the interior points are considered in the average since the error equations are based on the central difference. A standard average is used to determine the average uncertainty error and the average truncation error and the two values are added together to determine a total overall error value for that case. It is important to note that the charging current equation uses the  $m+2$  and  $m-2$  indices so the minimum number of layers we can consider is 5. If we were interested in finding the error for fewer sensing layers, we would have to adjust our equations to take into account error for forward and backward differences.

The results of the error calculations are plotted in Figure 3.4 and Figure 3.5. In these plots, the total error on the current and charging current calculations has been normalized by the current or volumetric charging current used to charge the cell, respectively, and has been plotted versus the number of sensing layers. The minimum error for the current is found to occur at 10 layers, while the minimum error for the charging current is found to occur at 7 layers. This corresponds to a layer spacing of 0.61 to 0.92 mm respectively. Looking more closely at the percentage error values it can be seen that the error in the current data is much smaller than the error in the

charging current data. For this reason, we should choose to use 7 layers instead of 10, which is what was used to obtain the data in Chapter 5. This suggests that we would not benefit from placing sensing layers closer to one another unless we can decrease our uncertainty error. A higher resolution ES design may still be of interest to us however, even if we are not able to use more precise measurements devices. It may be that some of the uncertainty error in the measurements is due to a systematic offset. While this would reduce the accuracy of the measurements, the shape of the curves would remain constant because the differential between measurement points would not change. Since many of our conclusions are based on the shape of the curves rather than the absolute values of the points, having a systematic offset in the data would likely not change our conclusions and we could therefore consider our error to be smaller than it is currently. Additionally, it may be beneficial to increase the sensing layer resolution at the end points to lend credence to the accuracy of our end point measurements.

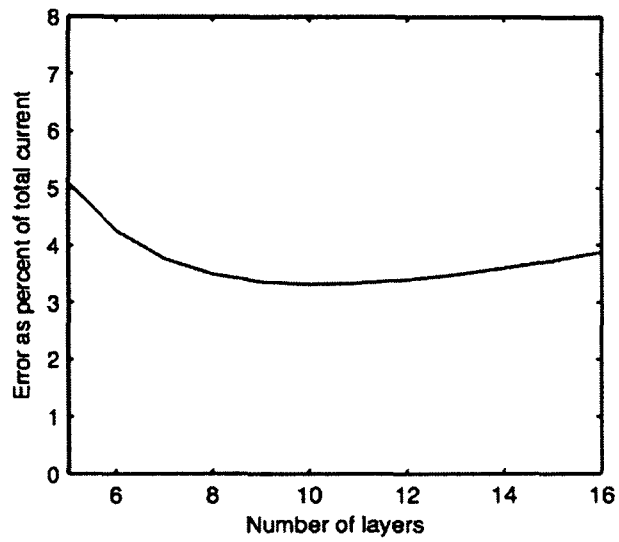


Figure 3.4 Total error associated with calculating the local current shown as a percentage of the total current used to charge the cell and as a function of the number of sensing layers used.

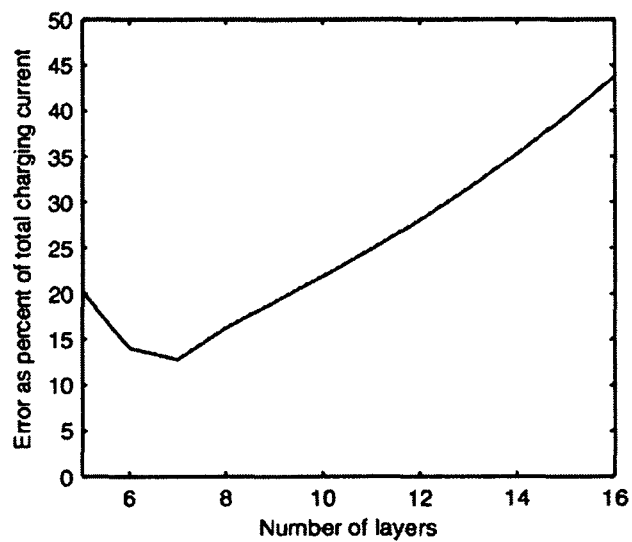


Figure 3.5 Total error associated with calculating the charging current shown as a percentage of the total volumetric charging current used to charge the cell and as a function of the number of sensing layers used.

### 3.6 Summary

In this chapter we developed a mathematic method for calculating local current, volumetric charging current and amount of charge stored from potential measurements made at known distances through the electrode thickness. The finite difference method developed can be applied to electric or ionic potential data and can include bulk or local conductivity values. The error of the calculations due to inaccuracies in the measurements taken was assessed using error propagation methods.

The sensitivity of our calculations based on the error was evaluated by plotting the total error in our calculations over a wide range of the three main sources of error: potential, conductivity and thickness measurement errors. It was determined that the thickness measurement error did not significantly affect the total error and that the effects of the potential and conductivity errors varied depending on whether the point was calculated using the forward, central or backwards difference method. We believe that our central difference calculations are quite robust, but the error associated with the forward and backward difference calculations could be improved. The spacing of the sensing layers in the ionic ES was also evaluated. It was determined that a layer spacing of 0.92 mm, corresponding to 7 layers in this case, would be optimal for the ionic ES under the conditions considered in this analysis. Since this was the layer spacing already in place for the ionic ES experiments, other methods for decreasing the uncertainty error in the ionic ES must be established for future iterations.



## Chapter 4

# An ES for Gathering Electric Potential Distributions Across a Symmetric EDL Capacitor Electrode

The aqueous sodium hybrid battery we study in this chapter combines a  $\text{Na}_4\text{Mn}_9\text{O}_{18}$  intercalation positive electrode with an electric double layer (EDL) capacitance negative electrode, and a 1 M aqueous sodium electrolyte. While this technology is particularly attractive due to the low cost and benign materials used, there are major losses that occur in the negative electrode due to the finite mobility of the ions and limited transport rates across the electrode. These losses, which are exacerbated by increasing the thickness of the electrode, are a particular impediment to further cost and performance improvements in this technology. This is because the low energy density of the negative electrode requires it to be thick compared to the positive electrode to properly balance the accessible charge-storage capacities between the two electrodes [24]. Additionally, a well accepted method to improve the commercial viability of these hybrid batteries is to increase the electrode thicknesses so that more

charge can be stored with less geometric area thereby decreasing the amount and cost of non-functional materials needed for the cell (i.e. separator, current collector, packaging, etc.) [6, 7]. In order to assess these issues, we have created a novel method for making *in situ*, through-thickness electric potential measurements in an activated carbon EDL capacitance negative electrode. We have chosen to study the negative electrode of a symmetric EDL capacitor, which will function the same as the negative electrode in the hybrid battery, for simplicity. We believe that the data gathered from this device will allow us to better characterize the charging and discharging cycles of the electrode and eventually lead to further electrode improvements.

## 4.1 Experimental Setup

The electric potential sensing electrode scaffold (ES) consists of alternating stainless steel sensing and Teflon insulating layers surrounding a 1-D column of working electrode material; in this case the negative electrode of a symmetric EDL capacitor. Building off the knowledge we gained while creating the MES, we made sure to design the ES such that there was adequate spacing between the sensing layers and an aspect ratio that allowed for nearly 1-D transport without showing significant edge effects. This section will detail the full design of the ES, the cell hardware and packing of the electrode.

### **4.1.1 Electric ES Build and Cell Assembly**

An ES with electric potential sensing layers was built to study the negative electrode of a symmetric aqueous  $\text{Na}^+$  EDL capacitor cell. The ES was constructed using 0.102 mm thick stainless steel sensing layers (TBI, Countryside, IL) that were cut into squares with a long protruding tab to be used as an electrical connection. Squares of 0.575 mm thick adhesive Teflon (Avrey Dennison, Pasadena, CA) were then adhered to both sides of the sensing layers. The resulting layers were stacked together with double-sided tape (3M, St. Paul, MN, 0.078 mm) in a manner such that each sensing layer tab protruded from the structure in a different direction, allowing easy access to each layer. The resulting ES stack had a thickness of 9.3 mm. Finally, a 2.38 mm diameter hole was drilled into the center of the ES and two small holes for alignment pins were drilled into the corners of the stack.

An acrylic housing was used to make the positive electrode housing. The acrylic had a thickness of 11.2 mm so that it would be similar in thickness to the negative electrode, but slightly oversized so that it would not limit the performance of the negative electrode. The acrylic housing also had a 2.38 mm diameter hole and two alignment pin holes drilled into it to match the electric ES structure and ensure that the two cylindrical electrodes would align properly after assembly.

The packing of the electrodes into the ES and the acrylic housing was carried out by alternating between depositing a small amount of activated carbon powder (YEC-8 EDLC activated carbon, Fuzhou Yihuan Carbon Co., Fuzhou, China) and injecting

1 M Na<sub>2</sub>SO<sub>4</sub>(aq) into the holes. A rod with the same diameter as the holes was then used to tightly pack down the activated carbon and electrolyte. This process was continued until the holes were completely filled. A small mound (< 1 mm) was left protruding from each side of both electrode housings to ensure contact between the electrodes, as well as between the electrodes and the respective current collectors. The mass of the activated carbon needed to fill both the negative and positive electrodes of the capacitor was ca. 0.08 g. The current collectors were secured to the housing using adhesive Kapton (McMaster-Carr, Princeton, NJ).

The two electrodes were assembled together with a piece of cotton filter paper separator (Ahlstrom Grade-40, Helsinki, Finland) soaked in 1 M Na<sub>2</sub>SO<sub>4</sub> aqueous electrolyte placed in between them. They were then clamped together using 6.35 mm thick stainless steel plates (McMaster-Carr) that were electrically insulated by adhesive Kapton films. Finally, the cell was sealed with epoxy (Loctite, Poxy Pak, Germantown, WI) to prevent solvent evaporation from the separator's perimeter. A schematic of the electrode assembly and a picture of the final cell assembly can be seen in Figure 4.1a and b respectively.

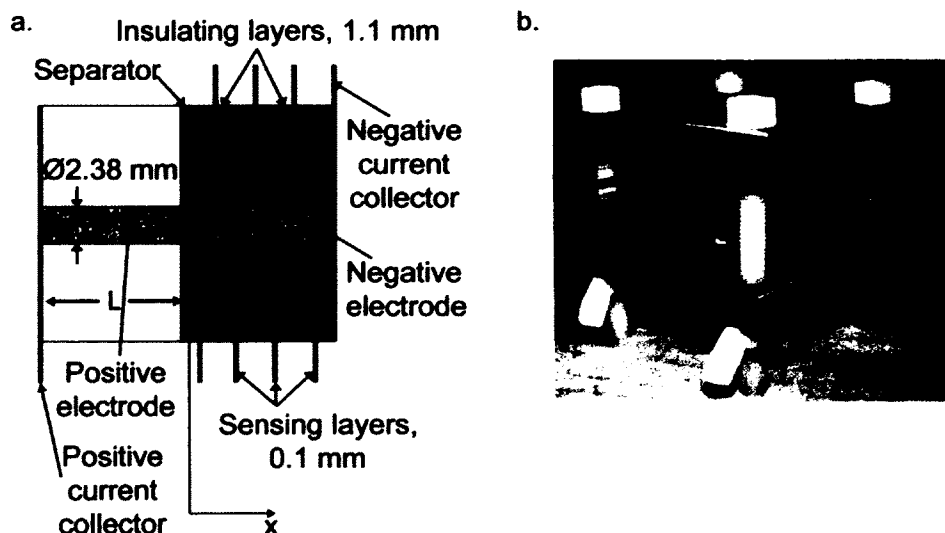


Figure 4.1 a. Schematic of the ES cross-section showing the alternating sensing and insulating layers on the negative electrode. b. A photo of an assembled ES.

### 4.1.2 Equipment and Testing Procedures

Once the capacitor was completely assembled, the cell terminals were connected to a potentiostat (VSP, Bio-logic, Knoxville, TN) to control the charging and discharging of the cell. Additionally, each of the stainless steel tabs protruding from the sensing layers were connected to the differential voltage measurement inputs on a data acquisition board (DAQ) (National Instruments, Austin, TX) where the voltages would all be measured with respect to the negative current collector. The input impedance of the differential voltage measurement is specified by manufacturer as  $>10 \text{ G}\Omega$ , yielding negligible stray current through the DAQ. Prior to conducting charging and discharging experiments, 5 cycles of cyclic voltammetry (CV) were performed at  $0.1 \text{ mV/s}$  between  $0 \text{ V}$  and  $0.9 \text{ V}$  to condition the cell and to assess the capacitance of the EDL capacitor. Constant voltage charging was then conducted at

0.9 V for four hours, followed by four hours of constant current discharging at 22.5 A/m<sup>2</sup>. Additional constant current discharging experiments were conducted at 225 A/m<sup>2</sup>, 169 A/m<sup>2</sup> and 112 A/m<sup>2</sup>, where each discharge proceeded until the cell voltage dropped to zero. The cell was charged at 0.9 V for four hours before every discharge experiment. Electric potential data from the sensing layers was collected during all of the experiments.

## **4.2 Preliminary Testing Results**

A few preliminary tests were conducted on the ES before and after the capacitor was fully assembled. The pre-assembly tests allowed us to gather resistance distribution data through the electrode as well as assess the effects of the compression plates on the conductivity values and distribution. We also made resistance distribution measurements on the assembled cell to compare with the pre-assembly values. Using these measurements with the known geometry of the cell, we were able to calculate local conductivity values. This is a unique measurement that had not been possible before the development of the ES. Furthermore, much like for the MES, we conducted standard cell-terminal analysis on the cell using the ES as well as a cell using only acrylic for the electrode housings to see if the ES had any affect on the cell performance.

### 4.2.1 Conductivity Measurements

The electric ES has allowed us to find local conductivity values through the negative electrode by enabling us to obtain resistance measurements between sensing layers and using this data along with known cell geometry to calculate the conductivity values. These resistance distribution measurements were made on the ES in two different arrangements. First, these measurements were made using the ES before it was fully assembled with the separator and positive electrode. In this pre-assembly arrangement, which can be seen in Figure 4.2, stainless steel current collectors were placed on both ends of the electrode packed in the ES housing and were connected to the current leads on a sourcemeter (Keithley 2410 1100V SourceMeter, Cleveland, OH). Another set of Keithley leads were then connected to pairs of sensing tabs to measure the resistance between each tab pair. This arrangement allowed us to make use of the Keithley's 4-wire sense mode. In this mode, a small amount of current is sent through the outer current leads and the resistance is measured between the inner voltage leads. This method is more accurate than if we used shared current and voltage leads. There are two uses for this measurement in the unassembled arrangement: 1) to compare the conductivity before and after compressing the electrode, 2) to obtain a value for the conductivity between the two sensing layers closest to the separator.

These resistance distribution measurements were made again once the cell was fully assembled. The assembled arrangement, also shown in Figure 4.2, was set up similarly except the current leads from the sourcemeter were connected to the negative current collector and the sensing tab nearest to the separator. This configuration did not allow

for the measurement of the resistance between the two sensing layers closest to the separator, but we estimated this resistance using the value from the pre-assembly configuration and relative change in the resistances between the unassembled and assembled measurements.

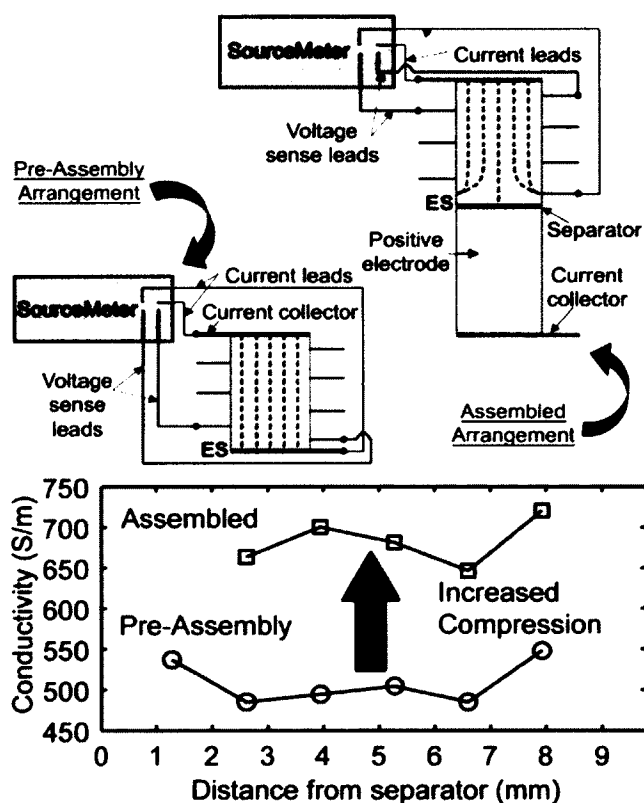


Figure 4.2 Conductivity through the thickness of the negative electrode using both pre-assembled and assembled configurations of the ES.

Figure 4.2 presents the conductivity distributions obtained from resistance measurements before and after assembly. The results show roughly uniform conductivities, however, we see about a 7–10% increase in conductivity at the edges and a roughly 35% increase from the pre-assembly to the assembled configuration.



The end point increases are likely due to higher compression at these points because of the protruding mounds of electrode material, and a concentration of the compression at the ends. The overall increase with assembly stems from higher compression of the cell from the end plates when it is fully assembled with a compressible separator that can intrude a small amount into the ES hole. The roughly constant conductivity throughout suggests that there is good carbon connectivity and that there are no voids in the electrode that would significantly affect our electric potential readings during the following studies. We are also able to use these local conductivity values to more accurately calculate the local current, volumetric charging current, and charge stored or discharged once we have potential distribution data from the ES. However, as previously stated we were only able to obtain the conductivity between the two tabs next to the separator,  $\sigma_{1,2}$ , in the pre-assembly setup. To estimate  $\sigma_{1,2}$  for the fully assembled cell we set the ratio of the overall average conductivity for both cases to the ratio of  $\sigma_{1,2}$  for both cases:  $\sigma_{1,2,assem} = \sigma_{1,2,pre-assem} \left( \sigma_{Avg, assem} / \sigma_{Avg, pre-assem} \right)$ .

#### 4.2.2 Conventional Cell-Terminal Characterization

CV and charge/discharge cycles were performed on the EDL capacitor to initially condition the cell for repeatable behavior and characterize the cell by conventional cell-terminal analysis. These tests were conducted using the parameters discussed in the experimental section. The CV tests allowed us to obtain the capacitance of the electrode and provided us with data to compare to a standard EDL capacitor in order to assess the effects of the ES on the cell's performance. Figure 4.3 shows the results

of the CV experiment run on a capacitor using the ES. The shape of the cyclic voltammogram in Figure 4.3 indicates a resistive behavior, which is generally observed at scan rates much higher than 0.1 mV/s in more conventional EDL capacitors [26]. A slow scan rate was required here because of the slow diffusion time-scale,  $t_L = L^2/4D_{eff, Na^+}$ , expected for the thick electrodes. Assuming a  $Na^+$  diffusivity of  $1.33 \times 10^{-5} \text{ cm}^2/\text{s}$  [53], and a formation factor (porosity/tortuosity) of 0.1, the diffusion time-scale for a 1 cm thick electrode is around 44 hr. We calculated the full cell's capacitance from the CV data by integrating the area under the forward sweep curve and subtracting the integrated area under the backward sweep curve. Using this method, we calculated a specific capacitance of 17.3 F/g.

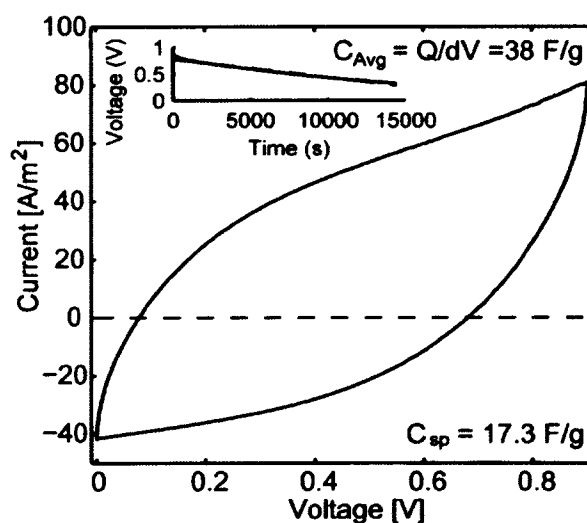


Figure 4.3 CV conducted at  $40 \text{ A/m}^2$  (0.1 mV/s) from 0 V to 0.9 V, yielding a capacitance of 17.3 F/g. The inset shows data for a constant current discharge held at  $22.5 \text{ A/m}^2$  for four hours that gives a comparable capacitance result of 38 F/g when taking the slower discharge rate into consideration.

We were able to verify that the ES and the potential measurements do not alter the capacitor performance by conducting an additional set of CV measurements on a capacitor that used acrylic housings for both electrodes, but was otherwise the same setup as the EDL capacitor with the ES. In that experiment, the capacitance of the cell was about 18.2 F/g, which means there is a standard deviation of 0.67 F/g between the ES cell and the all acrylic cell. Both CVs are plotted together on the same scale in Figure 4.4 for comparison. The low capacitance values seen in both setups is likely due to the large thickness of the electrodes and perhaps incomplete wetting of the activated carbon. It is also interesting to note that both CVs appear to have a  $\sim 20$  A/m<sup>2</sup> offset, perhaps due to a parasitic reaction current occurring during operation.

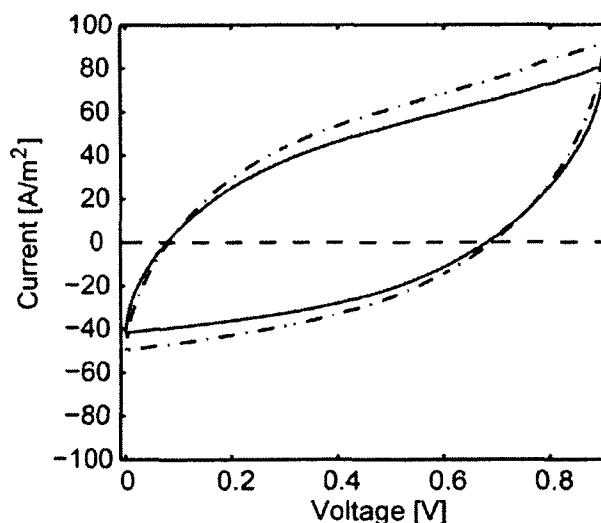


Figure 4.4 CV comparison between the ES (solid line) and an all acrylic capacitor with the same dimensions (dashed line). Similar shapes and areas dictate that the ES does not affect the performance of the electrode.

In addition to CV, we also experimentally characterized the capacitance from data gathered during a 22.5 mA/cm<sup>2</sup> constant current discharge experiment (Figure 4.3 inset), which is another common cell-terminal characterization method. The discharge cycle was conducted after 5 cycles of CV and 4 hours of charging at 0.9 V. We used equation [4.1] to analyze the discharge data. In this equation,  $Q$  is the charge storage capacity,  $I$  is the current used to discharge the cell,  $dV$  is the total drop in voltage, and  $dV/dt$  is the change in voltage over time, which was determined from the slope of the discharge curve, and  $C$  is the capacitance of the cell. From equation [4.1] we find the capacitance has a value of 38 F/g, which is roughly double that from the CV data because of the lower currents used during the discharge cycle. While the CV was conducted at 0.1 mV/s, corresponding to a discharge current of about 40 A/m<sup>2</sup>, the constant current discharge was conducted at only about half that current, 22.5 A/m<sup>2</sup>. It is well documented that the capacitance decreases with increasing discharge rates or CV scan rates [26, 28]. Additionally, we observe a sharp drop at the start of the discharge data, which is due to the internal resistance [29]. Despite reasonably good agreement between the two methods, the capacitance value is much lower than would be expected for this activated carbon material in thin electrodes [54]. However, we do believe that the similar shapes and areas of the two CVs suggests that the ES does not affect the performance of the electrode and that the measurements we obtain using the ES will be representative of standard operating conditions.

$$Q = \int_{t_1}^{t_2} I/(dV/dt) dV, \text{ where } C = Q/dV \quad [4.1]$$

## 4.3 Electric ES Results

Electric potential distribution measurements were obtained from the ES during potentiostatic charging at 0.9 V and during galvanostatic discharging at multiple discharge current densities: 225 A/m<sup>2</sup>, 169 A/m<sup>2</sup> and 112 A/m<sup>2</sup>. The results, which are presented in detail in the following sections, were analyzed using the mathematical methods derived and discussed in chapter 3 to obtain local current, charging current and volumetric charge stored.

### 4.3.1 Potentiostatic Charging

Potentiostatic charging of the EDL capacitor was conducted at 0.9 V. This voltage was chosen because it is below that for water electrolysis, which is crucial when using an aqueous electrolyte. Figure 4.5a shows the raw ES data from a charging cycle conducted immediately after the CV scans were completed. In this plot, the data after 60 s has been smoothed using Gaussian convolution with a standard deviation of 15 s. The first 60 s have not been altered because of the fast transients and order of magnitude higher signal compared to the data after 60 s. Each line in Figure 4.5a corresponds to a different sensing layer as shown in the bottom left inset. The uppermost line corresponds to the sensing layer closest to the separator, while the bottom line is from the sensing layer farthest away. The top right inset shows the corresponding current/time data. Evidence of non-uniform charging can be seen in the raw ES voltage data. At early times, the lines appear to be evenly distributed indicating equal voltage differences, but as the charging proceeds, the lines for the

three sensing layers closest to the separator (top three lines) begin to collapse upon each other, while the bottom lines remain evenly spaced apart. Since the electron phase current is proportional to the voltage gradient, the initial uniform spacing indicates the current was constant in regions of the electrode between the sensing layers at early times. This suggests that all of the charging initially occurs between the separator and the first sensing layer as expected. The subsequent closer spacing of the voltages measured near the separator indicates that the current is being consumed by charging in these regions at later times.

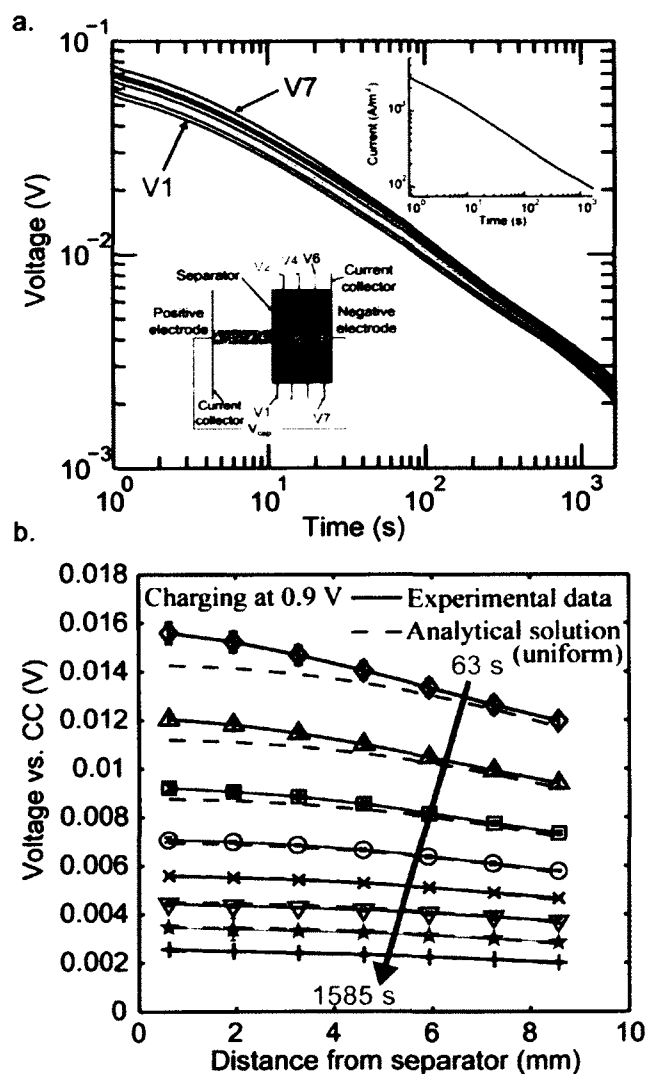


Figure 4.5 Constant voltage charging at 0.9 V. a. Voltage-time series showing raw potential data from the ES. The top right inset is the corresponding current-time series. The bottom left inset shows the placement of each sensing layer on the ES structure. b. Voltage versus the current collector as a function of the distance away from the separator at eight logarithmically distributed times. The dashed lines are fits to the analytical solution for uniform charging and conductivity. Deviations between the solid experimental data lines and the dashed analytical solution lines indicate non-uniform charging. Symbols denote times plotted:  $\diamond$  - 63 s,  $\triangle$  - 100 s,  $\square$  - 159 s,  $\circ$  - 251 s,  $\times$  - 398 s,  $\nabla$  - 631 s,  $\star$  - 1000 s,  $+$  - 1585 s.

These voltage gradients and curvatures can be seen more clearly in Figure 4.5b. Here, the voltage is plotted versus the distance through the electrode at multiple times. The analytical solution for uniform charging and conductivity is also plotted for comparison [55]. Similarly to the analytical solution found for the PEM fuel cell, the analytical solution for the EDL capacitor was derived from the conservation of current equation presented in equation [1.4]. However, in this case, the fixed potential boundary condition is applied at the current collector,  $\phi|_{x=L} = \phi_o$ , and the zero current boundary condition is applied at the separator,  $\partial\phi/\partial x|_{x=0} = 0$ , leading to:

$$\phi = \frac{-IL}{2A\sigma_{eff}} \left[ \left( \frac{x}{L} \right)^2 - 1 \right] + \phi_o \quad [4.2]$$

where  $\phi$  is the potential at a given point through the electrode assuming uniform charging and conductivity,  $I$  is the cell current,  $L$  is the total length,  $A$  is the surface area,  $\sigma_{eff}$  is the average effective electric conductivity,  $x$  is the distance away from the separator and  $\phi_o$  is the potential at the interface of the electrode with the current collector. Equation [4.2] is fitted to the voltage distribution using  $I$  as a fitting parameter. All other values are known. It can be seen that at short times the analytical solution for uniform charging and experimental data do not match up well near the separator. In this case, deviance from the analytical solution indicates non-uniform charging. At later times the experiment and model fit curves overlap more, implying that the charging becomes more uniform.



The finite difference equations discussed in Chapter 3 have been used along with the voltage data to estimate the local current and volumetric charging current at the location of each sensing layer. The two current estimations are plotted versus the distance away from the separator in Figure 4.6a and b respectively. It can be seen in Figure 4.6a that at early times the local current is relatively low near the separator and quickly plateaus to a maximum value a short distance into the electrode. Since a plateau in the current data indicates a region of zero charging, this plot shows that the charging is initially concentrated near the separator in the region before the plateau begins. Two changes are identified in Figure 4.6a as time proceeds; first, the plateau diminishes and shifts toward the current collector, second, the magnitude of the current decreases in a manner consistent with charging a capacitor at constant voltage. We observe that the current near the separator does not go to zero at long times, but asymptotes to a value of 40–50 A/m<sup>2</sup>. This is likely an indicator of a stray current, and is consistent with the current offset in the CV analysis.

We also find a systematic offset in Figure 4.6a between the current estimate at the final sensing layer and the current measured by the potentiostat at the current collector. We are able to exclude any geometrical effects as we are comparing current densities, which makes them independent of the diameter and area; also inaccuracies in sensing layer spacing, within reasonable bounds, does not have a significant effect. One possible explanation that we explored was that this phenomena was a result of the well-documented change in activated carbon conductivity with polarization [56].

However, during our constant current discharge experiments (shown in Figure 4.7) we find that the current always asymptotes to the same value far away from the separator despite the decreasing potential in the cell and using a relatively constant conductivity for our calculations. This suggests that any conductivity change that may be occurring with polarization is negligible. Another possibility is that the cell conditions change during operation due to additional compression and changes in the surface properties. If this were to occur, the resistance values measured prior to testing could be too high, resulting in apparent under-estimations of the current. In Figure 4.6a, we find the relative difference was constant and that a 22% increase in conductivity across the entire electrode would yield local current density values that match those of the current collector. At this juncture, we could have scaled the current according the relative difference to account for the under-estimation of conductivity; however, we chose to present the unaltered data. Possible future work could include simultaneously or intermittently measuring conductivity using AC impedance during charging and discharging cycles of the EDL capacitor.

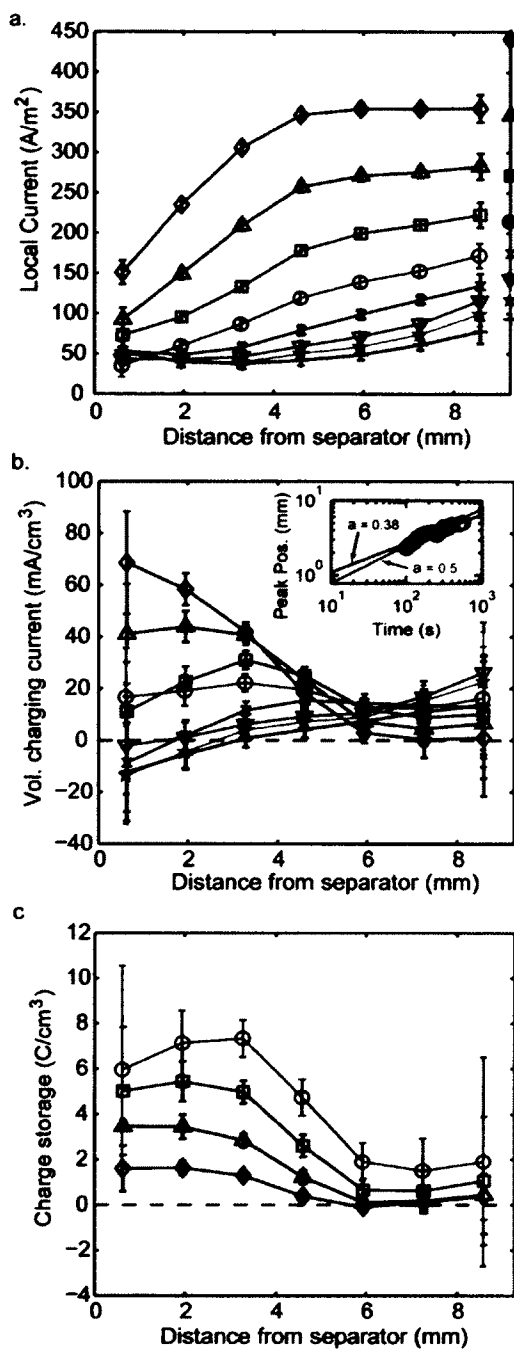


Figure 4.6 Constant voltage charging at 0.9 V. a. Local current plotted as a function of distance through the electrode. Lower currents near the separator suggest charge storage taking place here. b. Volumetric charging current through the thickness of the electrode. Charging current is high where local current was low. Inset shows the position of the charging current peak through the electrode over time. c. Charge stored through the electrode over time. In all plots:  $\diamond$  - 63 s,  $\triangle$  - 100 s,  $\square$  - 159 s,  $\circ$  - 251 s,  $\times$  - 398 s,  $\nabla$  - 631 s,  $\star$  - 1000 s,  $\dagger$  - 1585 s.

Figure 4.6b shows an initial peak in the volumetric charging current plot near the separator, which shifts toward the current collector and decreases in magnitude over time. This behavior is consistent with that inferred from the current plot in Figure 21a. At 251 s, the charging current is mostly uniform (red circles); prior to that time the charging current is concentrated in the regions closer to the separator and after that time it is concentrated more toward the current collector. This is consistent with the excellent match seen between the experimental and analytical voltage distributions from Figure 4.5b at 251 s.

In Figure 4.6b, we observe that negative charging currents are estimated near the separator at long times. Negative currents are unlikely during charging (although they may occur due to a parasitic reaction mechanism) and it is a reasonable conclusion that they arise due to the error in the second derivative estimation. Comparing Figure 4.6a and b, we see increased error estimates with each order of derivative. In addition, there is increased error in estimating the currents at the endpoints, which is a result of the forward and backward differencing formula's functional form.

We can quantify a time-scale for the propagation of charging through the electrode, by analyzing the spatio-temporal charging current data. Here, the time-scale is based on the propagation of the location of the charging current's peak. The inset in Figure 4.6b shows the location of the peak versus time with logarithmic scaling. The location of the peak is determined by the maximum of a spline fit to the discrete data. The data was fit to a general power law equation,  $x_p = bt^\alpha$ , to extract an estimate of the time-scale parameter,  $\alpha$ . A best-fit line to this data gives us a charging time scale of  $\alpha \approx 0.38$  with 95% confidence interval bounds of 0.3187 to 0.457. The time-scaling for pure diffusion is  $\alpha = 0.5$ . In light of the uncertainty, the estimated scaling is indicative of a diffusion process.

Figure 4.6c shows the results of integrating the volumetric charging current over time to find the amount of charge stored in each section of the electrode. The effects of non-uniform charging are clearly seen here. Although, the amount of stored charge eventually becomes non-zero everywhere, it increases most rapidly and remains highest near the separator. This is consistent with ions needing to diffuse farther through the electrode to reach unoccupied charge sites and having increased transport losses over the longer distances traveled. We can also see from this figure that the charge stored near the separator reaches about  $8 \text{ C/cm}^3$ , which is much lower than the expected  $41 \text{ C/cm}^3$  charge storage capacity we estimated using the  $Q$  value determined in equation [4.2]. The electrode is not shown to reach full capacity in this figure because only the first 250 s of the data has been plotted. Past this time the error bars

become quite large and we lose confidence in the absolute values of our data. In this time frame, however, it is apparent that only about one-third to one-half of the electrode is being used to store charge over this 250 s period. This means that the electrode should be thinner to fully utilize the electrode in this period of time. However, it should be noted that the 5 mm thickness of high electrode effectiveness is two orders of magnitude thicker than state of the art Li-ion batteries; demonstrating the dramatic increases in thicknesses afforded by aqueous electrolytes.

### **4.3.2 Galvanostatic Discharging**

We performed a second set of experiments on analyzing distributions during galvanostatic discharging at current densities of 225 A/m<sup>2</sup>, 169 A/m<sup>2</sup>, and 112 A/m<sup>2</sup>. By discharging galvanostatically we ensure that the current does not decrease over time and therefore our potential distribution's differential does not become too small, giving us a larger signal to noise ratio over the duration of the experiment. Figure 4.7 shows the potential distribution (a.), the local current (b.), and the volumetric discharging current (c.) in the EDL capacitor during the 225 A/cm<sup>2</sup> discharge. Similarly to the charging data, Figure 4.7b shows that the measured potential distribution does not match the uniform analytical solution near the separator initially, but becomes more uniform over time.

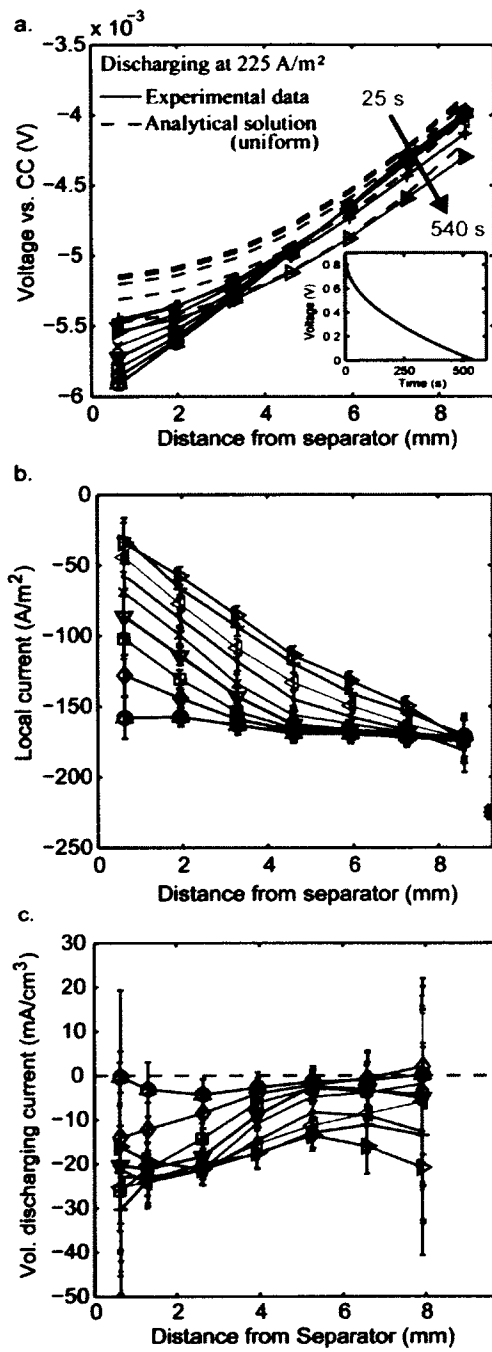


Figure 4.7 Constant current discharging at  $225 \text{ A/m}^2$ . a. Voltage versus the current collector as a function of the distance away from the separator and plotted over time. Deviations of the solid experimental data lines from the dashed uniform charging analytical solution lines suggest non-uniform charging in the electrode. b. Local current plotted as a function of distance through the electrode. Higher currents near the separator suggest most discharging taking place here. c. Volumetric discharging current through the thickness of the electrode. Discharging current is high where local current was low. In all plots:  $\triangle$  - 25 s,  $\circ$  - 35 s,  $\diamond$  - 50 s,  $\square$  - 71 s,  $\nabla$  - 100 s,  $\times$  - 141 s,  $\bullet$  - 200 s,  $\triangleleft$  - 282 s,  $+$  - 398 s,  $\triangleright$  - 537 s.

Figure 4.7a shows unexpected decreases in the voltages as the discharging progresses. Because the current is being held constant, this decrease must be due to a resistance increase in the cell. It is likely that this resistance is occurring between the final tab and the current collector due to the fact that the curve retains its slope at the current collector, but is offset by a constant amount. One possible explanation would be that passivation is occurring at the current collector during operation causing increased resistance. There were no visual indicators of increased resistance, such as corrosion of the current collector or removal of the electrode material. It should be noted that a change in the resistance at the current collector would not affect the current calculations, as they are only dependent on the change in voltage between the sensing layers, which remains constant.

It is also of interest to note that the parasitic reaction that was seen in the charging data does not appear to occur during discharge. Figure 4.7b shows that the current at the tab closest to the current collector remains constant over time. We would expect the



magnitude of this current to decrease over time, if a parasitic reaction was consuming current within the electrode. The fact that a parasitic reaction is observed during charging, but not during discharge suggests that we can be confident that there is no systematic offset in our REs due to our system and that the discrepancy measured is real.

To more clearly see the shift in the volumetric discharging current over time, the data in Figure 4.7c has also been visualized as a spatio-temporal plot in Figure 4.8. In this figure, the volumetric discharge current is shown as a function of the distance through the electrode and time. Darker shades represent little to no volumetric discharge current, while lighter shades indicate higher currents. This figure clearly indicates increased volumetric discharging currents in interior sections of the electrode as time goes on, which are difficult to visualize in the line plots of Figure 4.7c. Additionally, we notice fluctuations in the data that appear to be somewhat correlated across the electrode; i.e., when the current is at a low point of an oscillation the portion of the electrode at the other end exhibits a high point in its oscillation. This is consistent with the constant current discharge where the integral of charging current across the electrode should be constant. Although it is difficult to discern if this is related to noise in the data or the discretization, it could be physical. Additional studies would be required to determine the cause.

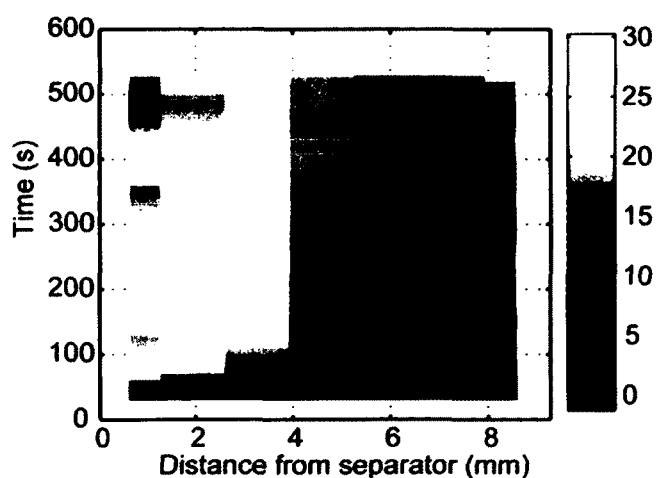


Figure 4.8 Spatio-temporal plot of the volumetric discharging current. Each color represents the amount of discharging current at a given tab and amount of time through the experiment. The majority of the discharging occurs in the half of the electrode closest to the separator.

Potential and local current distributions over time during galvanostatic discharging of the cell at  $169 \text{ A/m}^2$  and  $112 \text{ A/m}^2$  are plotted in Figure 4.9 and Figure 4.10, respectively. One interesting point to note is the uniform, systematic decrease in voltage across the thickness of the electrode at longer times. Since the cell is being held at a constant current and the relative voltage changes between adjacent measurement points are also constant, this voltage drop must be associated with an increase in resistance at the current collector, perhaps due to passivation. Again we note that the parasitic reaction observed in the charging data is absent from the discharging data. Figure 4.9b and Figure 4.10b show the local current behaves as expected, with the current being nearly constant across the electrode at early times, initially depleting only near the separator, and taking on a linear, downward slope at longer times indicating the cell eventually charges more uniformly. The local currents

generally tend towards zero near the separator and remain virtually constant close to the current collector. This evidence suggests to us that when we charge the cell, we are driving a parasitic reaction that is irreversible in the potential window in which we discharge.

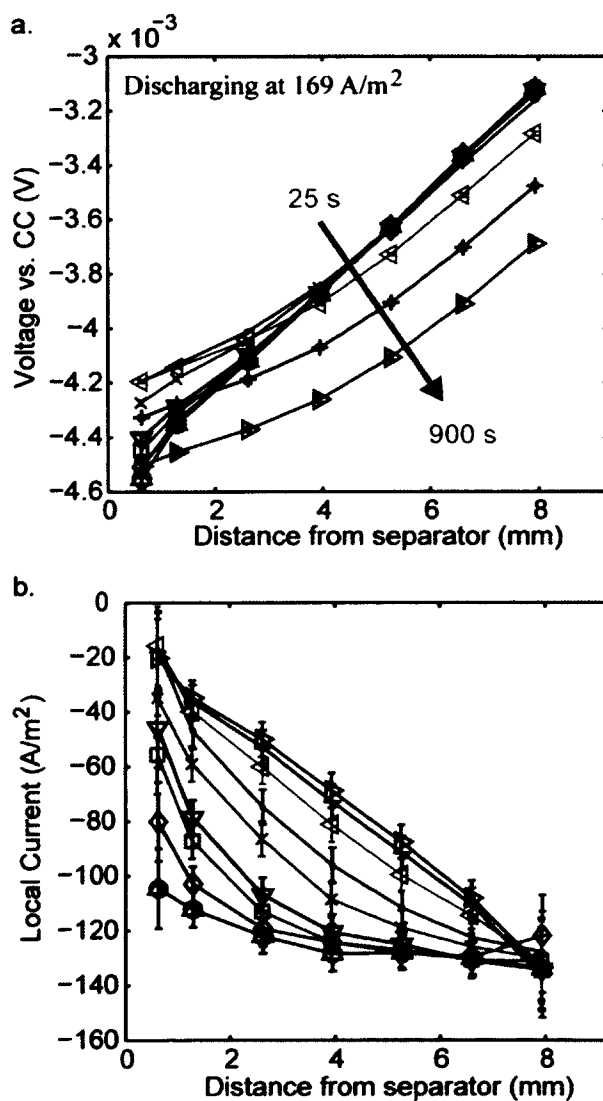


Figure 4.9 Distribution of voltage (a.) and local current (b.) during a constant  $169 \text{ A/m}^2$  discharge of the cell.

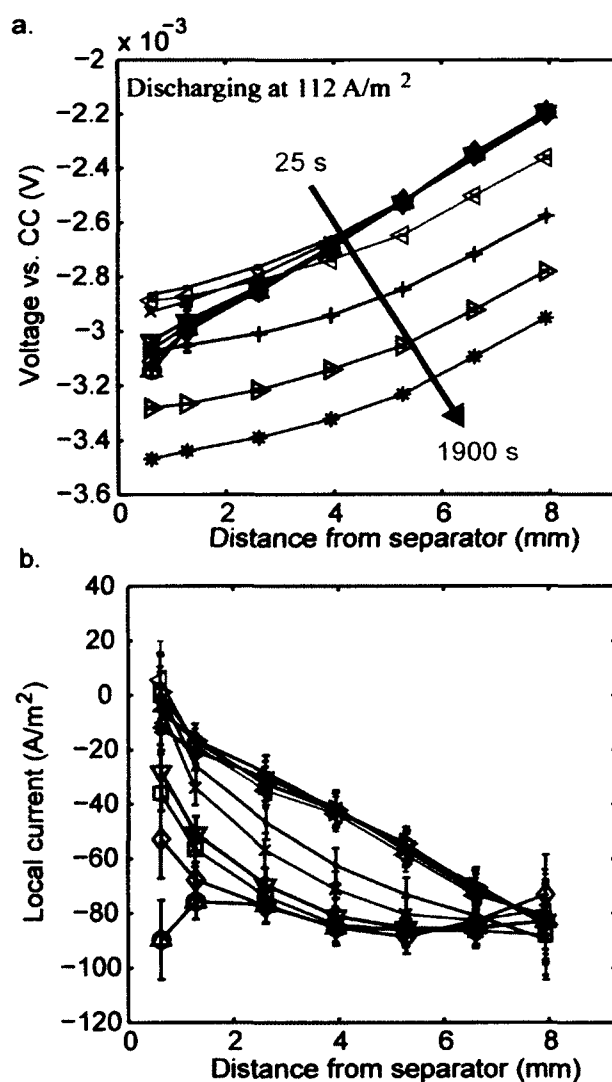


Figure 4.10 Distribution of voltage (a.) and local current (b.) during a constant  $112 \text{ A/m}^2$  discharge of the cell.

## 4.4 Summary

In this chapter, we have presented an ES for making *in situ*, through-thickness electric potential measurements through the negative electrode of an EDL capacitor. Using the ES we were able to obtain local electric conductivity values and some of the first *in situ* potential measurements through the thickness of an uninterrupted, representative

EDL capacitor negative electrode during standard operating conditions. Our results showed that the conductivity was relatively constant through the electrode, but varied with the amount of compression. The potential measurements revealed that the charging was initially concentrated near the separator, but became more uniform over time. We found that, while we were only charging in about half of the electrode during the first ~4 minutes, we were still able to utilize about 5 mm of depth into the electrode. This depth is about two orders of magnitude thicker than current state of the art Li-ion battery electrodes; demonstrating the dramatic increases in thicknesses afforded by aqueous electrolytes. Additionally, we were interested to find evidence of a stray current occurring during the charging cycle, but not during the discharge cycle. The reasons for this are currently unclear and require further investigations.

While the electric ES has provided us with interesting and previously unobtainable data, we believe there are still a number of ways we can improve upon our ES techniques. First, thinner insulating layers could be used. This would allow for more sensing layers in the same thickness and would improve the spatial resolution and therefore the accuracy of the finite difference discretization. Along these lines, sensing layers could be placed closer to the separator and current collector to obtain data points at the ends of the electrode. Second, the conductivity could be measured during the experiments by 1.) performing EIS in parallel with the DAQ to extract a high frequency resistance, or 2.) simultaneously or intermittently measuring conductivity using AC impedance during charging and discharging cycles of the EDL capacitor. This would alleviate issues with possible differences in conductivity

between unpolarized, new electrodes and polarized, conditioned electrodes. Third, we believe there are many advantages to measuring the ionic potential rather than the electric potential. The key advantage would be the larger voltage differences in the ionic potential and a higher signal to noise ratio due to the much lower conductivity of the electrolyte. We did, in fact, move forward with this last point and an ES designed for making ionic potential measurements through the thickness of an EDL capacitor negative electrode is discussed in the next chapter.

## Chapter 5

# An ES for Gathering Ionic Potential Distributions Across a Symmetric EDL Capacitor Electrode

We study a symmetric, aqueous EDL capacitor with implications for aqueous sodium hybrid batteries again in this chapter. However, in this chapter we focus on making *in situ*, through-thickness measurements in the ionic phase of the capacitor as there are many more losses associated with this phase than the electric phase. Because the conductivity in the electrolyte phase is about an order of magnitude smaller than in the electric phase, we will obtain significantly larger potential distributions than in our previous work. The larger potential drops should result in a better signal to noise ratio, which will allow us to do a more in-depth analysis of the results. Once we obtain the distributions, we will again use the finite difference techniques developed in Chapter 3 to calculate the local current, charging current and charge storage distributions. Additionally, we will analyze the effects of charging rate on the temporal evolution of the charge storage distributions and present a method for determining an effectiveness

factor. The results will provide insight into the effectiveness of the electrode and illustrate the transport limitations in thick EDL capacitor electrodes.

## **5.1 Experimental Setup**

The ionic potential sensing ES consists of alternating Nafion sensing and Teflon insulating layers surrounding a 1-D column of working electrode material, which in this case is the negative electrode of a symmetric EDL capacitor. The ionic potential sensing ES was again carefully designed to ensure adequate spacing between the sensing layers and an aspect ratio that allowed for nearly 1-D transport without showing significant edge effects. The Nafion sensing layers created a bit of a challenge, as they needed to remain fully hydrated throughout the experiment and could not be directly accessed by the DAQ leads. We used Hg/Hg<sub>2</sub>SO<sub>4</sub> reference electrodes (REs) for making ionic potential measurements and took additional steps to fully insulate the cell to overcome these issues. This section will detail the full design of the ionic ES, the new hardware and packing of the electrode.

### **5.1.1 Ionic ES Build and Cell Assembly**

Figure 5.1a shows a schematic of the ES we developed for measuring electrolyte potential distributions. The ES that surrounds the cylindrical negative electrode was fabricated using strips of 211 Nafion (Ion Power, New Castle, DE) in sodium-form as sensing layers and 0.793 mm thick sheets of Teflon as insulating layers. Before



assembling the layers, the Nafion was washed in hydrogen peroxide, rinsed in DI water, sodium exchange in 1 M NaOH and rinsed again in DI water. Each treatment lasted for 1 hour and was conducted at 100 °C. The sodium exchanging step replaces  $H^+$  ions bound to the  $SO_3^-$  side chains of the Nafion with  $Na^+$  ions to match the cations of the aqueous  $Na_2SO_4$  electrolyte. The Nafion was then cut into 1 cm by 3.5 cm strips and placed onto sheets of Teflon that had 0.05 mm adhesive sheets (3M 467 MP, St. Paul, MN) bonded to each side. The Nafion strips were arranged such that they radiated from the center of the ES to different positions near the edge of the ES as can be seen from the zoomed in top view of the ES in Figure 5.1b (bottom left). The final thickness of the ES with 7 sensing layers was 6.5 mm. A 1.6 mm diameter hole was drilled in the center of the structure for housing the electrode material and a 6.0 mm diameter hole was drilled at the location of each sensing layer around the edge of the ES for the reference electrodes. A 0.79 mm adhesive sheet was placed on the separator side of the ES to seal the bottom of the 6.0 mm holes and create an electrolyte well for the reference electrodes. A 5.3 mm thick acrylic plate with a matching 1.6 mm hole was prepared to house the positive electrode of the EDLC. It is important to note that although this electrode is thinner than the ES electrode, the cell is not limited by the charge storage of the positive electrode since the transport limitations are so high at the charging rates used. Holes for alignment pins were drilled into both housings to ensure proper lateral alignment of the electrodes in the assembled cell.

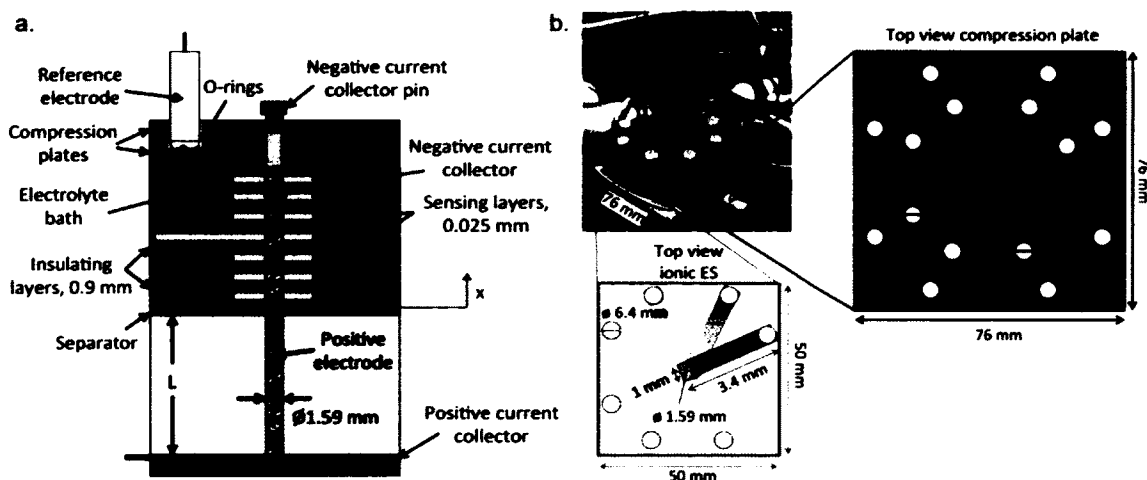


Figure 5.1 a. Schematic of the ionic ES cross-section showing alternating sensing and insulating layers on the negative electrode. An example of an electrolyte filled well and a RE is also shown. b. Photo of the fully assembled ionic ES including Hg/Hg<sub>2</sub>SO<sub>4</sub> reference electrodes (top left). Close up top views of the ionic ES (bottom left) and the top compression plate (right) are also included.

To prepare the electrodes, activated carbon powder (YEC-8 EDLC activated carbon, Fuzhou Yihuan Carbon Co., Fuzhou, China) was mixed with 1 M Na<sub>2</sub>SO<sub>4</sub> (aq). Electrolyte was added until the carbon was thoroughly wetted and the mixture was clay-like, but not overly liquidy. The mixture was packed into holes in the ES and acrylic plate to form the negative and positive electrodes, respectively. The total mass of the activated carbon used for the electrodes was about 0.025 g.

During assembly an electrolyte soaked cotton filter paper separator (Ahlstrom Grade-40, Helsinki, Finland) was placed between the electrodes and seven Hg/Hg<sub>2</sub>SO<sub>4</sub> reference electrodes (BAS Inc., Tokyo, Japan) were secured into position using seated o-rings that also prevented the electrolyte baths from leaking or evaporating. A

0.10 mm strip of stainless steel (TBI, Countryside, IL) was used as a current collector for the positive electrode while a compression pin placed between the electrode and the threaded screw was used for the negative electrode current collector. The fully assembled cell can be seen in Figure 5.1b (top left).

### **5.1.2 Equipment and Testing Procedures**

Once the cell was assembled, a potentiostat (VSP, Bio-Logic, Knoxville, TN) was connected to the cell terminals to control charging and discharging. A data acquisition board (DAQ) (National Instruments, Austin, TX), was attached to both current collectors and all reference electrodes to measure the potential of the cell and each reference electrode with respect to the negative electrode. The input impedance of the differential voltage measurement is specified by the manufacturer as  $>10\text{ G}\Omega$ , yielding negligible stray current through the DAQ. Five cycles of cyclic voltammetry (CV), run at  $0.1\text{ mV/s}$  between  $-0.9\text{ V}$  and  $0.9\text{ V}$ , were used to condition the cell and assess its capacitance. Electrochemical impedance spectroscopy (EIS) was conducted from  $1\text{ MHz}$  to  $30\text{ }\mu\text{Hz}$  with a  $10\text{ mV}$  perturbation. Charging and discharging cycles were run at various constant currents ranging from about  $25$  to  $100\text{ A/m}^2$  and were stopped when the cell voltage reached  $0.7\text{ V}$  during charging or  $0\text{ V}$  during discharge. The cell was held at  $0.7\text{ V}$  for one hour between the charging and discharging cycles to more uniformly charge the electrode and was held at  $0\text{ V}$  for four hours after the discharge cycle to fully discharge the cell before conducting subsequent experiments. Electrolyte potential data was captured by the DAQ from each reference electrode during every experiment.

## 5.2 Preliminary Results

As with the MES and electric ES, CV and EIS were run to condition the ionic ES cell as well to characterize the electrodes by conventional means. Figure 5.2a shows the results of these tests. The CV was conducted at a slow scan rate due to the long time-scale expected for thick electrodes. The results show a well-centered, fairly rectangular plot suggesting relatively low resistances in the electrode at these testing conditions and no apparent parasitic reactions [26, 57]. We were able to calculate the capacitance from the CV data by integrating the area under the forward sweep curve and subtracting the integrated area under the backwards sweep curve. Using this method, we found the cell to have a specific capacitance of about 31 F/g.

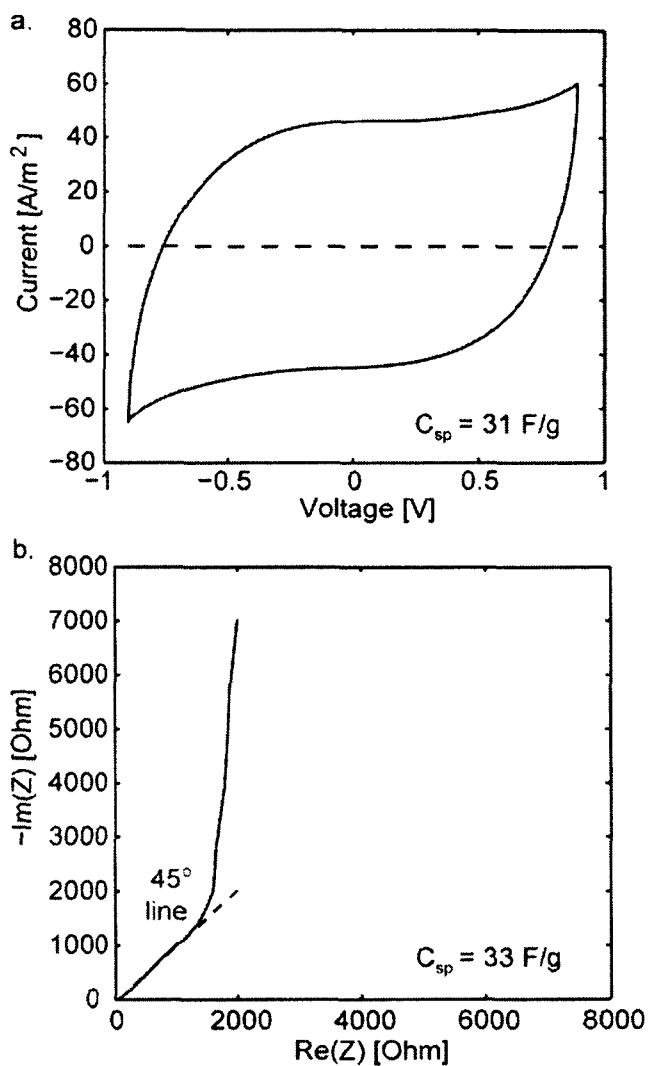


Figure 5.2 a. CV cycled at 0.1 mV/s from -0.9 V to 0.9 V. Integration of the curve leads to a calculated capacitance of 31 F/g. b. EIS conducted from 1 MHz to 30  $\mu\text{Hz}$  with a 10 mV perturbation. The calculated capacitance matches well with the CV data at 33 F/g and the effective conductivity is estimated to be about 1.4 S/m.

We were also able to determine the cell capacitance from the EIS data. Figure 5.2b shows the EIS data where the capacitor again performs as expected with a nearly 45° region at high frequencies followed by a transition into a nearly 90° region at low frequencies. The electrode shows a bounded Warburg response (45° slope) at high

frequencies corresponding to the migration of ions through the electrode, while the vertical region seen at low frequencies is representative of the total capacitance of the electrode [14, 15, 27]. Fitting of the EIS data provides an approximation of the cell capacitance as well as an estimate of the ionic resistance. We fit the data to equation [5.1] using commercial software (Bio-Logic's z-fit software). The software returned approximations for the time constant of the cell,  $\tau = 3666$  s, the electrolyte resistance,  $R_{d1} = R_{e'lyte} = 4548$   $\Omega$  and the separator|electrode interface resistance,  $R_1 = 49$   $\Omega$ . The capacitance,  $C$ , was then calculated to be 33 F/g using the equation  $C = \tau/R_{e'lyte}$ . This value agrees well with the value calculated from the CV data, although it is much lower than what would be expected for this activated carbon material in a thin electrode [54].

$$Z(f) = R_1 + R_{d1} \frac{\coth(\sqrt{\tau_{d1} i 2\pi f})}{\sqrt{\tau_{d1} i 2\pi f}} \quad [5.1]$$

The effective conductivity,  $\sigma_{eff}$ , was calculated using equation [5.2], where  $L$  and  $A$  are the known length and area of the electrode based on the cell design. The resulting  $\sigma_{eff}$  was found to be 1.4 S/m, which as we discuss later, matches well with the conductivity estimated from the ionic ES measurements. Additionally, the high frequency region is nearly an ideal 45° line, making it apparent that the ionic conductivity is relatively constant through the electrode [14].

$$\sigma_{eff} = \frac{L}{R_{electrode}A} \quad [5.2]$$

## 5.3 Ionic ES Results

Ionic potential distribution measurements were obtained from the ES during galvanostatic charging at multiple current densities: 25 A/m<sup>2</sup>, 38 A/m<sup>2</sup>, 50 A/m<sup>2</sup>, 76 A/m<sup>2</sup>, and 101 A/m<sup>2</sup>. The results, which are presented in detail in the following sections, were analyzed using the mathematical methods derived and discussed in Chapter 3 to obtain local current, charging current and volumetric charge stored. This section will also discuss our analysis of the effects of charging rate on the temporal evolution of the charge storage distribution through the electrode and a method for calculating the electrode's effectiveness factor.

### 5.3.1 Galvanostatic Charging

Galvanostatic charging experiments were conducted on the cell at five different current densities, 25 A/m<sup>2</sup>, 38 A/m<sup>2</sup>, 50 A/m<sup>2</sup>, 76 A/m<sup>2</sup>, and 101 A/m<sup>2</sup> using the procedure detailed in the experimental section of this chapter. During each of these tests, the DAQ was used to record the potential of the cell and the potential at each RE, with all measurements being in reference to the negative electrode current collector. Figure 5.3 shows the results from the DAQ at various times during a 76 A/m<sup>2</sup> charging cycle, plotted as a function of the distance away from the separator. In this plot, the solid lines with symbols represent the measurements gathered from the

DAQ. These points were obtained by averaging potential measurements over a 20 s period surrounding the time of interest after the raw data had been smoothed using Gaussian convolution with a standard deviation of 15 s. As expected, the potential drop through the ionic phase of the electrode shown here is more than an order of magnitude larger than the potential drop seen through the electric phase of the electrode in our previous work due to the conductivity difference between the carbon and electrolyte phases [58]. The dashed lines in Figure 5.3 are the simple analytical solution to the current conservation equation, shown in equation [5.3], where uniform charging and constant conductivity are assumed. The boundary conditions used to derive this equation are the same as those used for the PEM fuel cell work in Chapter 2,  $\phi|_{x=0} = \phi_o$  and  $\partial\phi/\partial x|_{x=L} = 0$ , since we are again studying the ionic potential distributions. In this equation  $\phi$  is the potential at a given point through the electrode thickness,  $i$  is the current density of the cell,  $\sigma_{eff}$  is the effective ionic conductivity through the electrode,  $x$  is the distance away from the separator,  $L$  is the total length of the electrode and  $\phi_o$  is the potential at the separator|electrode interface.



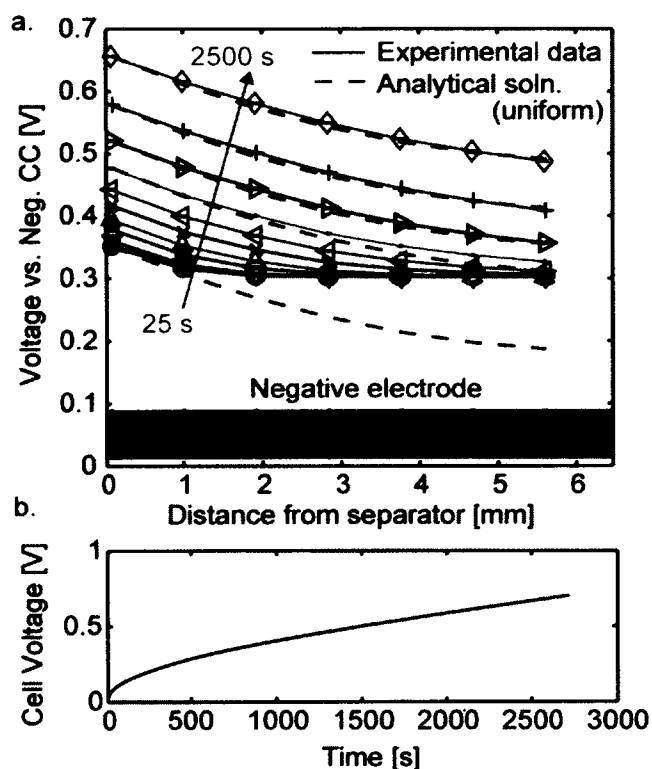


Figure 5.3 a. Distributions of ionic potential (vs. the negative current collector) at 10 logarithmically distributed times during constant current charging at  $76 \text{ A/m}^2$ . The dashed lines are fits to the analytical solution for uniform charging and conductivity. Deviations between the experimental and analytical lines indicate non-uniform charging. The negative electrode inset depicts the orientation of the electrode and location of the sensing layers. Symbols denote the times plotted:  $\circ$  - 25 s,  $\nabla$  - 50 s,  $\square$  - 100 s,  $\triangle$  - 159 s,  $\times$  - 251 s,  $\triangleleft$  - 398 s,  $\bullet$  - 631 s,  $\triangleright$  - 1000 s,  $+$  - 1585 s,  $\diamond$  - 2512 s. b. Raw data of the voltage-time series of the cell during charging.

$$\phi = \frac{i}{\sigma_{eff}} \left[ \frac{x^2}{2L} - x \right] + \phi_o \quad [5.3]$$

From Figure 5.3, it can be seen that as charging begins the measured voltage drop across the electrode does not match up well with the analytical solution. Note that

some of the analytical solution lines were left off the plot for clarity. Disparity between the data lines and the analytical solution is an expected result as this is a simple model that does not describe the spatio-temporal evolution of the electrode charging. The experimental data does not match the analytical solution well until about 17 minutes into the charging cycle, implying that it was not until this point that the cell began to charge uniformly. Because the experimental data and the analytical solution agree well at later times, we were able to use that data to obtain estimates of the effective ionic conductivity. We used MATLAB to fit the experimental data to equation [5.3]. Using  $\sigma_{eff}$  and  $\phi_o$  as fitting parameters, we determined the effective conductivity to be about 1.45 S/m. This value matches well with the estimate of 1.4 S/m we obtained for the conductivity from the EIS data.

We applied the finite difference equations that were developed in Chapter 3 to the ionic potential distribution data that was obtained using the ionic ES. A minor distinction between these current calculations and those developed in Chapter 3 for the electric ES data, is that we assume a uniform conductivity distribution in this case. We previously included a conductivity distribution as these measurements were easily obtained from the carbon electrode phase, but they are more difficult to obtain from the electrolyte phase. The local electrolyte phase current is calculated using finite difference to approximate the first derivative of the potential. The second order accurate forward, backward and central differencing formulas for this calculation are shown in equations [5.4]-[5.6], respectively, to show the slight variation discussed.

$$i_1 = -\sigma \left. \frac{d\phi}{dx} \right|_1 = \frac{-\sigma [-3\phi_1 + 4\phi_2 - \phi_3]}{2\Delta x} + O(\Delta x^2) \quad [5.4]$$

$$i_M = -\sigma \left. \frac{d\phi}{dx} \right|_M = \frac{-\sigma [\phi_{M-2} - 4\phi_{M-1} + 3\phi_M]}{2\Delta x} + O(\Delta x^2) \quad [5.5]$$

$$i_m = -\sigma \left. \frac{d\phi}{dx} \right|_m = \frac{-\sigma [\phi_{m+1} - \phi_{m-1}]}{2\Delta x} + O(\Delta x^2) \quad [5.6]$$

Using these formulas, along with those described by equations [3.14]-[3.16], we computed the spatio-temporal distributions of the local current and local charging current in the electrode during the 76 A/m<sup>2</sup> charging cycle. Figure 5.4a plots the local current at the same instances as the potential was plotted in Figure 5.3a. First, we note that the current at the separator|electrode interface stays near 76 A/m<sup>2</sup> for all times plotted even though the conductivity was not fitted for each time separately. This suggests that the conductivity does not widely fluctuate over time. We were able to additionally support this finding by estimating the temperature change inside the cell during operation, which could potentially have a significant impact on the ionic conductivity. The resistive heating was conservatively estimated to be 0.032 J in the negative electrode. This value was determined from the largest potential drop seen in the data, 0.17 V, the full charging time of 2500 s and half the current used to charge the cell, to account for the current distribution through the electrode, 7.5e-5 A. It was

then assumed that the electrode was perfectly insulated, a worst case scenario, and the sensible heat equation was used to calculate the change in temperature:

$$Q = mC\Delta T \quad [5.7]$$

In this equation  $Q$  is the resistive heating estimated previously,  $m$  is the mass of the electrolyte in the negative electrode,  $C$  is the specific heat capacity of 1 M Na<sub>2</sub>SO<sub>4</sub> [59], and  $\Delta T$  is the change in temperature of the electrolyte during charging. The mass of the electrolyte was determined from the volume of the negative electrode, assuming a porosity of 0.4 and a density of 1009 kg/m<sup>3</sup> [59]. The temperature change was found to be about 1.5 °C. Equation [5.8], was then used to relate the effects of the temperature change on the conductivity of the electrolyte. Here, the activation energy,  $E_a$ , is estimated to be 18,000 J/mol [60], the starting temperature,  $T_{ref}$ , is assumed to be 23 °C and  $R$ , the universal gas constant, is reported as 8.314 J/mol-K. Evaluating the exponential term of this equation allows us to conclude that a 1.5 °C temperature change will have an insignificant effect on the conductivity of the electrolyte, changing it by only about 4%.

$$\sigma = \sigma_{ref} \exp \left[ \frac{-E_a}{R} \left( \frac{1}{T} - \frac{1}{T_{ref}} \right) \right] \quad [5.8]$$

Figure 5.4a clearly shows the non-uniformity of charging, especially at early times. At early times, the local current drops to nearly zero about halfway into the electrode

from the separator side, indicating that there is minimal ion transport past this point. In other words, the ions have been adsorbed onto the carbon surface at empty charge sites in the sections of the electrode closest to the separator, storing charge in these areas, but not further into the electrode near the current collector. As the cell continues to charge, the local current distribution becomes more linear as ions diffuse through the electrode and charge surfaces further away from the separator.

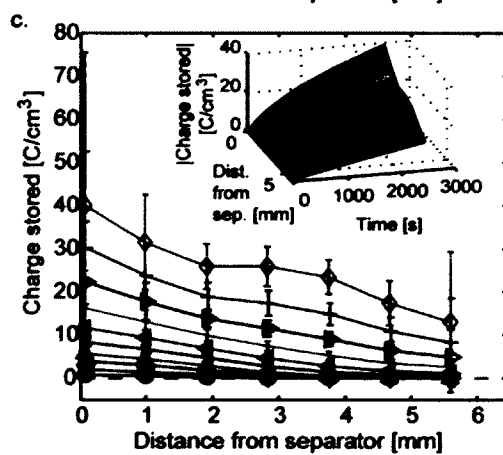
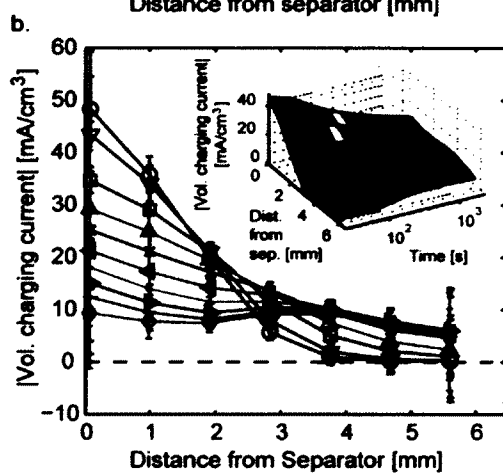
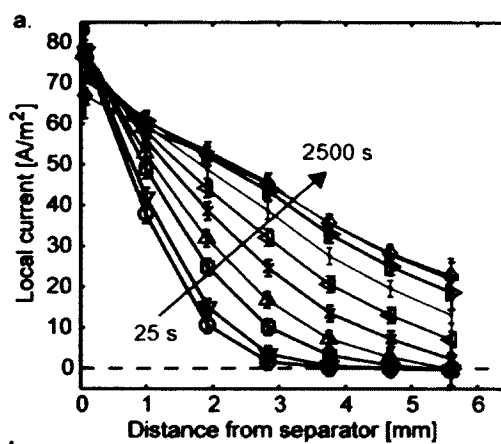


Figure 5.4 Constant current charging at  $76 \text{ A/m}^2$ . a. Local current plotted as a function of the distance away from the separator at 10 logarithmically distributed times. Higher ionic current near the separator initially, indicates charging in this area of the electrode only at these short times. b. The absolute value of the volumetric charging current through the thickness of the electrode is plotted here. Again it is seen that most of the charging current is localized near the separator at short times. At longer times, the charging current begins to level out, suggesting uniform charging at these times. Inset shows volumetric charging current vs. distance away from the separator vs. time. c. Amount of charge stored through the thickness of the electrode. Inset shows charge stored vs. distance away from the separator vs. time. In all plots:  $\circ$  - 25 s,  $\nabla$  - 50 s,  $\square$  - 100 s,  $\triangle$  - 159 s,  $\times$  - 251 s,  $\triangleleft$  - 398 s,  $\bullet$  - 631 s,  $\triangleright$  - 1000 s,  $+$  - 1585 s,  $\diamond$  - 2512 s.

Note the error bars in Figure 5.4a (as well as Figure 5.4b and Figure 5.4c) are based on the uncertainty analysis described in Chapter 3. The key uncertainty variables are the conductivity estimate, the sensing layer spacing, and the voltage measurements. As we discussed previously, the magnitude of the uncertainty error is amplified with each level of finite differencing and the error bars become larger. In addition, due to the derivation of the forward and backward difference formulas, the uncertainty in the data points next to the separator and current collector is notably larger than that for the interior points. It is likely that these error bars are overly conservative. This would be especially true if there are any systematic offsets in the data as these would not affect the shape of the curves and would not influence our conclusions drawn from the data.

As previously mentioned, the volumetric charging current was found by applying standard second order forward, backward and central differencing as detailed in

equations [3.14]-[3.16]. Figure 5.4b plots the absolute magnitude of the volumetric charging current versus the distance away from the separator, at the same 10 logarithmically distributed times as before. The inset shows this data in a 3-D plot where the volumetric charging current has been plotted versus distance away from the separator and time. It is especially clear from the inset that the volumetric charging current is concentrated near the separator at early times, but it begins to level out as we continue to charge the electrode. By 2500 s the volumetric charging current is nearly a horizontal line suggesting that the electrode is charging uniformly throughout at this point.

A key indicator of a charge storage electrode's efficacy is the uniformity of the cumulative charge stored. Knowing the charging current distribution as a function of time, we are able to numerically integrate the charging current with respect to time using the following formula:

$$Q = \int_{t_1}^{t_2} i_c dt \approx \frac{(t_2 - t_1)}{2(T - 1)} \sum_{k=1}^{T-1} (i_{c_{k+1}} + i_{c_k}) \quad [5.9]$$

Figure 5.4c plots the cumulative amount of charge stored in each section of the electrode at discrete instances in time. The inset of Figure 5.4c shows a 3-D plot of the charge stored versus the distance away from the separator and time. The plots show that the amount of charge stored next to the separator is consistently higher than next to the current collector due to the significantly higher charging rates near the separator



at early times. A notable feature evident in the 3D plot is the difference in the functional forms of the charge stored near the separator compared to the charge stored near the current collector, as a function of time. Near the separator, we see a non-linear, decaying increase in the amount of charge stored as the electrode surfaces in that region become fully-charged. In contrast, close to the current collector we observe linearly increasing charge storage as the electrode's charging rate here is limited by transport.

### **5.3.2 Effects of Charging Parameters on Charge Storage Distribution**

The ionic ES allows us to study how the charge storage distribution in the electrode responds to variations in cell operations and electrode preparation. Here, we investigated the effects of charging with different current densities on the temporal evolution of the charge storage distribution. As anticipated, we found the charging rate to have a significant affect on the charge storage distribution and the effective utilization of the electrode. Figure 5.5 shows the charge storage distributions within the electrode when the cell was at a total charge of, a. 50 mC, b. 100 mC and c. 150 mC. Each of these charge states was reached using current densities of  $38 \text{ A/m}^2$ ,  $50 \text{ A/m}^2$ , and  $76 \text{ A/m}^2$ . These current densities correspond to C-rates of  $C/2$ ,  $2C/3$  and  $1C$  that are based on the cell capacitance determined from CV and EIS. Note that the full length of the error bars is not shown, but they are all symmetric.

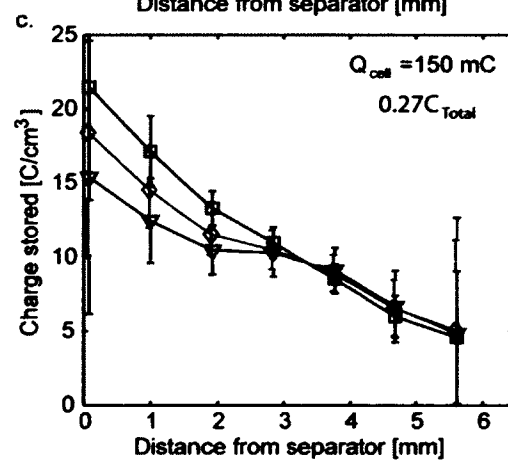
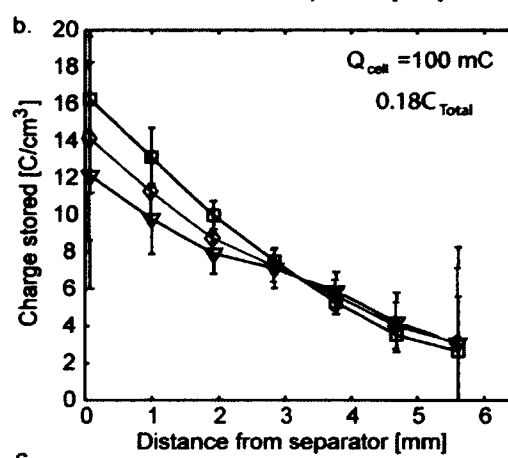
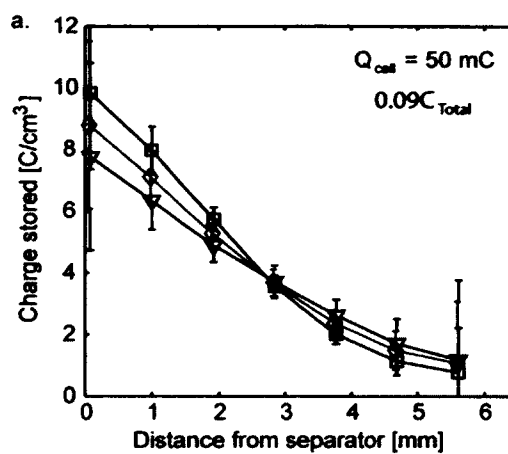


Figure 5.5 Charge distributions for three current densities (absolute values plotted). a. Distributions at a total cell charge for 50 mC. b. Distributions at a total cell charge of 100 mC. c. Distributions at a total cell charge of 150 mC. Larger current densities result in the most non-uniform distributions. All distributions are more uniform at higher amounts of cell charge. Note that the full length of the error bars is not shown, but they are all symmetric. In all cases:  $\nabla$  - 38 A/m<sup>2</sup> (C/2),  $\diamond$  - 50 A/m<sup>2</sup> (2C/3),  $\square$  - 76 A/m<sup>2</sup> (1C).

There are a number of notable trends that can be seen from Figure 5.5. First, as expected, we find that all cases show a significantly higher amount of charge stored near the separator than near the current collector. It can be seen that the uniformity of this charge storage distribution is influenced by the charging rate and duration. Lower current densities and longer charging times lead to more uniform distributions, while higher charging rates and shorter charging durations result in less uniformity. The differences in uniformity are potentially more pronounced than Figure 5.5 depicts due to lower signal from the sensing layers near the current collector. Because the total amount of charge stored is constant for each plot in this figure, the differences between the various current densities on the left-hand side of a given plot should be mirrored in the right-hand side of that plot. This trend is not seen however, likely because the error has a larger impact on the points closer to the current collector as the signal is relatively low at these points.

### 5.3.3 Effectiveness Factor

To see these effects more clearly, we propose an effectiveness factor similar to that applied for porous catalysts [32, 61-64]. The effectiveness factor relates the actual, transport limited charging to the ideal charging in the limit of zero charge transport resistances. In particular, this analysis is directed at the through-plane distribution and does not reflect the local transport resistances in the mesopores. To calculate an effectiveness factor, an estimate of the ideal limit is needed. As the effectiveness factor is normally evaluated in modeling [32, 61-63], it can be straight-forward to achieve this limit (e.g., setting transport resistances to zero or using area-specific kinetic rates and surface area). Herein, we propose a new technique where we use experimental measurements to evaluate the through-plane transport effectiveness factor for charge storage electrodes. Usually, effectiveness factors are computed for steady, heterogeneous reactions. However, for EDLCs and batteries, the effectiveness factor as we define it is a time-dependent (or charge stored dependent) figure of merit.

We calculate the effective factor based on the cumulative charge storage distribution, where the volumetric charge stored near the separator is used to represent that in the limit of infinitely fast transport. Equation [5.10] is used to calculate this effectiveness factor,  $\beta$ , which is the ratio of the average charge stored,  $q_{avg}$ , to the maximum charge stored,  $q_{max}$ . The value for  $q_{avg}$  was found by multiplying the current at which the cell was charged at by the duration of time over which it was charged, while  $q_{max}$  was found to be the point next to the separator in all cases. In this case we are asserting that the electrode is 100 % effective when every section holds as much charge as the

measured maximum. One disadvantage of this figure of merit is that it does not reflect the rate used to achieve this ratio. In other words, a slow charging rate always yields a higher effectiveness factor.

$$\beta = \frac{q_{avg}}{q_{max}} \quad [5.10]$$

Figure 5.6 plots the  $\beta$  values versus the current density (or C-rate) at various states of charge. The general trend of this plot shows that the electrode's effectiveness factor is highest after long times and at low current densities. The highest effectiveness factor calculated was about 75 %, which was obtained after the longest charging period, using the lowest current density. It appears there is an inverse trend between the effectiveness factor and current density. However, it is important to note that the effectiveness factor will asymptote to 100% as the current density goes to zero. Similarly, the effectiveness factor should asymptote to zero as the current density increases to infinity.

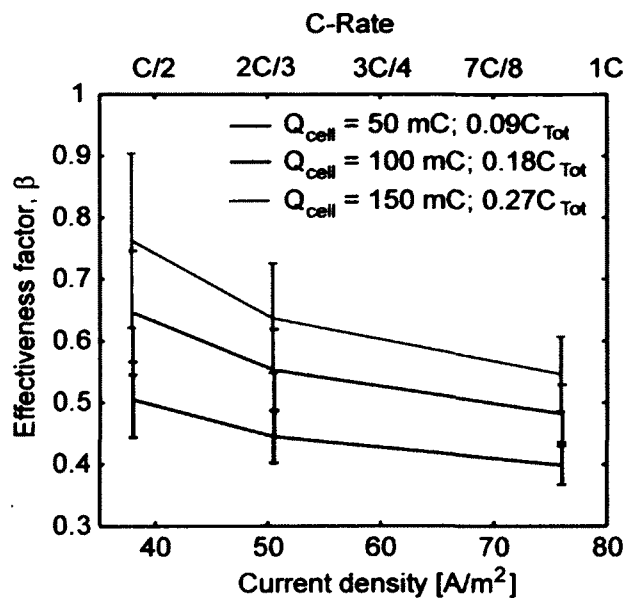


Figure 5.6 Effectiveness factor,  $\beta$ , as a function of current density at three levels of charge stored.

One of the potential ways to interpret Figure 5.6 is from the perspective of the charging and discharging rates for a given application. The plot quantifies the decrease in active material utilization that happens as higher charging/discharging time-scales are encountered; as would perhaps occur with highly intermittent, renewable power generation systems. The plots can then provide guidance on how to optimize electrode thickness for a given application. Future work on this should explore the rate dependency of these plots and identify scaling factors that collapse these figures and provide a rate independent figure of merit.

## 5.4 Summary

In this chapter, we discussed a method for measuring the ionic potential through the thickness of the negative electrode in a symmetric, aqueous EDL capacitor. We chose to study the negative electrode of a symmetric EDL capacitor for simplicity, but our ultimate goal is to improve transport through the negative electrode of an aqueous sodium hybrid battery. Our ionic ES was able to gather ionic potential measurements at seven points through the thickness of the electrode. We used the data collected from each sensing layer to calculate the local current, local volumetric charging current and local charge storage through the electrode at various current densities. We found there to be non-uniform charging in the electrode in all cases with certain conditions, such as increased current density, exacerbating the non-uniformity. We were additionally able to use this data to study the effects of various charging parameters on the charge storage distribution and link this to how effectively the electrode material is being used. In the best-case scenario, when the electrode was charged at low rates for long times, we charged only about 75 % of the electrode and this number decreased as the charging rate increased. Since many applications may require higher charging rates, these results dictate a need for improved through-plane transport to more effectively charge/discharge thick electrodes.

We saw a great improvement in our results when we studied the ionic potential rather than the electric potential, but there are still a number of changes to consider for future iterations that could continue to improve the results. First, as was discussed in the optimal layer spacing section of Chapter 3, there may be benefits to increasing the

spatial resolution of the ES, especially at the end points. Non-uniform sensing layer spacing should be considered to allow for higher resolution near the error plagued end points even if equipment limitations would not allow for such high resolution through the entire electrode. Second, finding a method for measuring the local conductivity using the sensing layers would improve the accuracy of our finite difference calculations and would be imperative for analyzing macro-scale structured electrodes such as those mentioned in the appendices. This type of electrode structuring may intentionally lead to non-uniform conductivity through the electrode so measurements of the local conductivity would be critical for analyzing the results and determining the effectiveness of the electrode structuring. One final idea would be to integrate electric sensing layers into the ionic ES. This would allow for both the electric and ionic potential distributions to be obtained simultaneously and give us the opportunity to compare them to verify the accuracy of our data. All of these changes should be considered for future work using the ionic ES.



## **Chapter 6**

# **Conclusions, Contributions and Recommendations for Future Work**

### **6.1 Conclusions and Contributions**

A novel method for obtaining through-thickness distributions measurements in porous electrodes was developed and presented in this dissertation. We designed and implemented our MES device to make ionic potential distribution measurements in the cathode catalyst layer of a PEM fuel cell. Two variations of our ES were used to measure electric potential distributions and then ionic potential distributions in the negative electrode of an aqueous sodium EDL capacitor. We used the data gathered to more fully characterize the electrodes through calculating conductivity, current, charging current and charge storage distributions. The following subsections summarize the developments and findings of this research.

### **6.1.1 MES Applied to the Cathode Catalyst Layer of a PEM Fuel Cell**

1. An MES was designed and implemented to measure the ionic potential distribution through the thickness of the cathode catalyst layer in a PEM fuel cell. The MES consisted of alternating Kapton insulating and Nafion sensing layers that surrounded a 1-D column of working electrode. These were, to the best of our knowledge, the first potential distribution measurements made through the thickness of an uninterrupted, representative PEM fuel cell electrode under normal operating conditions.
2. We found that the MES could easily distinguish between various operating conditions. When the cell was flooded, the potential distribution across the catalyst layer was linear, however, when the cell was drier, the distribution matched the analytical solution to the current conservation equation. The shape of the distribution curves allowed us to infer where in the electrode the reactions were taking place. For example, in the flooded case, the reactions appeared to all be taking place near the GDL and much of the electrode was not being used, while the distribution of the drier case suggested that the electrode was being used nearly uniformly under these conditions.
3. Data from the MES allowed us to make direct estimations of the conductivity through the electrode. The potential distribution data was fit using MATLAB and revealed surprisingly high conductivity values. We found that our conductivity estimate matched up well with some recent studies and suggests

that there are some unknown mechanisms creating higher than expected ionic conductivity through the catalyst layer. While we speculated on the causes, more work needs to be completed to determine the exact mechanism causing the high conductivity values.

### **6.1.2 Mathematical Methods Used to Assess Electric and Ionic Potential Distribution Methods in Aqueous Sodium EDL Capacitors**

1. This chapter developed a mathematical method for calculating local current, charging current and charge storage distributions from measured electric and ionic potential distributions. Second order forward, backward and central difference equations were used for finding local current and charging current. Where applicable, this method took into account varying conductivity through the electrode. A time integration of the charging current was used to determine the charge storage distribution.
2. An error analysis was performed using error propagation. This allowed us to calculate and plot error bars for all of our distributions based on the uncertainty of the equipment. We found that the error in our potential measurements and our local current calculations was reasonable, but it increased significantly as it was propagated through the second finite difference calculation and time integration. This turned out to be a bit of a hindrance for analyzing the electric ES measurements, but was mitigated by the larger potential drops associated with the ionic ES measurements.

3. The error sensitivity of the local current and charging current calculations was assessed. It was determined that the central difference calculations are quite robust, but that the forward and backward differences were fairly sensitive to uncertainty error. The forward difference is especially sensitive to the conductivity as there is a large potential drop near the separator making it susceptible to changes in the slope.
4. Ionic ES potential distribution data was used to assess the effects of sensing layer spacing on the total system error. MATLAB was used to fit the potential distribution data and obtain a continuous polynomial to use for estimating the error on local currents and charging currents calculated with various numbers of sensing layers. Both the equipment uncertainty error and the truncation error for these calculations were determined and used to indicate the sensing layer spacing that resulted in the lowest error. The results suggested that a layer spacing of about 0.92 mm was ideal. This spacing is what was used in the ionic ES experiments, which implies that adjusting the layer spacing is not a guaranteed method for reducing our measurement error.

### **6.1.3 ES Used to Make Electrical Potential Distribution Measurements in an Aqueous Sodium EDL Capacitor**

1. An ES was developed and implemented to measure electric potential distributions through the thickness of the negative electrode of a symmetric aqueous sodium EDL capacitor. The ES was comprised of alternating Teflon

insulating and stainless steel sensing layers surrounding a 1-D column of negative electrode material. The ES analysis presented in this dissertation was, to the best of our knowledge, the first set of quantitative, *in situ* distribution measurements of electric potential, current, charging current, and charge stored in a continuous battery or EDL capacitor electrode.

2. Local conductivity measurements were obtained directly in two different electrode configurations through the use of the electric ES. These measurements were factored into our finite difference calculations and allowed us to more accurately calculate the local current and charging current. This was, to the best of our knowledge, the first known instance of this type of through-thickness resistance measurement made in a representative porous electrode.
3. Local currents, charging currents and charge storage distributions were calculated and plotted from the electric potential data using the methods from Chapter 3. The results clearly showed how charging began non-uniformly near the separator and moved through the electrode over time. The charge storage distribution remained skewed towards the separator even at longer times because of the ease at which charging takes place at short transport length scales.
4. We determined that only about 5 mm of the 1 cm electrode was being charged during early charging times. Despite this, a 5 mm charging depth is still about two orders of magnitude larger than the charging depth of current state of the

art Li-ion battery electrodes and illustrates the dramatic increases in thicknesses afforded by aqueous electrolytes.

#### **6.1.4 ES Used to Make Ionic Potential Distribution Measurements in an Aqueous Sodium EDL Capacitor**

1. An ES was developed and implemented to measure ionic potential distributions through the thickness of the negative electrode of a symmetric aqueous sodium EDL capacitor. The ES was comprised of alternating Teflon insulating and sodium exchanged Nafion sensing layers surrounding a 1-D column of negative electrode material. To the best of our knowledge, this was the first set of quantitative, *in situ* distribution measurements of ionic potential, current, charging current, and charge stored in a continuous battery or EDL capacitor electrode.
2. Local currents, charging currents and charge storage distributions were calculated and plotted from the ionic potential data using the methods from Chapter 3. The larger potential drops associated with studying the ionic potential meant our results were more reliable and that we could examine the data further in time through the charging/discharging cycles. The results clearly showed how charging began non-uniformly near the separator and moved through the electrode over time. The charge storage distribution remained skewed towards the separator even at longer times because of the ease at which charging takes place at short transport length scales.

3. The ionic potential distribution data allowed us to directly estimate the effective conductivity in the electrode. MATLAB was used to obtain a fit to the ionic potential data using the separator|electrode interfacial potential and the conductivity as fitting parameters. The conductivity was estimated to be around 1.45 S/m, which matched well with the conductivity estimated from conducting EIS on the cell.
4. The charge storage distributions were used to estimate what percentage of the electrode was being utilized during the charging cycle. We found that at low charging rates and long times, we only used up to about 75 % of the electrode material. While this electrode again demonstrated charge depths that were orders of magnitude longer than for current state of the art Li-ion battery electrodes, these results clearly show the need for improved through-plane transport to more effectively charge/discharge the electrode.

## **6.2 Recommendations for Future Work**

### **6.2.1 MES Applied to PEM Fuel Cells**

1. The biggest obstacle to using the MES on a PEM fuel cell cathode catalyst layer was the hardware. The hardware should be redesigned such that all gases flow internally through the temperature controlled hardware. With the current design gases flow through tubes that exit and reenter the hardware. This resulted in high levels of condensation, leading to the formation of water

droplets that adversely affected the accuracy and stability of the results. It also limited the conditions under which the cell could be run. Redesigning the hardware such that all lines are completely insulated and temperature controlled would alleviate these issues. Another member of the lab has taken these issues into consideration and has redesigned and implemented new hardware that has successfully solved these problems.

2. During the hardware redesign, access to the HRE measurement points should also be reconsidered. The current design is cumbersome and requires many delicate connections. This could be improved through the use of a printed circuit board, for example. This issue has also been looked into by the lab member continuing this work and a printed circuit board has been successfully implemented to access the HREs.
3. Developing a method for measuring the local conductivity is also important. This may be possible through the use of the 4-wire sensing mode on a sourcemeter for example. Local conductivity values would provide additional information about the electrode and may lead to methods for improving performance through electrode structuring. Additionally, it may help to elucidate mechanisms that may be enhancing the through-thickness conductivity.



## **6.2.2 Electric ES Applied to EDL Capacitors**

1. Optimizing the sensing layer spacing and perhaps using thinner sensing layers to maximize the spatial resolution of the ES may improve the results from this device. Additionally, adding sensing layers at the separator and current collector would provide more data in sensitive areas and would improve the reliability and accuracy of our results.
2. Obtaining resistance measurements during operation would alleviate issues with possible differences in conductivity between unpolarized, new electrodes and polarized conditioned electrodes. This could be accomplished by 1.) performing EIS in parallel with the DAQ to extract a high frequency resistance, or 2.) simultaneously or intermittently measuring conductivity using AC impedance during charging and discharging cycles of the EDL capacitor.

## **6.2.3 Ionic ES Applied to EDL Capacitors.**

1. Developing a method for measuring local conductivity would also improve the accuracy of our finite difference calculations and would provide valuable information for developing new electrodes. The Hg/Hg<sub>2</sub>SO<sub>4</sub> REs used in this work may not be suitable for obtaining these measurements. This may require modifying the ionic ES hardware to work with HREs as these would allow us to implement 4-wire sensing to measure the conductivity.
2. Creating a higher resolution ionic ES may still be beneficial. Our optimal spacing calculations do not suggest a guaranteed decrease in error with an

increase in the number of sensing layers. However, this does not take in to consideration the possible occurrence of a systematic offset in the DAQ measurements. While an offset would affect the overall accuracy of the measurements, it would not affect the relative accuracy between sensing layers and we may find that our equipment error is smaller than expected. If this were the case, the optimal layer spacing may be decreased. Tests should be conducted to assess the accuracy of the DAQ. Additionally, a non-uniform layer spacing could also be tested and may help the believability of the error plagued end points.

3. It may be beneficial to integrate electric sensing layers into the ionic ES. This would allow for both the electric and ionic potential distributions to be obtained simultaneously and give us the opportunity to compare them to verify the precision of our data. It may also provide insights into developing new macro-structured electrodes.

## Appendix A

# Nafion Supported EDL Capacitor Electrodes

A number of experiments were conducted to assess the effects of using Nafion as the electrolyte in EDL capacitor electrodes. We were interested to see if Nafion could be used to improve the robustness of ion transport through the electrode and therefore improve the overall cell performance. Improvements have been seen in other studies when Nafion was used as the electrolyte in some battery and supercapacitor electrodes [27, 65, 66]. However, it is important to note that these studies all showed improvements over using organic electrolytes, which typically have significantly lower conductivities than aqueous electrolytes.

Before fabricating the electrodes, the Nafion had to be sodium exchanged. Nafion is a cation exchange material that will block the transport of anions and facilitate the transport of positively charged cations that are charge balanced by  $SO_3^-$  groups on the side chains. It is normally sold in protonated form, but the  $H^+$  ions can easily be exchanged for  $Na^+$  ions as is required for operating the aqueous sodium EDL capacitor used in this study. We used the electrode preparation work done by Garsuch et al. [66] as a guide for the exchange procedure. Similarly to their work, we conducted a titration test of Nafion with NaOH to ensure that we used the correct amount of NaOH to fully exchange the Nafion. The results are shown in the titration curve in

Figure A.1. We found that adding 1.3 mL of 0.1 M NaOH to 2 mL of a 5 wt % Nafion solution gave us a 1.5:1 molar ratio of Na:H, a high enough ratio to ensure that the Nafion was completely sodium exchanged. During this procedure the Nafion was diluted with the NaOH such that the final solution was only 2.9 wt % Nafion solids. This was taken into account when mixing the exchanged Nafion solution with activated carbon to make the electrode material.

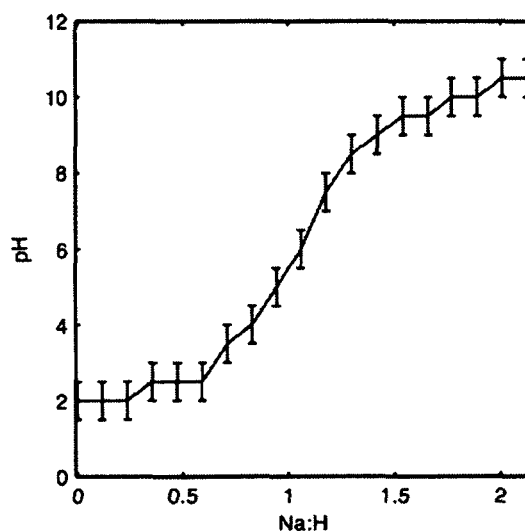


Figure A.1 Titration curve showing the pH of the Nafion solution as sodium hydroxide is added to the solution. The x-axis is the ratio of moles of sodium added to the moles of hydrogen that started in the solution.

The electrodes were then fabricated using methods similar to those discussed in Chapter 4 and Chapter 5. However, before mixing the activated carbon with the electrolyte, it was mixed with the sodium exchanged Nafion solution and ultrasonicated for 30 minutes. The Nafion/activated carbon mixture was dried in an oven at 70 °C for about 2 hours and then annealed under vacuum at 120 °C for 1 hour

and 160 °C for 20 minutes. Activated carbon and Nafion were mixed such that the resulting electrode material would be either 5 wt % or 10 wt % Nafion solids and 95 wt % or 90 wt % activated carbon, respectively. The activated carbon/Nafion material was then mixed with the Na<sub>2</sub>SO<sub>4</sub> electrolyte as before and packed into acrylic housings. Both types of electrodes were tested using CV at multiple scan rates to assess the impact of the Nafion. Typical CV curve responses from these tests are shown in Figure A.2. The results of CVs conducted on a baseline electrode (no Nafion), electrodes with 5 wt % Nafion and electrodes with 10 wt % Nafion are shown in Table A.1.

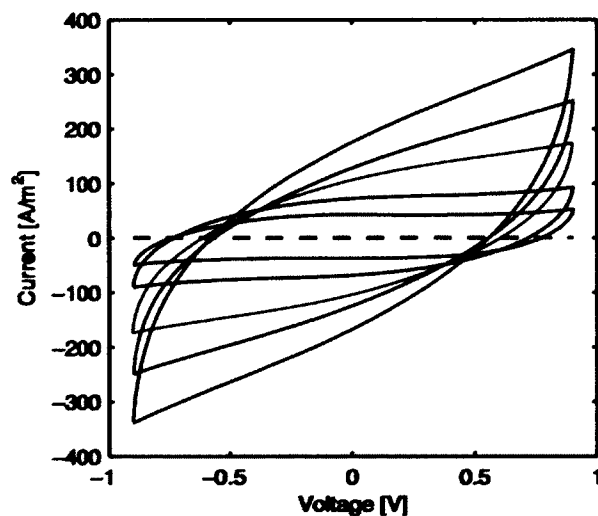


Figure A.2 Typical CV curves for a Nafion electrode. In this case a 5 wt % Nafion electrode was used. The scan rates used were 0.1 mV/s (blue), 0.2 mV/s (black), 0.5 mV/s (red), 1 mV/s (green) and 2 mV/s (purple).

Table A.1 The results of CV scans conducted at multiple different scan rates on electrodes with varying amounts of Nafion in the electrode material.

Scan Rate [mV/s]	Baseline test (no Nafion)		Nafion electrode [5 wt%]		Nafion electrode [10 wt%]	
	Capacitance [F/g <sub>AC</sub> ]	Percent decrease [%]	Capacitance [F/g <sub>AC</sub> ]	Percent decrease [%]	Capacitance [F/g <sub>AC</sub> ]	Percent decrease [%]
0.1	28.0	--	26.1	--	25.75	--
0.2	23.1	17.50	22.45	13.98	21.35	17.09
0.5	15.3	33.77	14.1	37.19	12.5	41.45
1	9.6	37.25	8.8	37.59	7.5	40.00
2	6.1	36.46	5.8	34.09	4.95	34.00

The results show the specific capacitance of each electrode at various CV scan rates as well as the percent decrease in total capacitance as the scan rate is increased. We hypothesized that the Nafion would improve the robustness of the ion transport by ensuring that areas of the electrode did not become ion depleted. We expected, therefore, that the capacitance of the Nafion electrodes would decrease less than the capacitance of an electrode without Nafion as the scan rate was increased. Unfortunately, we did not observe this trend. While we had hoped to see some improvement, the unvarying results are not surprising as Nafion has a similar bulk conductivity to 1 M aqueous sodium sulfate.

The results of these experiments were not 100 percent conclusive. If these experiments are repeated in the future there are a few changes that should be considered. Even though the electrode material appeared to be well-mixed, one recommendation would be to add a small amount of Triton X to ensure that the Nafion is dispersed evenly over the activated carbon. Another would be to develop a more accurate technique for

massing the electrode material used in the cell. We were not able to measure the amount of activated carbon packed into the electrode housing during the packing process so these measurements had to be made post-mortem. However, it was also difficult to remove the material from the housings in order to properly dry the material for weighing. Additionally, the humidity in the lab affected how well we were able to dry the electrode. On that note, a final recommendation would be to redesign the cell hardware such that the cell could be submersed in electrolyte during testing or to determine a better method for sealing the cell, perhaps by using a pouch cell setup. The low humidity of the lab space in the winter tended to dry out the electrodes. If the dry out was quick enough, it may have affected the final results. Even if these tests do not get repeated, it appears as though adding Nafion does not have a significant negative impact on the performance, which may be useful to know in the future.

## Appendix B

# Macro-structuring EDL Capacitor Electrodes for Improved Through-Plane Transport

There have been a number of studies focused on micro-structuring electrode material to improve performance by, for example, controlling the pore size distribution or by altering the carbon surface area [67-70]. However, there has not been much consideration given to macro-structuring the electrode, which we believe could be beneficial to cell performance as well. One group, Okura et al. [71] has seen some performance improvement by creating through-plane microchannels in their EDL capacitor electrodes. We believe that adding this type of ion “highway” through the thickness of the electrode would be beneficial to the electrode performance. The ion transport in bulk electrolyte is nearly 10 times higher than the transport through the porous electrode material. This suggests that adding a pathway of bulk electrolyte should allow ions to travel through the thickness of the electrode much more quickly and charge/discharge through the electrode thickness faster and more uniformly.

We tested this theory by comparing the performance of a standard electrode to a similar electrode with a single hole drilled part way through its thickness and filled with electrolyte. Before conducting experiments, we calculated the expected change in performance. The schematic in Figure B.1 shows holes drilled into an electrode and



denotes the relevant length scales. Note that the schematic shows two holes, however this study only considered the use of one hole.  $L_e$  is the full thickness of the electrode,  $L_h$  is the depth of the hole,  $r_e$  is the radius of the electrode,  $r_h$  is the radius of the hole and  $\delta$  is the charging depth. We assume that the ion transport through the electrolyte filled hole is sufficiently fast such that the charging depth is a uniform distance into the porous electrode material from every surface. The active electrode volume can then be calculated for various hole lengths and charging depths using simple geometry as shown in equation [B.1]. It is important to note that the active volume cannot exceed the bounds of the electrode material. Therefore, if the length of the hole plus the charging depth would exceed the length of the electrode then,  $(L_h + \delta)$  would become  $L_e$ . Similarly, if the radius of the hole plus the charging depth became larger than the radius of the electrode then,  $(r_h + \delta)$  would become  $r_e$ .

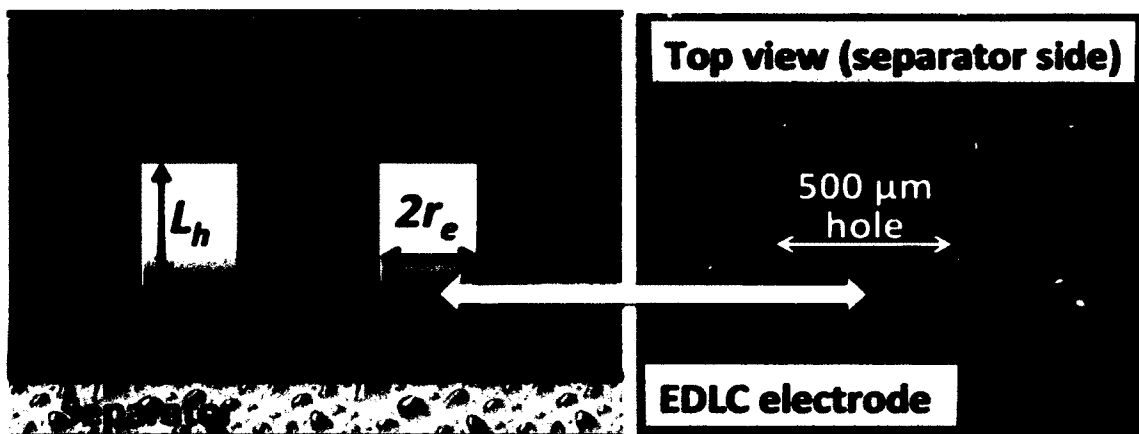


Figure B.1 Macro-structuring an electrode by adding through-thickness holes. The left side shows a schematic of a side view of an electrode with holes drilled into it and the relevant length scales that influence charging. It is assumed that the ion transport through the electrolyte filled hole is sufficiently fast such that the charging depth would be a uniform distance into the electrode from every surface. An image of an electrode with a  $500 \mu\text{m}$  hole is shown on the right. The hole remained visibly unchanged after testing.

$$V_{active, hole} = [\pi r_e^2 \delta - \pi r_h^2 \delta] + [\pi (r_h + \delta)^2 (L_h + \delta)] - \pi r_h^2 L_h \quad [\text{B.1}]$$

To estimate the performance change that we could expect to see, we calculated  $V_{active, hole}$  using equation [B.1] along with the dimensions of our experimental setup and compared that to the active volume for an electrode with no hole;  $V_{active, no hole} = \pi r_e^2 \delta$ . In this case, we used an electrode with a 1.6 mm diameter that was 5.3 mm thick and used a  $500 \mu\text{m}$  diameter drill bit when necessary to drill out a hole. We let the depth of charge and the depth of the hole vary parametrically and plotted the results, which can be seen in Figure B.2. It can easily be seen from this plot that the hole has the largest impact when it goes through the entire electrode thickness and

the charging depth is shallow. It is unlikely that these conditions would persist through the entire charging cycle, however, as the charging depth would increase as the cell continues to charge. However, there are still notable differences that could have a significant impact on how the electrode is charged. In our experiments we consider a hole drilled about half way through the thickness of the electrode. At this length, if the charging depth is about 2-3 mm, we can still expect to have about 1.7-2.1 times the amount of active material in the electrode with the hole as compared to the electrode without the hole. Therefore, we should see close to a two-fold increase in performance when testing a cell with a 500  $\mu\text{m}$  hole drilled halfway into the electrode.

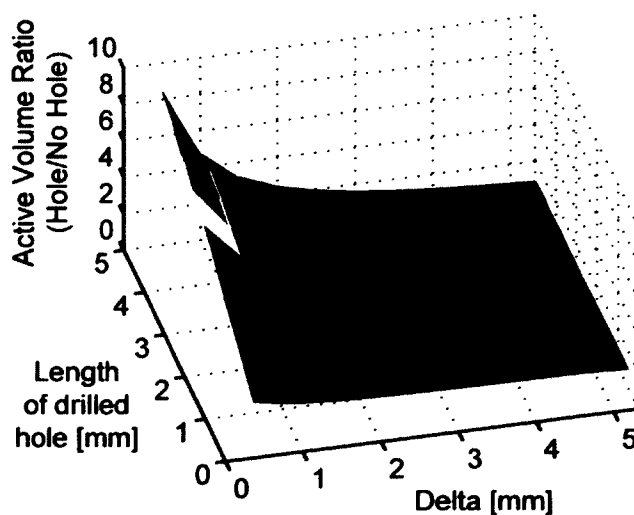


Figure B.2 The active volume ratio between an electrode with a 500  $\mu\text{m}$  hole and a similar electrode with no hole is plotted. The depth of the hole and the depth of charging were varied parametrically to assess the effects on the active volume ratio.

Electrodes were fabricated using similar methods to those discussed in Chapter 4 and Chapter 5. However, these electrodes contained 10 wt % Teflon-FEP (DuPont, Willmington, DE) and 1 wt % Triton X (Sigma-Aldrich, Saint Louis, MO). The Teflon-FEP was included as a binder so the electrode material would hold its shape even when the hole was drilled into it and the Triton X was used to evenly disperse the Teflon-FEP with the activated carbon material. The Teflon-FEP and Triton X were mixed together first and ultrasonicated for about 10 minutes. Then the solution was mixed with the activated carbon and ultrasonicated for about 30 minutes. The material was left overnight to dry before being mixed with  $\text{Na}_2\text{SO}_4$  (aq) and packed into acrylic housings as in previous experiments. Once the electrodes were packed, a current collector was attached to one end and a micromill was used to drill a 500  $\mu\text{m}$  hole into the middle of the other end about halfway through the electrode's thickness. The top of the electrode was then scraped with a sharp blade to remove any material that mounded up near the hole during drilling. The electrodes were soaked with electrolyte before being placed together with an electrolyte soaked separator between them. The cell hardware was assembled and tightened, and tape was placed around the seam between the electrode housings. Parafilm wax was then wrapped around the entire cell hardware to delay dry out as much as possible.

CV was conducted on the cells at multiple different scan rates; 0.1 mV/s, 0.2 mV/s, 0.5 mV/s, 1 mV/s and 2 mV/s. This was followed immediately by EIS, which was conducted between 1 MHz and 100  $\mu\text{Hz}$  with 10 mV perturbations. The CV data and the mass of activated carbon in the electrode was used to calculate the capacitance of

every electrode at each scan rate. An equivalent circuit curve was fit to the EIS data using Bio-Logic's zfit software, which allowed us to calculate the capacitance using a second method and to obtain a resistance measurement for each electrode. The results of these experiments for the electrodes with and without a hole are shown in Table B.1 and Table B.2 respectively.

Table B.1 Results from CV and EIS run on cells using electrodes with 89 wt % activated carbon, 10 wt % FEP and 1 wt % Triton X. A single 500  $\mu\text{m}$  diameter hole was drilled halfway through the thickness of both electrodes in these tests.

	<b>Hole Electrode 1</b>	<b>Hole Electrode 2</b>	<b>Hole Electrode 3</b>	<b>Hole Electrode 4</b>
<b>Mass AC [g]</b>	0.0119	0.0131	0.013	0.0135
<b>Specific Capacitance from CV [C/g<sub>AC</sub>]</b>	47.2	36.7	34.6	33.2
	40.2	33.2	31.8	30.9
	25.9	24.5	24	22.8
	15.6	16.1	15.5	14.6
	9.8	9.6	9.1	8.8
<b>Specific Capacitance from EIS [C/g<sub>AC</sub>]</b>	53.3	34.6	34.6	31.9
<b>R1 [Ohms]</b>	91	77	75	70

Table B.2 Results from CV and EIS run on cells using electrodes with 89 wt % activated carbon, 10 wt % FEP and 1 wt % Triton X. These standard electrodes did not have holes drilled into them.

	<b>No Hole Electrode 1</b>	<b>No Hole Electrode 2</b>	<b>No Hole Electrode 3</b>
<b>Mass AC [g]</b>	0.0149 g	0.0155 g	0.0145 g
<b>Specific Capacitance from CV [C/g<sub>AC</sub>]</b>	37.2	33.1	36.4
	33.8	31	33.4
	23.9	23.9	25.5
	15.5	16	16.8
	9.8	9.7	10.3
<b>Specific Capacitance from EIS [C/g<sub>AC</sub>]</b>	39.4	32.5	35.6
<b>R1 [Ohms]</b>	48	42	43

These results are somewhat inconclusive. In some cases an electrode with a hole appears to outperform an electrode without a hole, but other times the electrode without the hole appears to perform better. There are a few possible reasons that might cause us to see this unexpected result. The most important is probably the inaccuracy of measuring the mass of the activated carbon. Only about 5 % of the volume of the electrode material is removed when the hole is drilled out, which corresponds to a relatively small difference in mass between the two types of electrodes. Unfortunately, it is difficult to thoroughly dry out and weigh the electrode without losing some amount of material. Additionally, the material appears to absorb some moisture from the air so the relative humidity of the room in which the material is being massed has

an effect and small inaccuracies in the mass can have relatively large effects on the specific capacitance calculated. Another possible issue could be if the drilled out hole in the electrode was not completely filled with electrolyte, which could happen if electrolyte was wicked away when the cell was put together or because it dried out in this area before the experiments were completed. There is some evidence that this is happening as we can see by the relatively high EIS resistance measurements gathered from the electrodes with holes compared to the electrodes without holes. This high resistance would likely hinder the performance of the cell.

A few steps could be taken to improve this testing procedure in the future and may lead to obtaining our expected results. First, a more accurate measurement method should be devised for massing the activated carbon in the electrode. This should involve keeping the electrode material and electrode housing completely contained while removing the electrode material so none of the material is lost. It may also be helpful to redesign the cell hardware such that the entire cell can be submerged in electrolyte during testing so it remains fully hydrated. This may also help to increase the repeatability of experiments. One other possible technique would be to fill the hole in the electrode with an ionomer such as Nafion, which would retain its conductivity if some water was lost and would not be susceptible to wicking. We believe this project is worth pursuing in the future as our modeling suggests macro-structuring the electrode could lead to a significant improvement in cell performance.

## Appendix C

# In Situ, Through-Thickness Distribution Measurements of Oxygen Partial Pressure in a PEM Fuel Cell

An alternate version of the MES discussed in Chapter 2 was designed and fabricated to make oxygen concentration ( $c_{O_2}$ ) distribution measurements through the thickness of the cathode catalyst layer in a PEM fuel cell. The work is summarized here, but is presented in full detail in an *ECS Transactions* paper by Epting, Hess and Litster [72]. My contributions to this project included designing and building the hardware used to test the MES as well as collaborating to design and fabricate the MES structure. There were many similarities between the ionic sensing MES and the oxygen sensing MES, but while I conducted the research on the ionic sensing MES, my lab mate Billy Epting lead this work studying  $c_{O_2}$  distributions through the thickness of the cathode catalyst layer.

Fabrication of the oxygen sensing MES was similar to the fabrication of the ionic MES from Chapter 2. The main difference was how the sensing/insulating layers were fabricated. In the oxygen sensing MES, Teflon-FEP was spin-coated onto one side of the Kapton insulating layers to aid in hot-bonding the layers and a 200 nm layer of



Platinum was sputtered on the other side of the Kapton to be used as the sensing layers, also referred to as ultra-microelectrodes (UMEs). Another change is that a 2  $\mu\text{m}$  layer of Nafion was added to coat the walls of the hole drilled through the MES to keep the catalyst layer from electrically shorting with the platinum sensing layers and to provide electrolytic contact to the MES anode, which was used as a counter- and reference-electrode for the UMEs. GDLs were still placed at the end of each protruding UME, but were only used as electrical contacts, not HREs. Stacking the layers, assembling the MEA, etc. was a similar procedure to that used for the ionic MES. A schematic of the oxygen sensing MES is shown in Figure C.1.

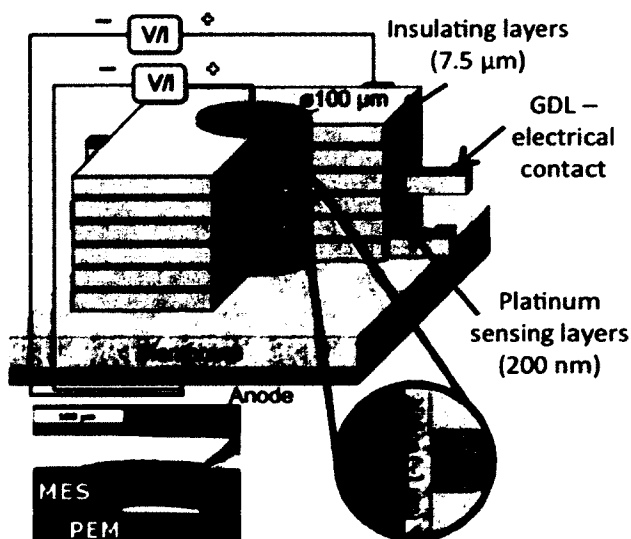


Figure C.1 Schematic of a platinum MES used for sensing oxygen partial pressure in the cathode catalyst layer of a PEM fuel cell.

The cell was run under low humidity conditions (50% RH) in order to ensure the study of single-phase gas transport limitations. The Bio-Logic potentiostat was used to the

control the cell current and the Keithley sourcemeter was used to run each UME one at a time as a working electrode with the cell anode as the reference and counter electrode. This method allowed us to obtain current measurements from each UME using a common reference electrode. CV was then conducted on each UME to verify they showed the expected behavior and to find limiting current regimes. The reverse sweep of a CV scan run on the UME located 42.3  $\mu\text{m}$  from the membrane can be seen in the inset of Figure C.2. A flat region in the curve around 0.2 V indicates an ORR limited regime for the UME. In this regime all of the oxygen at the electrode surface is consumed by the reaction. This fact will allow us to calculate the  $c_{O_2}$  based on the resulting UME current obtained. We can also see from Figure C.2 that the UMEs have a predictable and substantial response to changing the oxygen concentration in the cell. To make this plot, a UME was held in a diffusion limited regime, at 0.175 V, as the dimensionless oxygen concentration in the inlet gas (normalized by that in air) was varied from 1 to 0 with incremental changes every 60 s. We see that higher concentrations of oxygen lead to larger magnitudes of current and that there are significant decreases in the UME current as we decrease the oxygen concentration. Unfortunately, there were signs of electrode fouling while collecting this data and the results were not strongly repeatable as is evident when comparing the first and last step in Figure C.2, which were both conducted under full oxygen. Another measurement technique was implemented to overcome this issue.

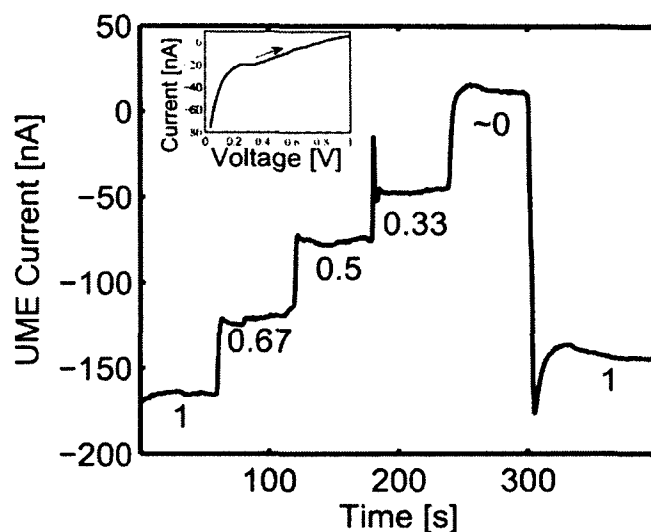


Figure C.2 Time series of UME current for the UME located  $7.5 \mu\text{m}$  from the membrane. The cell was held at  $0.175 \text{ V}$ , in the limiting current regime, as the oxygen concentration in the inlet air (listed on figure as a fraction of  $c_{O_2}$  in air) was varied every  $60 \text{ s}$ . The inset shows the reverse scan from CV conducted on the UME located  $42.3 \mu\text{m}$  from the membrane (scan rate  $5 \text{ mV/s}$ ). A transport-limited region can be seen around  $0.2 \text{ V}$ .

Pulsed amperometric detection (PAD) was used to obtain more repeatable results from the UMEs. This technique employed three potential pulses, which ensured that the measurements were not affected by electrode fouling. The first pulse anodically cleaned the electrode, the second pulse cathodically renewed it by stripping oxides and the third pulse measured the ORR current after a short delay was inserted to overcome capacitive currents. PAD was conducted on each UME individually to obtain the final distribution data, but it was also employed on adjacent pairs of UMEs to ensure each of the layers acted independently of one another and did not draw stray current from the other layers.

Multiple PAD waveforms were applied and averaged to obtain an average current,  $I_{meas}$ , for each UME in the MES while the fuel cell was held at a constant current of 450 mA/cm<sup>2</sup>. The measured currents were then translated into oxygen levels using equation [C.1]. In this equation  $I_{air}$  and  $I_{N_2}$  are calibration points that were measured before conducting the experiment, while the cell was at OCV.  $I_{air}$  is the PAD current measurement in an air environment while  $I_{N_2}$  is the same measurement in a nitrogen environment.

$$\frac{c_{O_2}}{c_{O_2}^{ref}} = \frac{I_{meas} - I_{N_2}}{I_{air} - I_{N_2}} \quad [C.1]$$

The results of the oxygen concentration distribution measurements are shown in Figure C.3. Each point represents an average of 23 PAD measurements and the error bars denote one standard deviation. A schematic of the fuel cell electrode is pictured below the x-axis to show the orientation of the measurements within the electrode. This figure shows a decrease in oxygen concentration as we move from the GDL (also known as diffusion medium - DM) towards the PEM. This is not surprising as we know there are many resistances hindering the transport of oxygen through the electrode. Additionally, oxygen is being consumed as it travels into the electrode. An analytical solution to the mass conservation equation derived from Fick's law, which assumes a spatially uniform reaction rate was fit to the data and is also shown in Figure C.3 (dashed curve). The catalyst layer/DM interface oxygen concentration,

$\overline{c_{O_2}}|_{CL/DM}$ , and the pore-phase catalyst layer diffusivity,  $D_{eff,CL}$ , were used as fitting parameters for this curve and were found to be,  $\overline{c_{O_2}}|_{CL/DM} = 0.75$  and  $D_{eff,CL} = 1.3 \times 10^{-7} \text{ m}^2/\text{s}$ . However, these values may not be completely accurate as the trend in the data is rather weak. This is likely because the fuel cell that was studied was not fully stable. Since the measurement at each layer took 5 minutes to collect, the system had sufficient time to change between consecutive UME measurements. In the future, the measurement process will be revised such that the measurements are made simultaneously or in quick succession to overcome this issue.

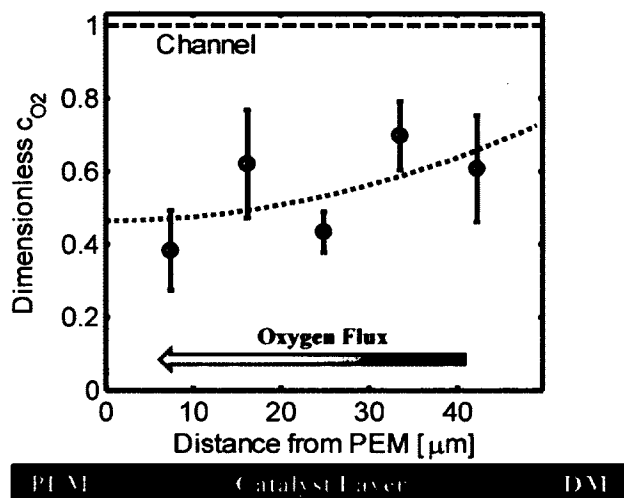


Figure C.3 Dimensionless oxygen concentration values are plotted versus distance through the electrode. Measurements were made at each UME one at a time while the cell was operating at  $450 \text{ mA}/\text{cm}^2$  and 50% RH. A schematic of the fuel cell cathode is shown below the x-axis, corresponding to the direction in which the measurements were made. The error bars represent one standard deviation. The dashed line is the analytical solution to the mass conservation equation derived from Fick's law.

## References

- [1] "U.S. & World Population Clocks," U. S. C. Bureau, Ed., ed, 2012.
- [2] S. C. Davis, S. W. Diegel, and R. G. Boundy, "Transportation Energy Data Book: Edition 30," Oak Ridge National Laboratory ORNL-6986, 2011.
- [3] M. A. Delucchi and J. J. Murphy, "US military expenditures to protect the use of Persian Gulf oil for motor vehicles," *Energy Policy*, vol. 36, pp. 2253-2264, 2008.
- [4] "Fourth Assessment Report of the IPCC," Intergovernmental Panel on Climate Change (IPCC)February 2007.
- [5] D. Papageorgopoulos, "Fuel Cell Technologies (DOE Overview)," in *Proceedings of the DOE Hydrogen Program Annual Merit Review*, Washington, D.C., 2011.
- [6] B. Barnett, "PHEV Battery Cost Assessment," in *Proceedings of the DOE Vehicles Technology Program Annual Merit Review*, Washington, D.C., 2010.
- [7] K. G. Gallagher, D. Dees, and P. Nelson, "PHEV Battery Cost Assessment," in *Proceedings of the DOE Vehicles Technology Program Annual Merit Review*, Washington, D.C., 2011.
- [8] "Basic Needs for Electrical Energy Storage," Department of EnergyApril 2-4, 2007 2007.
- [9] D. Harvey, J. G. Pharoah, and K. Karan, "A comparison of different approaches to modelling the PEMFC catalyst layer," *Journal of Power Sources*, vol. 179, pp. 209-219, 2008.
- [10] S. Litster and G. McLean, "PEM fuel cell electrodes," *Journal of Power Sources*, vol. 130, pp. 61-76, 2004.
- [11] M. Uchida, Y. Aoyama, N. Eda, and A. Ohta, "Investigation of the Microstructure in the Catalyst Layer and Effects of Both Perfluorosulfonate Ionomer and PTFE-Loaded Carbon on the Catalyst Layer of Polymer Electrolyte Fuel Cells," *Journal of The Electrochemical Society*, vol. 142, pp. 4143-4149, 1995.
- [12] R. O'Hayre, D. M. Barnett, and F. B. Prinz, "The triple phase boundary - A mathematical model and experimental investigations for fuel cells," *Journal of the Electrochemical Society*, vol. 152, pp. A439-A444, 2005.

- [13] F. Barbir, *PEM Fuel Cells: Theory and Practice*. London: Elsevier Academic Press, 2005.
- [14] M. C. Lefebvre, R. B. Martin, and P. G. Pickup, "Characterization of Ionic Conductivity Profiles within Proton Exchange Membrane Fuel Cell Gas Diffusion Electrodes by Impedance Spectroscopy," *Electrochemical and Solid-State Letters*, vol. 2, pp. 259-261, 1999.
- [15] R. Makharia, M. F. Mathias, and D. R. Baker, "Measurement of Catalyst Layer Electrolyte Resistance in PEFCs Using Electrochemical Impedance Spectroscopy," *Journal of The Electrochemical Society*, vol. 152, pp. A970-A977, 2005.
- [16] X.-Z. Yuan, *Electrochemical Impedance Spectroscopy in PEM Fuel Cells: Fundamentals and Applications*. London: Springer, 2010.
- [17] J. Wu, X. Z. Yuan, H. Wang, M. Blanco, J. J. Martin, and J. Zhang, "Diagnostic tools in PEM fuel cell research: Part I Electrochemical techniques," *International Journal of Hydrogen Energy*, vol. 33, pp. 1735-1746, 2008.
- [18] J. Wu, X. Zi Yuan, H. Wang, M. Blanco, J. J. Martin, and J. Zhang, "Diagnostic tools in PEM fuel cell research: Part II: Physical/chemical methods," *International Journal of Hydrogen Energy*, vol. 33, pp. 1747-1757, 2008.
- [19] R. O'Hayre, S.-W. Cha, W. Collela, and F. B. Prinz, *Fuel Cell Fundamentals*. New York: John Wiley & Sons, 2006.
- [20] I. A. Schneider, D. Kramer, A. Wokaun, and G. G. Scherer, "Effect of inert gas flow on hydrogen underpotential deposition measurements in polymer electrolyte fuel cells," *Electrochemistry Communications*, vol. 9, pp. 1607-1612, 2007.
- [21] A. M. Chaparro, A. J. Martín, M. A. Folgado, B. Gallardo, and L. Daza, "Comparative analysis of the electroactive area of Pt/C PEMFC electrodes in liquid and solid polymer contact by underpotential hydrogen adsorption/desorption," *International Journal of Hydrogen Energy*, vol. 34, pp. 4838-4846, 2009.
- [22] U. A. Paulus, Z. Veziridis, B. Schnyder, M. Kuhnke, G. G. Scherer, and A. Wokaun, "Fundamental investigation of catalyst utilization at the electrode/solid polymer electrolyte interface: Part I. Development of a model system," *Journal of Electroanalytical Chemistry*, vol. 541, pp. 77-91, 2003.

- [23] J. F. Whitacre, A. Tevar, and S. Sharma, "Na<sub>4</sub>Mn<sub>9</sub>O<sub>18</sub> as a positive electrode material for an aqueous electrolyte sodium-ion energy storage device," *Electrochemistry Communications*, vol. 12, pp. 463-466, 2010.
- [24] J. W. Long, D. Bélanger, T. Brousse, W. Sugimoto, M. B. Sassin, and O. Crosnier, "Asymmetric electrochemical capacitors—Stretching the limits of aqueous electrolytes," *MRS Bulletin*, vol. 36, pp. 513-522, 2011.
- [25] Y.-g. Wang and Y.-y. Xia, "Hybrid Aqueous Energy Storage Cells Using Activated Carbon and Lithium-Intercalated Compounds," *Journal of The Electrochemical Society*, vol. 153, pp. A450-A454, 2006.
- [26] H. Zhou, S. Zhu, M. Hibino, and I. Honma, "Electrochemical capacitance of self-ordered mesoporous carbon," *Journal of Power Sources*, vol. 122, pp. 219-223, 2003.
- [27] F. Lufrano, P. Staiti, and M. Minutoli "Influence of Nafion Content in Electrodes on Performance of Carbon Supercapacitors," *Journal of The Electrochemical Society*, vol. 151, pp. A64-A68, January 1, 2004 2004.
- [28] K. Chan, "Electrochemical characterization of electrospun activated carbon nanofibres as an electrode in supercapacitors," *Journal of Power Sources*, vol. 142, pp. 382-388, 2005.
- [29] C.-T. Hsieh and H. Teng, "Influence of oxygen treatment on electric double-layer capacitance of activated carbon fabrics," *Carbon*, vol. 40, pp. 667-674, 2002.
- [30] M. Eikerling and A. A. Kornyshev, "Modelling the performance of the cathode catalyst layer of polymer electrolyte fuel cells," *J. Electroanal. Chem.*, vol. 453, pp. 89-106, 1998.
- [31] C. Marr and X. Li, "Composition and performance modelling of catalyst layer in a proton exchange membrane fuel cell," *J. Power Sources*, vol. 77, pp. 17-27, 1999.
- [32] W. Sun, B. A. Peppley, and K. Karan, "An improved two-dimensional agglomerate cathode model to study the influence of catalyst layer structural parameters," *Electrochimica Acta*, vol. 50, pp. 3359-3374, May 2005.
- [33] M. S. Wilson and S. Gottesfeld, "Thin-Film Catalyst Layers for Polymer Electrolyte Fuel-Cell Electrodes," *Journal of Applied Electrochemistry*, vol. 22, pp. 1-7, Jan 1992.
- [34] T. E. Springer, T. A. Zawodzinski, and S. Gottesfeld, "Polymer Electrolyte Fuel Cell Model," *J. Electrochem. Soc.*, vol. 138, pp. 2334-2342, 1991.



- [35] Q. T. Qu, Y. Shi, S. Tian, Y. H. Chen, Y. P. Wu, and R. Holze, "A new cheap asymmetric aqueous supercapacitor: Activated carbon/NaMnO<sub>2</sub>," *Journal of Power Sources*, vol. 194, pp. 1222-1225, 2009.
- [36] A. D. Tevar and J. F. Whitacre, "Relating Synthesis Conditions and Electrochemical Performance for the Sodium Intercalation Compound Na<sub>4</sub>Mn<sub>9</sub>O<sub>18</sub> in Aqueous Electrolyte," *Journal of The Electrochemical Society*, vol. 157, pp. A870-A875, 2010.
- [37] F. N. Büchi and G. G. Scherer, "Investigation of the Transversal Water Profile in Nafion Membranes in Polymer Electrolyte Fuel Cells," *J. Electrochem. Soc.*, vol. 148, pp. A183-A188, 2001.
- [38] S. Takaichi, H. Uchida, and M. Watanabe, "In situ analysis of oxygen partial pressure at the cathode catalyst layer/membrane interface during PEFC operation," *Electrochimica Acta*, vol. 53, pp. 4699-4705, 2008.
- [39] P. Piela, T. E. Springer, J. Davey, and P. Zelenay, "Direct Measurement of iR-Free Individual-Electrode Overpotentials in Polymer Electrolyte Fuel Cells," *The Journal of Physical Chemistry C*, vol. 111, pp. 6512-6523, 2007.
- [40] J. Liu, M. Kunz, K. Chen, N. Tamura, and T. J. Richardson, "Visualization of Charge Distribution in a Lithium Battery Electrode," *The Journal of Physical Chemistry Letters*, vol. 1, pp. 2120-2123, 2010.
- [41] S. J. Harris, A. Timmons, D. R. Baker, and C. Monroe, "Direct in situ measurements of Li transport in Li-ion battery negative electrodes," *Chemical Physics Letters*, vol. 485, pp. 265-274, 2010.
- [42] S.-H. Ng, F. La Mantia, and P. Novák, "A Multiple Working Electrode for Electrochemical Cells: A Tool for Current Density Distribution Studies," *Angewandte Chemie International Edition*, vol. 48, pp. 528-532, 2009.
- [43] J. B. Siegel, X. Lin, A. G. Stefanopoulou, D. S. Hussey, D. L. Jacobson, and D. Gorsich, "Neutron Imaging of Lithium Concentration in LFP Pouch Cell Battery," *Journal of The Electrochemical Society*, vol. 158, pp. A523-A529, 2011.
- [44] "National Hydrogen Energy Roadmap," US Dept. of Energy November 2002.
- [45] P. P. Mukherjee and C. Y. Wang, "Stochastic microstructure reconstruction and direct numerical simulation of the PEFC catalyst layer," *Journal of the Electrochemical Society*, vol. 153, pp. A840-A849, 2006.
- [46] "HiSPEC Fuel Cell Catalysts," in <http://www.jmfuelcells.com/fccatalysts.html>, ed, 2011.

- [47] R. W. Lindstrom, K. Kortsdottir, M. Wesselmark, A. Oyarce, C. Lagergren, and G. Lindbergh, "Active Area Determination of Porous Pt Electrodes Used in Polymer Electrolyte Fuel Cells: Temperature and Humidity Effects," *Journal of The Electrochemical Society*, vol. 157, pp. B1795-B1801, 2010.
- [48] A. Parthasarathy, S. Srinivasan, A. J. Appleby, and C. R. Martin, "Electrode kinetics of oxygen reduction at carbon-supported and unsupported platinum microcrystallite/Nafion® interfaces," *Journal of Electroanalytical Chemistry*, vol. 339, pp. 101-121, 1992.
- [49] Y. Liu, C. Ji, W. Gu, J. Jorne, and H. A. Gasteiger, "Effects of Catalyst Carbon Support on Proton Conduction and Cathode Performance in PEM Fuel Cells," *Journal of The Electrochemical Society*, vol. 158, pp. B614-B621, 2011.
- [50] T. A. Zawodzinski, C. Derouin, S. Radzinski, R. J. Sherman, V. T. Smith, T. E. Springer, and S. Gottesfeld, "Water-Uptake by and Transport through Nafion(R) 117 Membranes," *Journal of the Electrochemical Society*, vol. 140, pp. 1041-1047, Apr 1993.
- [51] D. K. Paul, A. Fraser, and K. Karan, "Towards the understanding of proton conduction mechanism in PEMFC catalyst layer: Conductivity of adsorbed Nafion films," *Electrochemistry Communications*, vol. 13, 2011.
- [52] D. R. Lide, Ed., *CRC Handbook of Chemistry and Physics*. Taylor and Francis, Internet Version 2007, p.^pp. Pages.
- [53] P. Vanysek, "Ionic conductivity and diffusion at infinite dilution," in *CRC Handbook of Chemistry and Physics*. vol. 74th Ed., D. R. Lide, Ed., ed Boca Raton, 1993, pp. 5-90/5-92.
- [54] (October 17, 2011). *Fuzhou Yihuan Carbon Co., Ltd.* Available: [http://www.yhcarbon.com/index.php?\\_m=mod\\_product&\\_a=view&p\\_id=188](http://www.yhcarbon.com/index.php?_m=mod_product&_a=view&p_id=188)
- [55] K. C. Hess, W. K. Epting, and S. Litster, "Spatially Resolved, In Situ Potential Measurements through Porous Electrodes As Applied to Fuel Cells," *Analytical Chemistry*, vol. 83, pp. 9492-9498, 2011/12/15 2011.
- [56] B. Kastening, M. Hahn, and J. Kremeskovdtter, "The double layer of activated carbon electrodes part 2. Charge carriers in the solid material," *Journal of Electroanalytical Chemistry*, vol. 374, pp. 159-166, 1994.
- [57] F. Lufrano and P. Staiti "Conductivity and Capacitance Properties of a Supercapacitor Based on Nafion Electrolyte in a Nonaqueous System," *Electrochemical and Solid-State Letters*, vol. 7, pp. A447-A450, January 1, 2004 2004.

- [58] K. C. Hess, J. F. Whitacre, and S. Litster, "In Situ Measurements of Potential, Current and Charging Current across an EDL Capacitance Anode for an Aqueous Sodium Hybrid Battery," *Journal of The Electrochemical Society*, vol. 159, pp. A1351-A1359, January 1, 2012 2012.
- [59] M. C. F. Magalhães, E. Königsberger, P. M. May, and G. Hefter, "Heat Capacities of Concentrated Aqueous Solutions of Sodium Sulfate, Sodium Carbonate, and Sodium Hydroxide at 25 °C," *Journal of Chemical & Engineering Data*, vol. 47, pp. 590-598, 2002/05/01 2002.
- [60] R. A. Horne and D. S. Johnson, "Arrhenius Activation Energy of Electrical Conductance of Aqueous Lithium and Cesium Chloride Solutions in the -20 to +12°C Range," *The Journal of Chemical Physics*, vol. 45, pp. 21-23, 1966.
- [61] R. P. Iczkowski and M. B. Cutlip, "Voltage Losses in Fuel Cell Cathodes," *Journal of The Electrochemical Society*, vol. 127, pp. 1433-1440, July 1, 1980 1980.
- [62] P. N. Sharratt and R. Mann, "Some observations on the variation of tortuosity with Thiele modulus and pore size distribution," *Chemical Engineering Science*, vol. 42, pp. 1565-1576, 1987.
- [63] F. Gloaguen and R. Durand, "Simulations of PEFC cathodes: an effectiveness factor approach," *Journal of Applied Electrochemistry*, vol. 27, pp. 1029-1035, 1997/09/01 1997.
- [64] S. Otani and J. M. Smith, "Effectiveness of large catalyst pellets, An experimental study," *Journal of Catalysis*, vol. 5, pp. 332-347, 1966.
- [65] F. Lufrano and P. Staiti, "Performance improvement of Nafion based solid state electrochemical supercapacitor," *Electrochimica Acta*, vol. 49, pp. 2683-2689, 2004.
- [66] R. R. Garsuch, D.-B. Le, A. Garsuch, J. Li, S. Wang, A. Farooq, and J. R. Dahn, "Studies of Lithium-Exchanged Nafion as an Electrode Binder for Alloy Negatives in Lithium-Ion Batteries," *Journal of The Electrochemical Society*, vol. 155, pp. A721-A724, 2008.
- [67] M. Eikerling, A. A. Kornyshev, and E. Lust, "Optimized Structure of Nanoporous Carbon-Based Double-Layer Capacitors," *Journal of The Electrochemical Society*, vol. 152, pp. E24-E33, 2005.
- [68] H. Tamai, M. Kouzu, M. Morita, and H. Yasuda, "Highly Mesoporous Carbon Electrodes for Electric Double-Layer Capacitors," *Electrochemical and Solid-State Letters*, vol. 6, pp. A214-A217, 2003.

- [69] C. Kim, "Electrochemical characterization of electrospun activated carbon nanofibres as an electrode in supercapacitors," *Journal of Power Sources*, vol. 142, pp. 382-388, 2005.
- [70] S. Kondrat, C. R. Perez, V. Presser, Y. Gogotsi, and A. A. Kornyshev, "Effect of pore size and its dispersity on the energy storage in nanoporous supercapacitors," *Energy & Environmental Science*, vol. 5, pp. 6474-6479, 2012.
- [71] T. Okura, A. Morimoto, G. Inoue, and M. Kawase, "Structured EDLC Electrode with Through-Plane Microchannel," *Meeting Abstracts*, vol. MA2012-02, p. 523, June 4, 2012 2012.
- [72] W. Epting, K. C. Hess, and S. Litster, "In Situ Measurement of Oxygen Partial Pressure in a Cathode Catalyst Layer," *ECS Transactions*, vol. 33, pp. 1241-1249, 2010.